CHIRAL ANOMALY-BASED TRANSISTORS FOR LOW-DISSIPATION COMPUTING

CHEN JIEWEI

PhD

The Hong Kong Polytechnic University

2022

The Hong Kong Polytechnic University

Department of Applied Physics

Chiral anomaly-based transistors for low-dissipation computing

CHEN Jiewei

A thesis submitted in partial fulfilment of the requirements for the degree of Doctor of Philosophy

August 2021

CERTIFICATE OF ORIGINALITY

I hereby declare that this thesis is my own work and that, to the best of my knowledge and belief, it reproduces no material previously published or written, nor material that has been accepted for the award of any other degree or diploma, except where due acknowledgement has been made in the text.

____ (Signed)

CHEN Jiewei (Name of Student)

Abstract

As charge-based electronics are reaching their physical limits in reducing power consumption, the devices based on new physics mechanisms with low-dissipation transport characteristics offer opportunities to improve energy efficiency. In this thesis, we design and demonstrate three types of field-effect transistors based on chiral anomaly current in topological materials, including (1) Modulation of the chiral anomaly to achieve field-effect electronics with Dirac semimetal. (2) Topological transistors with Weyl semiconductor. (3) Room-temperature valley-based electrochemical transistor with high ON/OFF ratio

Firstly, we demonstrate field-effect chiral anomaly devices with Dirac semimetal $PtSe_2$. In analogous to valley degree of freedom in semiconductor, chiral anomaly current in Weyl/Dirac semimetals is theoretically predicted to be low loss over a long distance but still lacks experimental ways to efficiently control its transport. Here, we demonstrate field-effect chiral anomaly devices with Dirac semimetal $PtSe_2$, in which the Dirac point is close to the Fermi level. Through electrostatic gating with ionic liquid, we can modulate the chiral anomaly conductance by the external field with an ON/OFF ratio of more than 10^3 and realize basic logic functions in the device by regarding electric and magnetic fields as input signals. The chiral anomaly is further corroborated with nonlocal valley transport measurement, which can also be effectively modulated through magnetic and electrical fields, showing robust nonlocal valley transport with the diffusion length at the micrometre scale. Our works provide a way to manipulate chiral anomaly current for low-power electronics.

Secondly, we demonstrate the topological transistors with the Weyl semiconductor. The field-effect transistors with topological semiconductors can show low-dissipation transport based on the chiral anomaly in the "ON" state and topologically trivial "OFF" state, which promises low-power electronics. Here we demonstrate topological FETs with a high ON/OFF ratio by modulating the energy separation between Fermi level and Weyl point of Weyl semiconductor Te. By electrostatic manipulation of E_F, there is topological phase change between Weyl semimetal and semiconductor, and the negative magnetic resistance induced by chiral anomaly current reaches up to -90% in the Weyl semimetal state. We have achieved both enhancement and depletion mode FETs, with ~10^8 ON/OFF ratio under ≤2 V gating, 5.74×10^6 ON/OFF by –1 V gating and ultrahigh low-dissipation ON conductance of 100 mS, superior to the performance of general charge-based FETs and much higher than reported spin/valley FETs (about 10^1-10^3 ON/OFF). Furthermore, we have demonstrated multiple terminal and angle-switching logic functions in a single device, which is high area efficiency. Our results provide new strategies for preparing high ON/OFF FETs, which is promising for supplementing conventional charge-based electronics.

Thirdly, we have successfully achieved a valley-based electrochemical transistor with a high ON/OFF ratio at room temperature. As a quantum degree of freedom of electrons, the valley exhibits low-dissipation transport characteristics for carrying information with high energy efficiency. However, it still remains a grand challenge to efficiently operate the valley transistor at room temperature and realize basic digital and analogue computing functions. Here we demonstrate valley transistors with more than 7 μm diffusion length based on Weyl semiconductor (Te) at room temperature. The electrical double layer can volatilely shift E_F and modulate valley transistor with an ON/OFF ratio of 10^5. The ion intercalation/extraction can cause a non-volatile shift of E_F, showing 32 linear, symmetrical and discrete non-volatile states with low cycle-to-cycle variation (0.37%) for neuromorphic computing with the accuracy of 95.2% for classifying handwriting data. The coexistence of ion adsorption and intercalation mechanism results in the dynamic ion response with the high nonlinearity (4.35) and short-term memory curve for reservoir computing. The accuracy for temporal signal reaches as high as 95%. Our studies show the potential of low-power valley transistors for computing at room temperature.

In conclusion, we investigate the chiral anomaly-based transistors, which show the potentials of overcoming the physical limits (unavoidable heat dissipation) of the charge-based electronics. Modern electronics demands high performance with extreme energy efficiency (*e.g.*, abundant data computing). Our device shows potentials to address this issue: high ON/OFF ratio transfer curve, basic logic functions (AND, OR) and room-temperature neuromorphic computing to deal with static and dynamic information.

List of Publications

1. **<u>Jiewei Chen</u>**, Ting Zhang, Jingli Wang, Ning Zhang, Wei Ji, Shuyun Zhou and Yang Chai. Field-effect chirality devices with Dirac semimetal. *Advanced Functional Materials* 2104192 (2021).

2. **<u>Jiewei Chen</u>**, Jingli Wang, Linfei Zhang, Cong Wang, Ziyuan Lin, Wenjing Zhang, and Yang Chai. Room-temperature valley transistor with Weyl semiconductor. The sEDSSC conference (2020).

3. **<u>Jiewei Chen</u>**, Yang Chai. Chiral anomaly for field-effect transistors with integrated sensing and logic functions. The Spring Material Research Society Conference (2020).

4. **<u>Jiewei Chen</u>**, Ting Zhang, Jingli Wang, Ziyuan Lin, Jidong Liu, Cong Wang, Ning Zhang, Wenjing Zhang, and Yang Chai. Topological transistors with Weyl semiconductor, under review.

5. **<u>Jiewei Chen</u>**, Yue Zhou, Jingli Wang, Linfei Zhang, Cong Wang, Wenjing Zhang, and Yang Chai. Room-temperature valley transistors to process static and dynamic information, under preparation.

6. Feichi Zhou, **<u>Jiewei Chen</u>**, Xiaoming Tao, Xinran Wang, and Yang Chai. 2D Materials Based Optoelectronic Memory: Convergence of Electronic Memory and Optical Sensor. *Research* 9490413 (2019).

7. Feichi Zhou, Zheng Zhou, **<u>Jiewei Chen</u>**, Tsz Hin Choy, Jingli Wang, Ning Zhang,

Ziyuan Lin, Shimeng Yu, Jinfeng Kang, H.-S. Philip Wong and Yang Chai. Optoelectronic resistive random access memory for neuromorphic vision sensors. *Nature Nanotechnology* 14, 776–782 (2019).

8. Jingli Wang, Lejuan Cai, **Jiewei Chen**, Xunyu Guo, Yuting Liu, Zichao Ma, Zhengdao Xie, Hao Huang, Mansun Chan, Ye Zhu, Lei Liao, Qiming Shao and Yang Chai. Transferred Metal Gate to 2D Semiconductors for Sub-1 V Operation and Near Ideal Sub-Threshold Slope. *Science Advances* (accepted).

9. Ning Zhang, Cong Wang, **Jiewei Chen**, Canyu Hu, Jun Ma, Xi Deng, Bocheng Qiu, Lejuan Cai, Yujie Xiong, and Yang Chai. Metal Substitution Steering Electron Correlations in Pyrochlore Ruthenates for Efficient Acidic Water Oxidation. *ACS Nano* 15, 8537–8548 (2021).

10. Jing-Kai Qin, Feichi Zhou, Jingli Wang, **Jiewei Chen**, Cong Wang, Xuyun Guo, Shouxin Zhao, Yi Pei, Liang Zhen, Peide D. Ye, Shu Ping LauShu Ping Lau, Ye Zhu, Cheng-Yan Xu, and Yang Chai. Anisotropic Signal Processing with Trigonal Selenium Nanosheet Synaptic Transistors. *ACS nano* 14, 10018-10026 (2020).

11. Jingli Wang, Jingsi Qiao, Kang Xu, **Jiewei Chen**, Yuda Zhao, Bocheng Qiu, Ziyuan Lin, Wei Ji and Yang Chai. Quasi one-dimensional van der Waals gold selenide with strong interchain interaction and giant magnetoresistance. *Science Bulletin* 65.17, 1451-1459 (2020).

12. Ziyuan Lin, Jingli Wang, Xuyun Guo, **Jiewei Chen**, Chao Xu, Mingqiang Liu, Bilu Liu, Ye Zhu, Yang Chai. Interstitial copper-doped edge contact for n-type carrier

transport in black phosphorus. *InfoMat* 1.2 242-250 (2019).

13. Lejuan Cai , Ziyuan Lin , Mengye Wang, Feng Pan , **Jiewei Chen** , Yi Wang , Xinpeng Shen and Yang Chai. Improved interfacial H_2O supply by surface hydroxyl groups for enhanced alkaline hydrogen evolution. *Journal of Materials Chemistry A* 5.46, 24091-24097 (2017).

14. Bangjie Shao, Tsz Hin Choy, Feichi Zhou, **Jiewei Chen**, Cong Wang, Yong Ju Park, Jong-Hyun Ahn & Yang Chai. Crypto primitive of MOCVD MoS_2 transistors for highly secured physical unclonable functions. *Nano Research* 14.6, 1784-1788 (2021).

Acknowledgements

My three-year PhD study in the Hong Kong Polytechnic University passed quickly, which was an unforgettable and significant experience in my life. I am honoured to enjoy the scientific research under the supervision of Prof. CHAI Yang at the department of Applied Physics. After finishing this thesis, I would like to express my gratitude to many people who have given me great support.

At first, I would like to thank my supervisor Prof. CHAI Yang. I went to the Hong Kong Polytechnic University as a research assistant after giving me the offer in 2017. Later in 2018, I was admitted to the PhD program. It was lucky for me to have the opportunity to study and live in Hong Kong. Prof. CHAI Yang always encourages me to work on highly innovative and significant projects and emphasizes the importance of persisting and focusing on the specific project despite meeting tremendous difficulties. When I feel depressed after hundreds of experiment failures, he always gives me valuable guidance and suggestions. In addition, he supports my research in many aspects such as the design of projects, analysis of tested data, organization of experiment results in the manuscript and how to write a concise paper. With his professional and patient supervision, I can work hard and overcome the difficulties during my PhD study.

Then I would like to express my sincere gratitude to thank my group members and friends in the Hong Kong Polytechnic University, including Dr. Jingli Wang, Dr.

Yanghui Liu, Dr. Feichi Zhou, Dr. Jingkai Qin, Dr. Bocheng Qiu, Dr. Yang Wang, Dr. Mengye Wang, Dr. Lejuan Cai, Dr. Fuyou Liao, Dr. Weixin Li, Dr. Tianyue Wang, Ms Cong Wang, Ms Yue Zhou, Ms Tianqing Wan, Ms Sijie Ma, Mr. Jianmin Yan, Mr. Ziyuan Lin, Mr. Kang Xu, Mr. Xinpeng Shen, Mr. Zixuan Cai, Mr. Yi Wang, Mr. Yunpeng Zuo for their kind help and assistance.

At last, I would like to express my deep love to my parents for their unconditional support. Thanks very much for their understanding and support. I am always proud of them, just the same as they are proud of me. Their optimism drives me forward when meeting difficulties.

Table of Contents

Abstract .... **IV**

List of Publications .... **IV**

Acknowledgements .... **X**

Table of Contents .... **XII**

List of Figures .... **XIV**

List of Tables .... **XXIX**

Chapter 1 Demands for non-charge-based electronics **1**

1.1 Background 1

1.2 Significance of research 5

1.3 Structure of thesis 6

1.4 References 9

Chapter 2 Field-effect chirality devices with Dirac semimetal $PtSe_2$ **10**

2.1 Introduction 10

2.2 Experimental section 13

2.3 Results and discussion 15

2.4 Summary 37

2.5 References 38

Chapter 3 Topological transistors with Weyl semiconductor **41**

3.1 Introduction 41

3.2 Experiment section 43

3.3 Results and discussion 46

3.4 Summary 65

3.5 References 66

Chapter 4 Room-temperature valley transistors to process static and dynamic information 69

4.1 Introduction 69

4.2 Experimental section 73

4.3 Results and discussion 75

4.4 Summary 101

4.5 References 102

Chapter 5 Conclusions and outlook 104

5.1 Conclusions 104

5.2 Outlook 106

5.3 References 108

List of Figures

Figure 1.1 Ever-increasing energy consumption. (a) Total energy consumption for computing from 2020 to 2050. (b) Technological installed capacity for processing information..1

Figure 1.2 Chiral anomaly mechanism. (a) Sketch of a Dirac cone with two mixed Weyl nodes with opposite chiralities, which can be separated by the magnetic field. (b) Berry curvature of a topological semimetal. Nontrivial Berry curvature leads to the chiral anomaly. (c) Charge, valley, and isospin relaxation and mixing in topological semimetals..4

Figure 2.1 Chiral anomaly current in Dirac semimetal. “ON” state: E_{Fermi} is close to the Weyl point and $|\mu^{L}- \mu^{R}| \gg 0$. “OFF” state: E_{Fermi} away from the Weyl point and $|\mu^{L}- \mu^{R}| \approx 0$. 11

Figure 2.2 Chiral-anomaly related valley transport in the Dirac semimetal. (a) Sketch of a Dirac cone consisting of two slightly displaced massless Weyl nodes with distinct left-handed and right-handed chirality under the applied magnetic field. (b) Two typical processes in the chiral anomaly situation: charge pumping and inter-valley transport. 12

Figure 2.3 Berry curvature and charge pumping process in the Dirac semimetal. (a) Distribution of the square of the Berry curvature as a function of the relative energy Δε, the energy between Dirac/ Weyl point and Fermi level. There is the most substantial Berry curvature when the Fermi level is at the Dirac/Weyl point. As Fermi level moves away from the Dirac/Weyl point, Berry curvature decays remarkably. (b) Schematic illustration of the charge pumping process between left-handed and right-handed fermions arises from the chiral anomaly. 17

Figure 2.4 Illustration of a device structure for chirality-based field-effect devices... 18

Figure 2.5 Chirality-based field-effect device. (a) Schematic curves of electrical conductivity in charged-based field-effect transistor as a function of V_{ds} (left panel) and V_g (right panel), respectively. In an n-type depletion-mode FET, I_D is the drain current, $\boldsymbol{IDSS}$ is maximum saturation current, and V_P is the pinch-off voltage at which the channel closes. (b) Schematic curves of chiral conductivity in chirality-based field-effect devices as a function of B^2 (left panel) and V_g (right panel), respectively. For the curve as a function of V_g, the dashed line refers to the situation that the Fermi level can easily cross the topological point due to too small $\Delta\varepsilon$, while the solid line shows the case that Fermi level cannot cross the topological point. 18

Figure 2.6 Crystal structure and layer-dependent bandgap of $PtSe_2$. (a) Schematic image of the crystal structure of $PtSe_2$ from the side view (left panel) and top view (right panel). (b) The layer-dependent bandgap of $PtSe_2$ calculating by the path M-K-G-M of the Brillion zone 19

Figure 2.7 Band structures of bulk $PtSe_2$ along different paths. (a) Brillion zone of bulk $PtSe_2$ and the proposed Dirac point is marked as "D". (b) Parallel to G-M line. (c) Vertical to G-M line. (d) Along k_z direction. Dirac cones point around D (0, 0.32, 0.5) in three different orthogonal directions. 20

Figure 2.8 Three dimensional band structures around the Dirac point. (a) Three-dimensional band structures along k_x and k_y. (b) Three-dimensional band structures along k_x and k_y, where k_x is the direction vertical to G-M line, and k_y is the direction parallel to G-M line. The variable range is +/-0.1(unit 2π/a)......................................21

Figure 2.9 The element ratio of the used $PtSe_2$ flake. (a) Scanning electron microscope image of $PtSe_2$ crystal flake. (b)The EDX spectrum of $PtSe_2$ crystal indicates that Se is deficient...22

Figure 2.10 Hall bar device #1. (a) The optical microscope photograph. (b) Tested height of the sample (~12 nm) determined by AFM. (c) Raman spectra of sample #1 and bulk $PtSe_2$ crystal. Two pronounced peaks around 183 and 206 cm^{-1} can be observed when and the typical peak at around 230 cm^{-1} of few-layer $PtSe_2$ is absent. (d) Metallic temperature-resistance curve. (e) Angle-dependent MR varying from 21.16% ($B \perp E$) to -0.97% ($B /\!/ E$). (f) MR as a function of magnetic field under $B \perp E$ at 2K. 23

Figure 2.11 Hall resistance and magnetotransport behaviour of #1. (a) The Hall resistance varies from 300K to 2K of sample #1. (b) Magnetotransport behaviours of Hall bar device #1 under $B/\!/E$ at 2K. MR= $\boldsymbol{RB - R(0)R(0) \times 100\%}$, where $\boldsymbol{R(0)}$ is the resistance at zero magnetic field, and $\boldsymbol{R\ (B)}$ is the resistance under B. The inset is σ_{chiral} as a function of B^2, extracted according to $\sigma_{chiral} = \sigma - \sigma_0$, where σ is the conductivity under specific magnetic field, and σ_0 is the conductivity without magnetic field. 24

Figure 2.12 The downshift of the Dirac point of electron-doped $PtSe_2$. (a) Hall resistance of sample #2 at different temperatures. The Hall resistance increases as the temperature vary from 300K to 2K. (b) The density of states of pristine and electron-doped $PtSe_2$. The circles highlight the position of the Dirac point in pristine and electron-doped $PtSe_2$. 25

Figure 2.13 Angle-dependent longitudinal magnetic resistance of sample #3. (a) Angle-dependent longitudinal magnetic resistance of 4-terminal sample #3. Inset is the optical microscope photograph of a typical tested 4-terminal sample. (b) Longitudinal MR of sample #3 at small rotation angles near *B//E*. 26

Figure 2.14 Angle-dependent negative longitudinal magnetic resistance of 4-terminal sample #4 (~15 nm) at 2K. When $B // E$, there is the strongest negative longitudinal magnetic resistance. As the angle gradually reduces, the negative magnetic resistance becomes weaker. When $B \perp E$, the strongest positive magnetic resistance is about 36%. 26

Figure 2.15 Magnetotransport behaviours in thick samples with more than 160 nm. . 27

Figure 2.16 Planar Hall tests of our $PtSe_2$ sample. (a) Schematic of angular-dependent planar Hall tests. *B*, *E* and the sample are in the same plane. $\boldsymbol{\varphi}$ is the angle between *B* and *E*. (b) Angular dependence of the R_{xy}. (c) Angular dependence of the R_{xx}. Tested R_{xy} and R_{xx} are well fitted by $\boldsymbol{\gamma R \parallel - R \perp 2\sin 2\varphi}$ and $\boldsymbol{R \parallel + R \perp 2 + R \parallel - R \perp 2\cos 2\varphi}$, respectively. $\boldsymbol{\gamma}$ is the ratio of the width to the length of the prepared Te device, $\boldsymbol{R \parallel}$ is longitudinal MR under $\boldsymbol{B \parallel E}$, and $\boldsymbol{R \perp}$ is longitudinal MR under $\boldsymbol{B \perp E}$. The tests were carried out at 2K under 6T. 29

Figure 2.17 The manipulation of the chiral anomaly in $PtSe_2$ semimetal. (a) Schematic of gating $PtSe_2$ by the ionic liquid. (b) The shift of energy gap between E_F and Dirac point. The position of the Fermi level can be tuned by applying different V_g. (c) I_g-V_g curve of the ion liquid gating at 220K. The faster scanning (0.1 V s^{-1} vs 0.02V s^{-1}) rate leads to a larger hysteresis loop because of the effective movement of ions under gating, which is common in ionic liquid gating FET devices. (d) I_g-T curves for sample #7 under different V_g. 30

Figure 2.18 Resistance-temperature curves of sample #8. The testing order is V_g= 0, V_g= -2V, V_g= +2V and V_g= 0. 31

Figure 2.19 Chirality-based field-effect $PtSe_2$ device. (a) Chiral anomaly-based negative MR curves as a function of B under different V_g. The inset shows that E_{Fermi} is below the Dirac point of $PtSe_2$ at V_g=0. (b) σ_{chiral} as a function of B^2 under different V_g. 32

Figure 2.20 Chiral anomaly-based negative magnetic resistance curves as a function of B at different gating voltages under B // E. Both samples #4 and #10 show V_g-dependent magnetic resistance curves. 32

Figure 2.21 Gating thick $PtSe_2$ sample #11 (~90 nm) through the ionic liquid. 33

Figure 2.22 Demonstrations of logic operations based on chiral anomaly current. (a) Demonstration of AND logic gate. INPUT 1 is “0” for $B \leq 4.5$T, and “1” for $B > 4.5$T. INPUT 2 is “0” for $V_g \leq 0$ V, and “1” for $V_g > 0$ V. OUTPUT is “0” for $\sigma_{chiral} \leq 780$ S

cm^{-1}, and "1" for $\sigma_{chiral} > 780$ S cm^{-1}. (b) OR-AND logic operation. We define θ as input 1 with 0°as "0" and 10° as "1". V_g is defined as input 2 with V_g = +2V as "0" and -2V as logic "1". Input 3 is *B* with 3 T as logic "0", and 6 T as logic "1". The output is defined as "0" corresponding to the negative MR, and "1" corresponding to the positive MR. 34

Figure 2.23 Chirality-based nonlocal width-dependent valley transport. (a) Schematic view of the inter-valley diffusion between different valley positions (±K), compensating the chiral anomaly induced charging pumping process. (b) Scanning electron microscopy of sample #V1. It has the same channel length of 2 μm and different channel width of 2 μm (terminal 3-4), and 1 μm (terminal 5-6), respectively. (c) Width-dependent valley transport in sample #V1 under the magnetic field modulation. The inset shows the ratio of $R_{56\text{-}NL}/R_{34\text{-}NL}$ as a function of *B* at different temperatures. The dashed line corresponds to the theoretical value of 0.50. 35

Figure 2.24 Length-dependent valley transport. (a) Scanning electron microscopy of sample #V2. It has the same channel width 2 μm and different channel length from 2 μm (terminal 3-4), 4 μm (terminal 5-6) to 7 μm (terminal 7-8). (b) Length-dependent valley transport sample #V1 under the magnetic field modulation. (c) Electrical modulation of length-dependent valley transport strength through ionic liquid gating. The calculated valley strength $|\alpha_{NL}|$ as a function of diffusion length shows that $|\alpha_{NL}|$ decays exponentially with the increasing of lateral length. 37

Figure 3.1 Comparison of working mechanisms. (a) The working mechanism of conventional field-effect transistors. (b) Working mechanism of topological transistors. 47

Figure 3.2 Weyl points and the operation of the topological transistors. (a) Weyl points in Te along the L-H path. Inset is the Brillion zone. (b) Berry curvature related working mechanism. 48

Figure 3.3 The crystal structure and density of states for the perfect and defective Te. (a) Schematic of the perfect Te supercell without defects (b) Schematic of the Te supercell with one Te vacancy (marked by the red circle). (c) The density of states of the perfect and defective Te, respectively. The Fermi level shifts downwardly approximately 0.2 eV, close to the Weyl point (W_1) in the valence band. 48

Figure 3.4 Representative Te flakes with different thicknesses. 49

Figure 3.5 Angle- and temperature-dependent MR in sample #1. (a) Angle-dependent longitudinal MR in the prepared Te device. MR= $\boldsymbol{RB-R(0)R(0)}\times\boldsymbol{100}\%$, where $\boldsymbol{R(0)}$ is the resistance at zero magnetic field, and $\boldsymbol{R}\ (\boldsymbol{B})$ is the resistance under B. Inset is the scanning electron microscope image of the prepared Te device. The scale bar is 10 μm. (b) Precise angle-dependent negative MR from 0° to 10° at 2 K. (c) Temperature-dependent MR from 200 K to 2 K. Negative MR appears at 100 K under low magnetic field. Around 7.5 T, there is an angle- and temperature-dependent oscillation peak. 50

Figure 3.6 Angle-dependent negative MR in sample #2 at 2 K. (a) Angle-dependent MR from 0° to 90°. (b) Precise angle-dependent MR from 0° to 10°. There is also an oscillation peak around 7.5 T. 50

Figure 3.7 Reproducible negative MR characteristics under *B*//*E*. Te samples with the thickness ranging from (a) 70 nm to (f) 28 nm. 51

Figure 3.8 No observable magnetic elements doping in the Te sample. (a) EDX spectrum of the prepared Te flake. The inset is the captured scanning electron microscope image with a pink rectangle as the analytical area. (b) Raman spectrum clearly shows three typical peaks E_1 (94 cm^{-1}), A_1 (123 cm^{-1}) and E_2 (143 cm^{-1}), which are typical Raman peaks for Te sample. 52

Figure 3.9 Exclusion of the current effect on the observed negative MR behaviours. (a1, b1) Angle-dependent MR, (a2, b2) MR under *B*//*E*, and (a3, b3) MR under $B \perp E$ in the four-probe test and two-probe magnetotransport tests, respectively. 52

Figure 3.10 Planar Hall effect of Te device to further corroborate the observed chiral anomaly. (a) Schematic of test structure of planar Hall tests. *B*, *E* and the sample are in the same plane. $\boldsymbol{\varphi}$ is the angle between *B* and *E* (b) Angular dependence of the R_{xy}. Experiment data are well fitted by $\boldsymbol{\gamma R \parallel - R \perp 2 \sin 2\varphi}$, where $\boldsymbol{\gamma}$ is the ratio of the width to the length of the prepared Te device, $\boldsymbol{R \parallel}$ is longitudinal MR under $\boldsymbol{B \parallel E}$, and $\boldsymbol{R \perp}$ is longitudinal MR under $\boldsymbol{B \perp E}$. (c) Angular dependence of the R_{xx}. Experiment data are well fitted by $\boldsymbol{R \parallel + R \perp 2 + R \parallel - R \perp 2 \cos 2\varphi}$. These tests were carried out at 2 K under 6T. 53

Figure 3.11 (a, b) Hall resistance and (c) MR of thick and thin samples under $\boldsymbol{B \perp E}$. 54

Figure 3.12 Carrier-density-dependent MR. (a) The temperature-dependent MR of 32-nm-thick sample under *B*//*E*. The hole carrier density is 3.39×10^{13} cm^{-2} at 2K. (b) The temperature-dependent MR of 12-nm-thick sample under *B*//*E*. The hole carrier density is 2.25×10^{12} cm^{-2} at 2K. (c) Carrier-density-dependent MR in different samples. The insets are the corresponding optical images of the prepared Hall bar structures based on 32-nm-thick and 12-nm-thick samples. 55

Figure 3.13 Schematic of topological transistors with Weyl semiconductor Te. Te flake and the side gate electrode are covered with ionic liquid (DEME-TSFI). Gating voltage can drive ions onto the channel surface of Te. 56

Figure 3.14 Magnetotransport tests of 32-nm-thick and 12-nm-thick samples under *B*//*E* at different gating voltages, respectively...57

Figure 3.15 Electrical gating to manipulate the Δσ and σ. (a, b) $\Delta\sigma$ as a function of B^2 in 32-nm-thick and 12-nm-thick samples, analogue to the I_d-V_d curve of conventional charge-based FETs. The linear relationship between $\Delta\sigma$ and B^2 is in good agreement with the chiral anomaly equation under a relatively low magnetic field. Different modes of topological FET with Weyl semiconductor Te. (c) Depletion-mode FET based on 32-nm-thick sample. E_F is close to the Weyl point at V_g= 0. (d) Enhancement-mode FET based on 12–nm-thick sample. E_F is far away from the Weyl point at V_g= 0. 58

Figure 3.16 Transfer curve of prepared conventional charge-based Te FET at 300 K.59

Figure 3.17 Performance comparison between conventional charge-based FETs and TPCTs. (a) Output curve in the Te charge-based FET as V_g increases from -70 V to 70

V. (b) Transfer curve in the Te charge-based FET, typical p-type FET with a ON/OFF ratio of 2.0 $\times 10^5$ and ON-state conductivity of 660 μS/μm. (c) Chiral anomaly conductivity as a function of B^2 in the Te TPCT. (d) Transfer curve as a function of V_g in the Te TPCT with an ON/OFF ratio of 3.5×10^8 and ON-state conductivity of 3.9×10^4 μS/μm. 60

Figure 3.18 Performance comparison. (a) Summarized performance in prepared short-channel TPCTs. Inset is the SEM image of a typical device with ~300 nm channel length. The scale bar is 2 μm. (b) ON-state conductivity versus ON/OFF ratio in our work, the FETs based on low-dimensional materials and state-of-the-art Si transistors. Te_{RT} and Te_{LT} are the performance in Te charge-based FET at 300K and 10K, respectively. Three kinds of Intel 14-nm transistor: HP (high performance), SP (standard performance), and ULP (ultralow-power). 62

Figure 3.19 Multiple-mode logic functions based on the topological Te FETs. (a) Two-input AND logic function. (b) Three-input OR-AND logic function. (c) Demonstration of a single topological Te FET for angle-switching logic functions (OR, AND). 64

Figure 4.1 Chiral anomaly in Dirac/Weyl physics. Charge pumping refers that the charge depleted at one Weyl node will be generated at the other node with opposite chirality. The charge pumping between Weyl nodes results in the low-dissipation chiral anomaly current ($\boldsymbol{Jc}$), which generates and transports in the form of $\boldsymbol{Jc} = \boldsymbol{e2B4\pi2\hbar2c}(\boldsymbol{\mu R} - \boldsymbol{\mu L})$. $\boldsymbol{Jc}$ is topologically protected and "even" under time reversal. 70

Figure 4.2 Typical scheme of the band structure for the topological semimetal and the topological semiconductor. 71

Figure 4.3 Detection of inter-valley transport based on the chiral anomaly. Valley pseudospin (indicated by node position ±K) imbalance relaxes at a rate of $\boldsymbol{\tau v-1}$. For practical tests, planar and nonlocal electrodes are prepared in the etched samples for detecting the valley. 72

Figure 4.4 Crystal structure, Brillion zone and bandstructure of Te. 76

Figure 4.5 Calculation configuration and densities of states of different Te structures. (a-d) Configuration of perfect Te, defective Te (1.23% Te vacancy), defective Te_{Li1} (1.23% Te vacancy and 1.23% Li doping) and defective Te_{Li2} (1.23% Te vacancy and 2.46% Li doping). Te vacancy is marked yellow ball. Doping Li is marked purple ball. (e) Densities of states of perfect and defective Te. (f) Densities of states of defective Te with different concentrations of Li doping. 77

Figure 4.6 The summary of calculated energy separation between E_F and Weyl point W_1. There are perfect Te, defective Te (1.23% Te vacancy), defective Te_{Li1} (1.23% Te vacancy and 1.23% Li doping) and defective Te_{Li2} (1.23% Te vacancy and 2.46% Li doping). 78

Figure 4.7 Valley transistors based on the ion manipulation. Electrical double layer of ions with volatile shift of E_F in Te flakes for valley transistors. Reversible ion intercalation/extraction with non-volatile shift of E_F in Te flakes for valley synapses. 79

Figure 4.8 Self-doped high hole carrier density (n_{2D} =3.0×10^{13} cm^{-2}). 80

Figure 4.9 Temperature-dependent valley transport. (a) Schematic and scanning electron microscopy image of the "H" geometry valley device. (b) Temperature-dependent valley transport from 300K to 2K. 80

Figure 4.10 Length-dependent valley transport. (a) Nonlocal resistance as a function of the magnetic field. (b) The zero-magnetic field resistance as a function of length. (c) |R_{VNL}| as a function of channel length in the semi-log curve, well fitted by a straight line. Inset is the schematic of the length-dependent valley device. 81

Figure 4.11 Width-dependent valley transport. (a) Width-dependent valley transport as a function of B. (b) Valley transport ratio of different widths. Inset is the schematic of width-dependent valley device. 82

Figure 4.12 Angle- and temperature-dependent longitudinal MR. (a) Angle-dependent MR from 0° to 90° at 2K. Inset shows the definition of the rotation angle. The angle between B and E is defined as θ. (b) Precise angle-dependent negative MR from 0° to 10° at 2K. (c) Temperature-dependent MR from 150 K to 2 K. Negative MR appears at 100 K under a low magnetic field. 83

Figure 4.13 The performance of Te valley transistors. (a) α_{NL} as a function of B^2 in the Te valley transistor. (b) Transfer curve as a function of V_g in the 28-nm Te valley transistor under 1T. A typical enhancement-mode transistor. (c) ON/OFF ratio versus thickness of Te flakes in our valley transistors. 84

Figure 4.14 Charge-based FET in the same Te flake as the valley FET. (a) Output curve

I_d-V_d in the charge-based FET as V_g increases from -60 V to 60 V with a step of 20V. (b) Transfer curve in the Te charge-based FET. 85

Figure 4.15 Thickness-dependent logic functions (AND, OR). 86

Figure 4.16 Ion intercalation/extraction mechanism in our valley devices. (a) XPS Te 3d spectra of Te. (b) XPS Li 1s spectra of Te. (c) XPS Cl 2p spectra of Te. 88

Figure 4.17 Stable valley states with linear increasing. (a) Long-term potentiation and depression displaying discrete states under the control of voltage pulses. +2V is used to intercalate Li^+ into Te and move the E_F away from the Weyl point. -2V is used to extract Li^+ and move E_F back. The zoom-in of (a) with linear and discrete states. (b) Stable valley states under 3000 s retention tests. 88

Figure 4.18 Valley synapses with different stable states. (a)8, (b)16, (c)24 and (d)32 discrete and linear states through electrochemical modulation. 89

Figure 4.19 Different nonlinearities of the LTP and LTD to fit the experimental data. All the data are normalized from 0 to 1 before the fitting. 90

Figure 4.20 Cycle-to-cycle performance of valley synapses with different stable states. (a)8, (b)16, (c)24 and (d)32 discrete states under different stimulation pulses. 90

Figure 4.21 Processing the static information based on valley synapses with linear, discrete and stable states. (a) Neuromorphic computing based on a three-layer neural network. A voltage programmed crossbar array with valley synaptic devices is shown. (b) Training the neural network using different valley states based on voltage-controlled "write" operations for classifying static MNIST. 91

Figure 4.22 The distribution probability between the neurons of inputs and hidden layers in synapses with different states after training. 92

Figure 4.23 Nonlinear and short-term memory behaviours with the pulse coding. (a) Nonlinear decaying curve with short-term memory. Decaying data follows a fitted exponential curve and the characteristic time t_0 obtained by fitting is 2.55 ms. After stimulation, it takes about ~10 ms for the output value to retain stability. (b) Dynamic responses after representative input signals, (10010), (11011), (01110) and (10101). "1" indicates the applied stimulation pulse of 4 V with 1 ms. (c) The summarised output of the device at the fifth pules. 93

Figure 4.24 Nonlinear and short-term memory behaviours with the pulse coding. (a) Pulse-coding to nonlinearly deal with five dynamic icons of the Tokyo Olympic Games. Each dynamic icon consists of three much different motions. Every five pixels is a group for nonlinear processing. (b) Reservoir computing network to process dynamic information. The classifying accuracy of processing dynamic information. 96

Figure 4.25 Classifying the dynamic icons. (a) The measured states of the reservoir neurons for the rhythmic gymnastics icon. (b) Accuracy of classifying the dynamic ions with 10% noise based on the reservoir computing network. (c) Confusion matrix for classifying the five dynamic icons of the test set. Colour bar: occurrence of a given predicted output. 97

Figure 4.26 The measured states of the reservoir neurons for different dynamic icons. 97

Figure 4.27 Dynamic icons with 10% noise for the test in reservoir computing.........98

Figure 4.28 Dynamic athletics icon with 10% noise for the test in reservoir computing. 99

Figure 4.29 Dynamic golf icon with 10% noise for the test in reservoir computing...99

Figure 4.30 Dynamic shooting icon with 10% noise for the test in reservoir computing. 99

Figure 4.31 Dynamic rhythmic gymnastics icon with 10% noise for the test in the reservoir computing. 100

Figure 4.32 Dynamic baseball icon with 10% noise for the test in reservoir computing. 100

List of Tables

Table 1.1 Comparison of charge, spin and valley as information carriers.....................3

Table 2.1 Summary of thickness-dependent MR..28

Table 3.1 ON/OFF ratio comparison among our work, reported spin/valley-based FETs and charge-based FETs. 61

Table 4.1 Comparison of the topological semimetal and semiconductor for chiral anomaly-based electronics. 72

Table 4.2 Performance comparison among our valley transistor, Te charge transistor and valley transistor. 85

Table 4.3 The outputs after 32 different input states numbered #0 to #31...................93

Chapter 1 Demands for non-charge-based electronics

1.1 Background

Semiconductor Industry Association (SIA) and Semiconductor Research Corporation (SRC) have identified reducing power consumption as one of the most urgent issues in the next decade of semiconductors research and development[1]. Information processing is mainly based on complementary metal-oxide semiconductors (CMOSs) by manipulating the charge transport. Charge-based electronics suffer from unavoidable joule heating and related power consumption, approaching fundamental limits in energy efficiency. As shown in **Figure 1.1a**, the total energy consumption of computing grows exponentially with the speed of doubling approximately every three years. In the meantime, there is a linear increase in the world's energy production at a rate of roughly 2% per year. This rising global computing energy is driven by ever-growing demands for the computation market (**Figure 1.1b**).

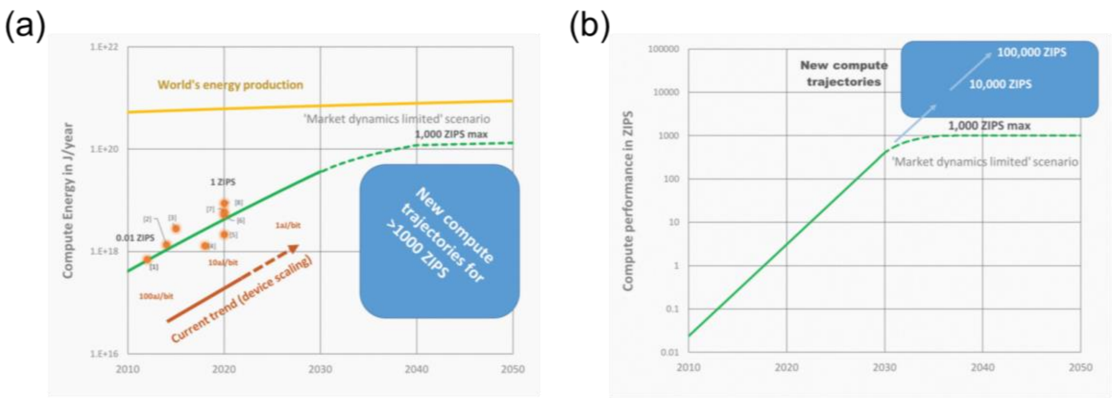

Figure 1.1 Ever-increasing energy consumption[1]. (a) Total energy consumption for computing from 2020 to 2050. (b) Technological installed capacity for processing

information.

As conventional electronics reach their physical limits in reducing power consumption, new physics based non-charge-based electronics offers opportunities to improve energy efficiency dramatically. **Table 1.1** shows the comparison of valley, charge and spin in the aspect of physical origin, advantages and disadvantages[2]. For the charge-based information carriers, it is easy to initiate, control and detect, but there is unavoidable Joule heating. In contrast, spin and valley carriers show no direct Joule heating and low-dissipation characteristics. Under time reversal, the charge current is “odd’ while spin and valley current is “even”. Specifically, spin-based electronics mainly include three processes: spin-charge conversion, spin transport and spin manipulation. The first step is the spin-charge conversion. By the suitable design, charge signals can convert into the spin by the way compatible with integrated circuits. After injecting the spin current, the long spin transport is better for practical applications. To achieve high-performance spintronics, the manipulation of spin should be as efficient as charge-based electronic devices. Valleytronics indicate the conceptual electronic applications based on the valley degree of freedom to process information, which are promising devices for achieving low-power data processing. There are Berry curvature hotspots for physical access with electric and magnetic fields. Exciting, transport and manipulation of the valley are the cornerstones of valleytronics. Further physical understanding and novel conceptual applications are motivated to provide information processing advantages that complement or surpass current electronics based on charge.

Table 1.1 Comparison of charge, spin and valley as information carriers[2]

	Charge	Spin	Valley
Physical origin	Electron charge	Electron spin angular momentum	Electron sublattice orbital angular momentum
Pros	Direct response to an electric field Easy to initiate, control and detect Direct optoelectronic coupling to light intensity High speed	Non-volatile No direct Joule heating Long spin lifetime and decoherence time Direct coupling to photon spins	Large Berry curvature hotspot for physical access with electric and magnetic fields No direct Joule heating Long valley lifetime (especially with spin-valley locking) Direct coupling to photon spins Non-volatile (in a magnetic heterostructure)
Cons	Joule heating Typically volatile Fast decoherence due to electron scattering	No direct response to an electric field Initiation, control and detection typically rely on indirect spin–charge conversion Low spin–charge conversion efficiency May require magnetic field	No direct response to an electric field Initiation, control and detection typically rely on indirect valley–charge conversion Low valley–charge conversion efficiency May require magnetic field Fast valley decoherence (so far)

Apart from widely investigated non-charge-based spin and valley current, chiral-anomaly-based current (J_c) can also be used for low-dissipation information processing. Due to the global topology of gauge fields, the chiral anomaly current is topologically protected[3,4]. For the Dirac semimetal, the magnetic field can separate two Weyl nodes with opposite chiralities[5] (**Figure 1.2a**). Under the parallel magnetic and electric fields, the charge depleted at one Weyl node will be generated at the other node with opposite chirality (charge pumping process)[5,6]. Initially the right- and left-handed fermions in the different Weyl nodes have equal chemical potential ($\mu^{\mathrm{L}}= \mu^{R}$). In the presence of parallel electric field, there would be an imbalance ($\mu^{\mathrm{L}} \neq \mu^{R}$) between two Weyl nodes with opposite chirality. In such a case, the continuity equation of right- or left-handed Weyl node takes the form of $\nabla \cdot j^{\mathrm{R,L}} + \partial_t \rho^{\mathrm{R,L}} = \pm \frac{e^3}{4\pi^2\hbar^2 c}\mathbf{E}\cdot\mathbf{B}$. The chiral charge at a single Weyl node is not conserved, which is the so-called chiral anomaly. The charge depleted at one Weyl node will be generated at the other node with opposite chirality (charge pumping) and thus the charge is conserved over all the system. The charge pumping between Weyl nodes results in the low-dissipation J_c, which generates and transports in the form of $J_c = \frac{e^2 B}{4\pi^2 \hbar^2 c}(\mu^R - \mu^L)$. J_c is topologically protected and "even" under time reversal[4]. The chiral anomaly arises from the nontrivial Berry curvature[7], and there is the strongest Berry curvature when Fermi level is at the Weyl point (**Figure 1.2b**). The chiral will cause a valley imbalance if we apply the parallel electric and magnetic fiedls[8]. As shown in **Figure 1.2c**, inter-valley transport can relax valley imbalance at a rate of τ_v^{-1}. The relaxation time of the valley is long due to the large quasi-momentum transfer, so the valley can diffuse over a long distance.

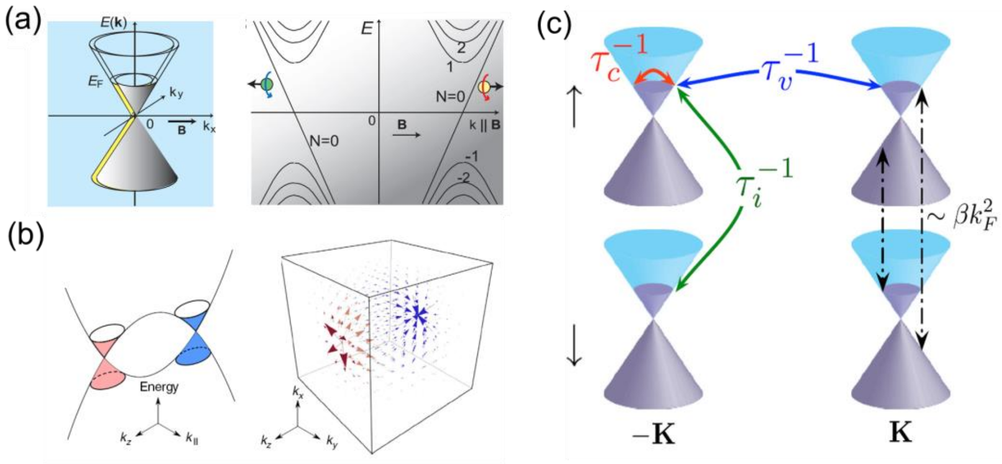

Figure 1.2 Chiral anomaly mechanism. (a) Sketch of a Dirac cone with two mixed Weyl nodes with opposite chiralities, which can be separated by the magnetic field[5]. (b) Berry curvature of a topological semimetal[7]. Nontrivial Berry curvature leads to the chiral anomaly. (c) Charge, valley, and isospin relaxation and mixing in topological semimetals.

1.2 Significance of research

Weyl fermions-related chiral anomaly has attracted much attention in recent years. The special band topology endows Weyl materials with specific electronic states, which are often topologically protected and immune to environmental perturbations. However, recent intensive investigations are mainly focusing on the basic physics of Weyl systems. This thesis is specialized in using chiral anomaly in low-dissipation and high-reliability electronics.

The chiral anomaly current can transport a long distance and can be manipulated by temperature, angle, light, magnetic field and gating voltages, which offers potentials of many kinds of electrons. Specifically, the chiral anomaly-based valley transport is robust can transport a long distance at room temperature, which is a good quantum platform for low-dissipation information processing.

The thesis investigates the applications of the valley for digital and analogue computing, two basic data transfer and communication systems. (1) Digital computing can solve problems by processing information in a discrete form (binary, 0 and 1). Digital computing is good at numerical calculations and logic functions. The field-effect transistor is the basic device of digital computing. High performance and low power consumption are important for modern digital computing systems. It is quite necessary to adopt new device physics because charge transistors are running into their performance limit. Chiral anomaly current is low-dissipation and arises from the non-trivial Berry curvature, which is highly sensitive to the position of Fermi level. Thus, it is potential to apply electrical gating to achieve a high ON/OFF transfer curve with low static consumption. Since chiral anomaly is strongly dependent on the gating voltage, magnetic field and the relative angle between magnetic and electrical fields, multiple-input logic functions (beyond "AND" and "OR") can be achieved. (2) Analogue computing is one of the most important trends in the next decade of semiconductors research and development. The neuromorphic analogue hardware-based computing paradigm has been regarded as one potential solution with high energy efficiency and unique cognitive functions. The working mechanism of both the brain/nerve relies on the movement of ions, which inspires researchers to emulate the neuromorphic functions with ionic devices. As there is a coexistence of the electrical double layer and ion intercalation mechanisms in our valley devices, we can require suitable output curves for specific neuromorphic computing to process static and dynamic information.

1.3 Structure of thesis

The chapters of this thesis are organized as follows:

Chapter 1: Introduction. This chapter points out the importance of addressing the power consumption issue and introduces the basic transport characteristic of non-charge information carriers, followed by their applications in electronics. Then, the background of chiral anomaly mechanisms is introduced. Moreover, this chapter presents the significance of the thesis: chiral-anomaly based devices for efficiently processing information. Last, the organization of the thesis is introduced.

Chapter 2: Manipulation of chirality to achieve field-effect electronics with Dirac semimetal $PtSe_2$. Angle-dependent negative, planar Hall effects and non-local transport are observed. Tuning the energy separation between the Dirac point and the Fermi level can efficiently change the chiral conductivity-based curves. An analogue output curve can be achieved when considering the magnetic field and chiral conductivity. The transfer curve in $PtSe_2$ devices shows more than 10^3 ON/OFF ratio by electrostatic gating. With electric and magnetic fields as input signals, the chirality devices can also exhibit basic logic functions (AND, OR).

Chapter 3: Topological phase change FETs with Weyl semiconductor Te. Magneto-transport experiments of Weyl semiconductor Te verify the presence of chiral anomaly current. By electrostatic modulation, topological transistors can switch between low-dissipation, highly conductive ON-state and the trivial charge transport OFF-state. There is high negative magnetoresistance (MR) up to -90%, indicating that the low-dissipation chiral anomaly current contributes the majority part of the conductance. The ON/OFF ratio reaches ~10^8 under $\leq$ 2 V operating voltage, and the ON-state conductivity is up to 3.9×10^4 μS/μm.

Chapter 4: Room-temperature valley transistors to process static and dynamic information. Based on the chiral anomaly mechanism, room-temperature valley transistors with 7 μm diffusion length is achieved with Weyl semiconductor Te. The ON/OFF ratio is ~10^5 at room temperature by electrostatic gating. There is a coexistence of ion adsorption and intercalation mechanisms, which result in the output curves with tunable nonlinearity and retention time (timescale from 10^3 s to 10^{-2} s). The accuracy of processing static handwritten digits and dynamic icons from the Tokyo Olympic Games both reach 95%.

Chapter 5: Conclusion and outlook. In this chapter, the results in this thesis are systematically summarized. Meanwhile, future research based on low-dissipation carriers is proposed, such as p-n complementary valley circuits with multiple logic functions at room temperature.

1.4 References

1 The Decadal Plan for Semiconductors. *Semiconductor Industry Association and Semiconductor Research Corporation https://*[*www.src.org/about/decadal-plan/*](https://www.src.org/about/decadal-plan/) (2020).

2 Mak, K. F., Xiao, D. & Shan, J. Light–valley interactions in 2D semiconductors. *Nature Photonics* **12**, 451-460 (2018).

3 Jia, S., Xu, S.-Y. & Hasan, M. Z. Weyl semimetals, Fermi arcs and chiral anomalies. *Nature Materials* **15**, 1140-1144 (2016).

4 Kharzeev, D. E. The chiral magnetic effect and anomaly-induced transport. *Progress in Particle and Nuclear Physics* **75**, 133-151 (2014).

5 Xiong, J. *et al.* Evidence for the chiral anomaly in the Dirac semimetal Na_3Bi. *Science* **350**, 413-416 (2015).

6 Li, C.-Z. *et al.* Giant negative magnetoresistance induced by the chiral anomaly in individual Cd_3As_2 nanowires. *Nature Communications* **6**, 10137 (2015).

7 Li, H. *et al.* Negative magnetoresistance in Dirac semimetal Cd_3As_2. *Nature Communications* **7**, 10301 (2016).

8 Parameswaran, S., Grover, T., Abanin, D., Pesin, D. & Vishwanath, A. Probing the chiral anomaly with nonlocal transport in three-dimensional topological semimetals. *Physical Review X* **4**, 031035 (2014).

Chapter 2 Field-effect chirality devices with Dirac semimetal $PtSe_2$

Conventional field-effect transistors (FETs) based on the charge degree of freedom suffer from Joule heat dissipation. Chiral anomaly current in Weyl physics is low-dissipation over a long distance, but it still lacks effective ways to control its transport for the FETs. Here, the chirality-based FETs with Dirac semimetal $PtSe_2$ are designed and demonstrated. Angle-dependent negative magnetoresistance and the planar Hall test are used to evidence the chiral anomaly current in our sample. The ON/OFF ratio reaches more than 10^3 by efficient electrostatic control over chiral anomaly current with ionic liquid. Essential logic functions are achieved due to the device's high sensitivity to the magnetic field, rotation angle and electrostatic gating. The pumped chiral charges can be compensated by inter-valley transport through quasi-momentum transfer. The nonlocal valley transport is width- and length-dependent and can be effectively modulated by the magnetic and electrical fields. This work provides an efficient way to control the transport of chirality degree of freedom, which can significantly reduce power consumption compared with state-of-the-art charge-based transistors.

2.1 Introduction

Conventional field-effect transistors (FETs) rely on charge transport in semiconductors, which inevitably results in heat dissipation and leads to ever-increasing power consumption in integrated circuits[1,2]. It is highly imperative to develop low-power devices by adopting the carrier transport mechanisms with low-dissipation characteristics, for example, low-dissipation information carrier (spin, valley, *etc.*)[3,4]. Massless Weyl fermions have unusual transport properties that are resulted from chiral properties and the exotic trajectories against external perturbations[5-7]. Chirality of the Weyl fermion is defined by the sign of spin projection along the momentum direction (**Figure 2.1a**)[8]. Under the parallel electric field (***E***), chiral charge is pumped between two Weyl nodes with opposite chiralities under non-zero Berry curvature, leading to chiral current throughout the whole sample, a so-called chiral anomaly.

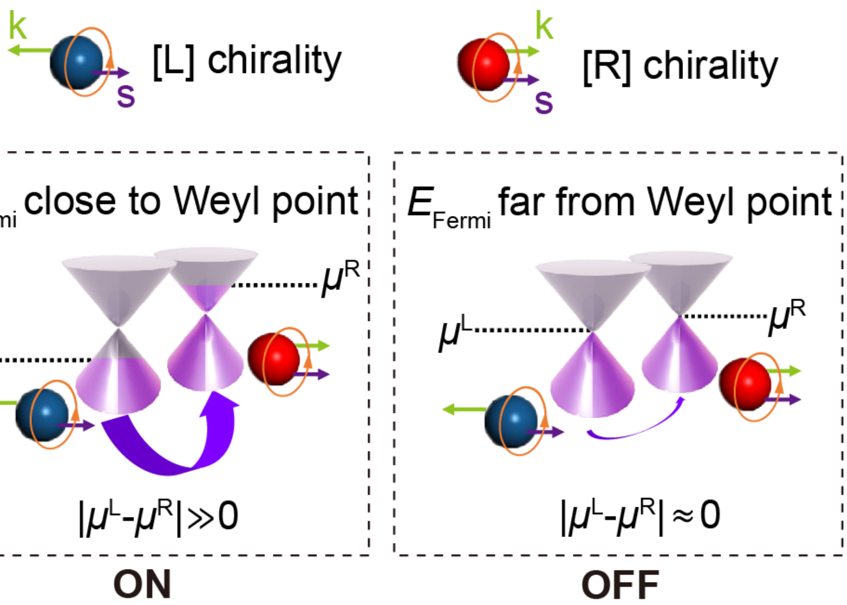

Figure 2.1 Chiral anomaly current in Dirac semimetal. "ON" state: E_{Fermi} is close to the Weyl point and $|\mu^L- \mu^R| \gg 0$. "OFF" state: E_{Fermi} away from the Weyl point and $|\mu^L- \mu^R| \approx 0$.

The pumped chiral charges can be compensated by inter-valley transport through quasi-momentum transfer (**Figure 2.2**)[9,10].

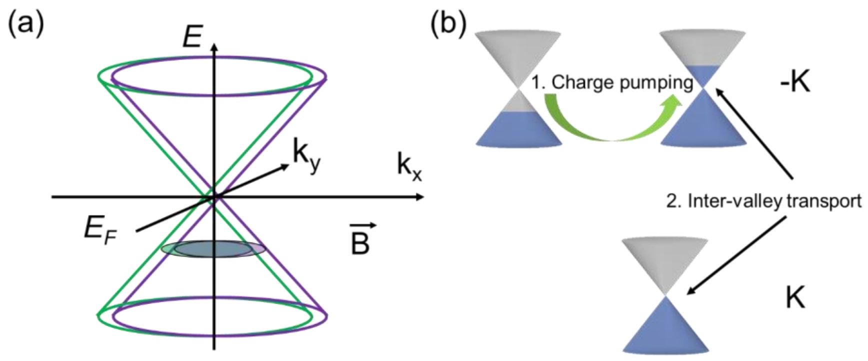

Figure 2.2 Chiral-anomaly related valley transport in the Dirac semimetal. (a) Sketch of a Dirac cone consisting of two slightly displaced massless Weyl nodes with distinct left-handed and right-handed chirality under the applied magnetic field. (b) Two typical processes in the chiral anomaly situation: charge pumping and inter-valley transport.

In analogy to the valley degree of freedom in two-dimensional (2D) transition metal dichalcogenides, the chirality degree of freedom in topological semimetals can also potentially carry and encode information without heat dissipation[8,11-13]. Because the chirality imbalance is closely related to the transfer of chirality between fermions and gauge fields with the global topology[12,14], the topologically protected chiral current is low-dissipation even under strong interactions over long distance[15], much longer than the transport of valley[16] or spin[17] (typical micrometre level). Compared with the successful modulation of valley/spin transport by optical or electrical stimulation[2,16], the manipulation of chiral anomaly current in three-dimensional (3D) topological semimetals still remains elusive, because it lacks effective ways to modulate chiral anomaly current in semimetals.

In this work, we investigate the field-effect chiral anomaly characteristics by adopting Dirac semimetal $PtSe_2$, which possesses a 3D Dirac point in the conduction band. Electrostatic modulation with ionic liquid allows efficiently tuning the energy separation between the Dirac point and the Fermi level as well as the chiral conductivity. The chirality devices exhibit analogue characteristics of FETs with an ON/OFF ratio higher than 10^3 under external field modulation and can perform basic logic functions. Chiral anomaly nonlocal valley transport can also be effectively modulated by both magnetic and electric fields. Our results provide another potential way for low-power electronics with a new degree of freedom.

2.2 Experimental section

Device fabrication

$PtSe_2$ crystal was purchased from HQ Graphene. Flakes were mechanically exfoliated onto the Si substrate with 300-nm-thick SiO_2. The electron beam lithography technique was used to define the pattern of metal electrodes. Metal contacts were prepared by sequential thermal evaporation of Cr (10 nm) and Au (80 nm) at the rate of 0.2 Å /s and 0.5 Å /s, respectively. As there is a layer-dependent bandstructure in transition-metal dichalcogenides[18,19], we have chosen thick enough samples to show bulk-like band structures. To observe the obvious angle-dependent negative MR, the thicknesses of used $PtSe_2$ flakes were selected in the range of 8-15 nm, determined by Bruker Multimode atomic force microscopy. To prepare devices for nonlocal valley transport measurement, a relatively low beam current (30 pA, 20 kV) was adopted in the focused ion beam process to avoid obvious damage to the sample.

Magnetotransport measurement

The temperature-dependent magnetotransport measurements were carried out by Physical Property Measurement System (PPMS) from Quantum Design. The direction of the magnetic field was reversed to correct the additional Hall (or resistive) voltage signals due to the misalignment of the voltage leads during the MR (or Hall resistivity) measurements. The ionic liquid DEME-TFSI can induce ~10^{14} cm^{-2} carriers to form the equivalent capacitance of ~10 mF/cm^2. A droplet of ionic liquid was used to cover the surface of $PtSe_2$ and the side gate electrode. Then, the sample was kept under high vacuum with 9×10^{-8} Torr for 24 h. The side ionic liquid gate pattern was prepared much larger than $PtSe_2$ film for efficient gating. The initial gating temperature was set at 220 K, which is close to the freezing point of DEME-TFSI. Gating at this temperature allows effective gating and avoids damaging the sample.

Materials characterizations

Scanning electron microscope spectrum and energy dispersive X-ray spectroscopy were acquired by JEOL Model JSM-6490. Raman spectrum was performed with a Witec alpha300 R (laser source, 532nm).

First-principles calculations

We employ the first principle simulation method to investigate the precise band structure of bulk $PtSe_2$ material. Quantum-Espresso code[20-22] was used to perform the calculation. We used the projector-augmented-wave (PAW) method[23] to describe the atomic potential, and generalized-gradient-approximation (GGA) Perdew-Bruke-Ernzerhof[24] exchange-correlation functional. The energy cutoff for plane waves was set to 80 Ryd to precisely describe the highly localized d-orbitals in the system. The $PtSe_2$ crystal was firstly fully optimized under k-sampling density 16 × 16 × 12, and then band structure was calculated. To search for possible Dirac point in the whole Brillouin zone (BZ), we used Wannier90 code[25] to project the 16 × 16 × 12 band structure onto maximally-localized Wannier orbitals[26] and generate a tight-binding model. With this tight-binding model, it is possible to search for tens of thousands of k-points in the BZ. After the Dirac point in the conduction band was identified by this tight-binding model, it was further verified by Quantum-Espresso.

2.3 Results and discussion

Two Weyl nodes with distinct left-handed and right-handed chiralities are split from the Dirac cone under magnetic field ($\boldsymbol{B}$), where the distance between two nodes in momentum space is determined by the magnitude of $\boldsymbol{B}$[7,27]. The chemical potential imbalance between left-handed and right-handed chiralities drives the formation of chiral current with the presence of parallel $\boldsymbol{E}$, which results in chiral current, and exhibits negative longitudinal magnetoresistance (MR)[28-30]. We can manipulate chirality (valley-like degree of freedom) in semimetals by controlling chiral anomaly strength, which arises from non-zero Berry curvature (Ω) and is closely related to the energy separation ($\Delta\varepsilon$) between Fermi level (E_{Fermi}) and Weyl/Dirac point (**Figure 2.3a**). Therefore, chiral anomaly current can be efficiently tuned through the field-effect shift of Fermi level of semimetals. When $\boldsymbol{B} \,//\, \boldsymbol{E}$, the chiral anomaly conductivity (σ_{chiral}) can be described according to Equation (2.1)[31]:

$$\sigma_{chiral} = \frac{e^4 v_{\mathrm{F}}^3 \tau B^2}{4\pi^2 \hbar \Delta\varepsilon^2} \tag{2.1}$$

where e is the electron charge, v_F is the Fermi velocity near the Weyl points, τ is the inter-valley scattering time, and $\hbar$ is the Planck constant. It is noteworthy that this Equation (2.1) is only restricted to a relatively low magnetic field according to theoretical analysis[32]. In experiments, most researchers validated Equation (2.1) below 6T.

The 3D Dirac point in Dirac semimetal comprises two degenerated Weyl nodes with opposite chirality, which can be separated in momentum space by breaking time-reversal symmetry under $\boldsymbol{B}$. Without the electric field $\boldsymbol{E}$, the right- and left-handed fermions in Weyl nodes have equal chemical potential ($\mu^R = \mu^L$), and the chiral charge at a single Weyl node is conserved. With parallel $\boldsymbol{B}$ and $\boldsymbol{E}$, the left-handed (L) chirality will be pumped into right-handed (R) chirality, resulting in the unequal chemical potential ($\mu^R \neq \mu^L$), as illustrated in **Figure 2.3b**. In such a case, a net current is generated and transported over the sample due to chiral imbalance. The current form is $J_c = \frac{e^2 B}{4\pi^2 \hbar^2 \mathrm{c}}(\mu^{\mathrm{R}} - \mu^{\mathrm{L}})$, where J_c is named as chiral current[7,10]. Experimentally, we can test the positive chiral magnetic conductivity described by the Equation (2.1).

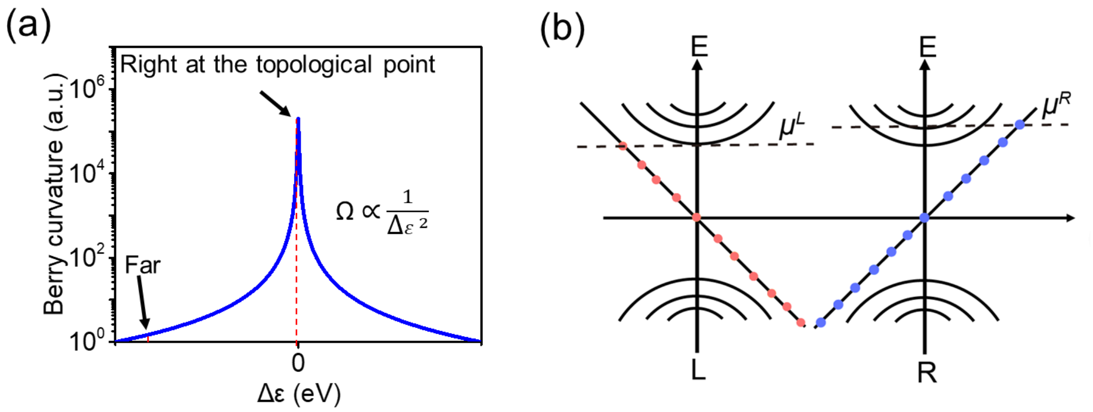

Figure 2.3 Berry curvature and charge pumping process in the Dirac semimetal. (a) Distribution of the square of the Berry curvature as a function of the relative energy Δε, the energy between Dirac/ Weyl point and Fermi level. There is the most substantial Berry curvature when the Fermi level is at the Dirac/Weyl point. As Fermi level moves away from the Dirac/Weyl point, Berry curvature decays remarkably. (b) Schematic illustration of the charge pumping process between left-handed and right-handed fermions arises from the chiral anomaly.

Chiral current can be used for low-dissipation information processing by field-effect modulation. When E_{Fermi} is close to the Weyl point, the larger difference ($|\mu^L - \mu^R| \gg 0$) in chemical potentials between left- (μ^L) and right-handed (μ^R) fermions results in a strong chiral current ("ON" state); when E_{Fermi} is away from the Weyl point, chiral anomaly strength decays remarkably, leading to $|\mu^L - \mu^R| \approx 0$ and negligible chiral current ("OFF" state). **Figure 2.4** schematically illustrates the chirality-based field-effect device, where chiral current flows in the direction parallel to $\boldsymbol{B}$ and $\boldsymbol{E}$.

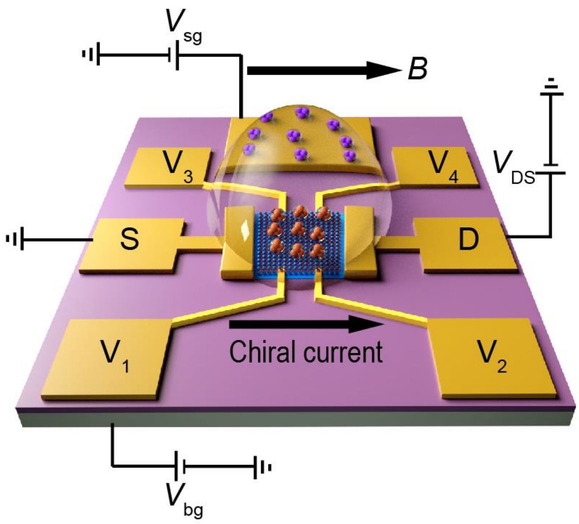

Figure 2.4 Illustration of a device structure for chirality-based field-effect devices.

The operations and characteristics of chirality-based devices are similar to those in charge-based FETs (**Figure 2.5a**). Electrostatic gating can tune the carrier density and E_{Fermi} of Dirac semimetals, thus modulating $\Delta\varepsilon$ and chiral anomaly current in chirality-based devices (**Figure 2.5b**). To effectively modulate chiral anomaly current, it is quite necessary to choose topological materials with suitable $\Delta\varepsilon$. If $\Delta\varepsilon$ is close to zero, Equation (2.1) becomes invalid [33]. If $\Delta\varepsilon$ is too large, σ_{chiral} is too weak for detection, and it is hard to efficiently manipulate σ_{chiral} to achieve high ON/OFF ratio.

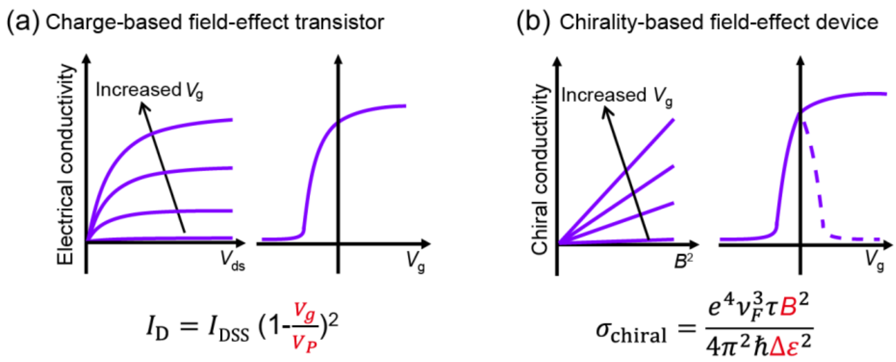

Figure 2.5 Chirality-based field-effect device. (a) Schematic curves of electrical conductivity in charged-based field-effect transistor as a function of V_{ds} (left panel) and

V_g (right panel), respectively. In an n-type depletion-mode FET, I_D is the drain current, $\boldsymbol{I_{DSS}}$ is maximum saturation current, and V_P is the pinch-off voltage at which the channel closes. (b) Schematic curves of chiral conductivity in chirality-based field-effect devices as a function of B^2 (left panel) and V_g (right panel), respectively. For the curve as a function of V_g, the dash line refers to the situation that the Fermi level can easily cross the topological point due to too small $\Delta\varepsilon$, while the solid line shows the case that Fermi level cannot cross the topological point.

Layered $PtSe_2$ exhibits strongly layer-dependent bandgap, from semiconducting to semimetallic characteristics, as the thickness increases (**Figure 2.6**)[19,34].

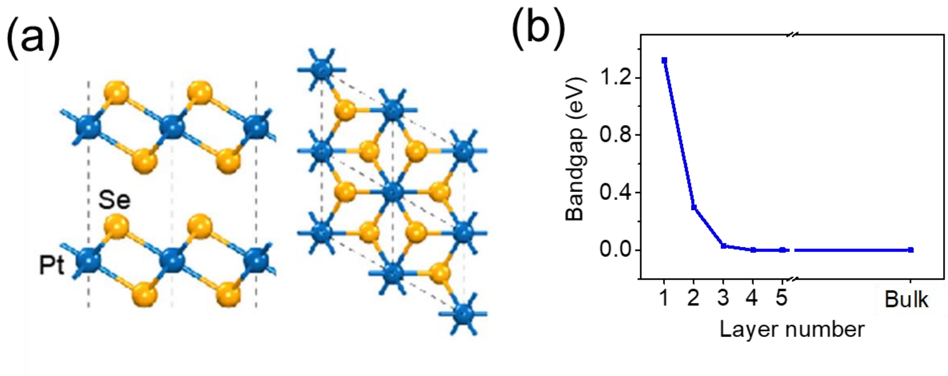

Figure 2.6 Crystal structure and layer-dependent bandgap of $PtSe_2$. (a) Schematic image of the crystal structure of $PtSe_2$ from the side view (left panel) and top view (right panel). (b) The layer-dependent bandgap of $PtSe_2$ calculating by the path M-K-G-M of the Brillion zone.

According to density functional theory (DFT) calculations (**Figure 2.7**), the conduction band of bulk $PtSe_2$ shows a cone around the point D (0, 0.32, 0.5) (in the units of 2π/a, 2π/a, 2π/c, respectively) along with three different directions: in parallel with G-M path, perpendicular to G-M path, and along the k_z direction, different from the Dirac cone previously verified in the valence band of $PtSe_2$[18,19].

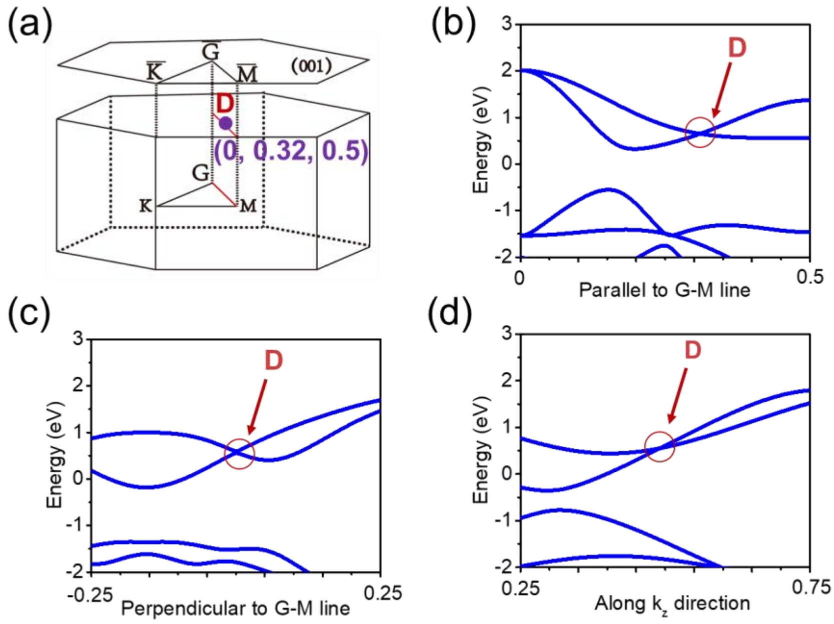

Figure 2.7 Band structures of bulk $PtSe_2$ along different paths. (a) Brillion zone of bulk $PtSe_2$ and the proposed Dirac point is marked as “D”. (b) Parallel to G-M line. (c) Vertical to G-M line. (d) Along k_z direction. Dirac cones point around D (0, 0.32, 0.5) in three different orthogonal directions.

3D band structures demonstrate that the bands are linearly dispersing across these nearly straight cones (**Figure 2.8)**, resulting from *d* orbitals of Pt and *p* orbitals of Se. This fourfold degenerated point can be described by the 4×4 Dirac matrix, identified as the Dirac fermion. The Dirac point is positioned ~0.55 eV above the Fermi level in the conduction band of pristine bulk $PtSe_2$, which is quite different from the Dirac point in the valence band (with ~1.1 eV below the Fermi level) of $PtSe_2$ reported in previous works[35,36]. The Dirac point in the valence band exhibits large $\Delta\varepsilon$, which makes it extremely difficult to modulate chiral anomaly current. In this work, we focus on the investigation of the Dirac point in the conduction band of $PtSe_2$ to achieve field-effect chirality devices.

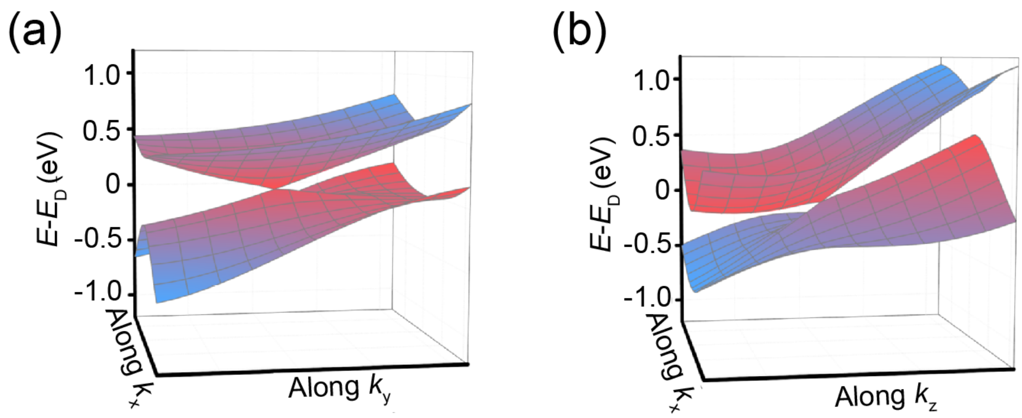

Figure 2.8 Three dimensional band structures around the Dirac point. (a) Three-dimensional band structures along k_x and k_y. (b) Three-dimensional band structures along k_x and k_y, where k_x is the direction vertical to G-M line, and k_y is the direction parallel to G-M line. The variable range is +/-0.1(unit 2π/a).

The presence of defects in materials can dramatically change the position of the Fermi level. For example, the Fermi level of Dirac semimetal Na_3Bi can be lifted up by ~0.4 eV because of defects[29]. The energy-dispersive X-ray spectrum of the $PtSe_2$ crystal (**Figure 2.9)** reveals Se deficiency (roughly $PtSe_{1.93}$), which increases electron density and upshifts Fermi level close to the Dirac point in the conduction band.

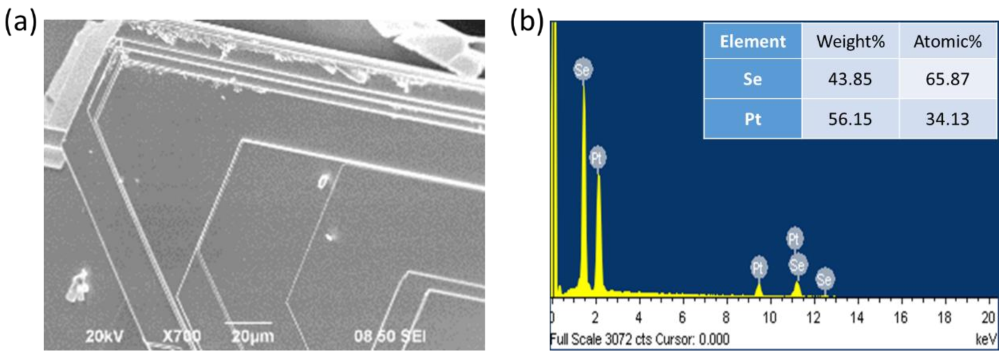

Figure 2.9 The element ratio of the used $PtSe_2$ flake. (a) Scanning electron microscope image of $PtSe_2$ crystal flake. (b)The EDX spectrum of $PtSe_2$ crystal indicates that Se is deficient.

The crystalline orientation of $PtSe_2$ can be identified according to the angle between two straight edges[37]. Angle-dependent negative MR is a strong indicator of the chiral anomaly in $PtSe_2$ devices. Other possible factors for negative MR, such as weak localization and current jetting, were carefully examined and excluded (Supporting Note III and Figure S9, Supporting Information). We input current along the sharp zigzag edges of $PtSe_2$, and perform an angle-dependent MR test by rotating the angle (θ).

We performed Hall measurements through a 6-terminal structure (**Figure 2.10a**). The thickness of sample #1 is ~12 nm (**Figure 2.10b**). Both sample #1 and bulk $PtSe_2$ crystal have two pronounced peaks around 183 and 206 cm^{-1} (**Figure 2.10c**), and the typical peak at around 230 cm of few-layer $PtSe_2$ is absent[19], supporting that sample #1 have bulk-like properties. Sample #1 exhibits the metal-like resistance-temperature curve (**Figure 2.10d**) when the temperature decreases from 300K to 2K. There is angle-dependent MR (**Figure 2.10e**) when varying from 21.16% ($\boldsymbol{B} \perp \boldsymbol{E}$) to -0.97% ($\boldsymbol{B} /\!/ \boldsymbol{E}$).

Figure 2.10f shows the positive MR of sample #1 as a function of the magnetic field under $\boldsymbol{B}\perp\boldsymbol{E}$ at 2K.

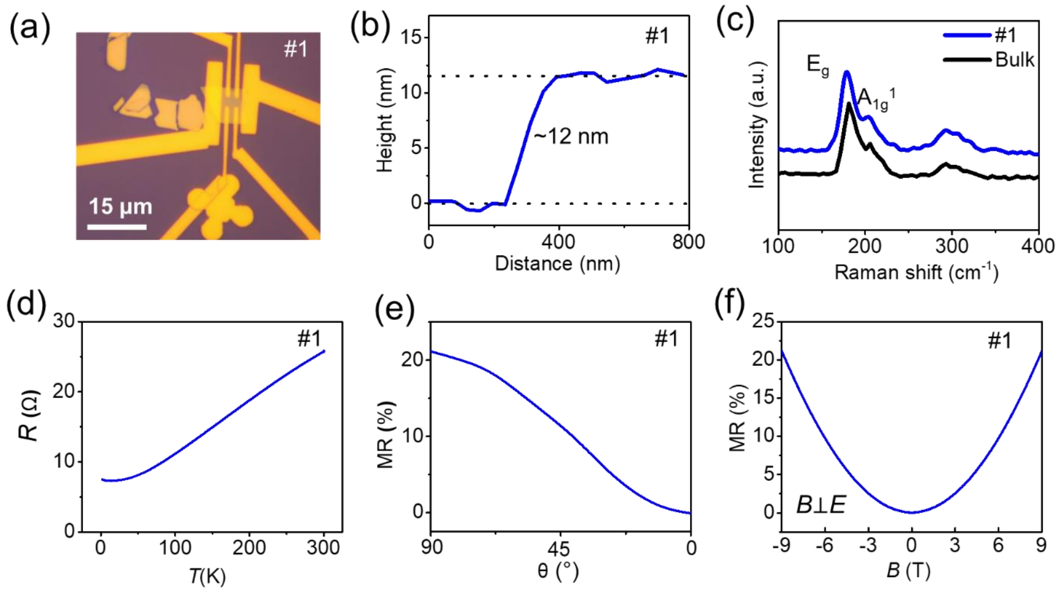

Figure 2.10 Hall bar device #1. (a) The optical microscope photograph. (b) Tested height of the sample (~12 nm) determined by AFM. (c) Raman spectra of sample #1 and bulk $PtSe_2$ crystal. Two pronounced peaks around 183 and 206 cm^{-1} can be observed when and the typical peak at around 230 cm^{-1} of few-layer $PtSe_2$ is absent. (d) Metallic temperature-resistance curve. (e) Angle-dependent MR varying from 21.16% ($B\perp E$) to -0.97% ($B \mathbin{/\!/} E$). (f) MR as a function of magnetic field under $B\perp E$ at 2K.

There is n-type Hall resistance in sample #1 from 300 K to 2 K (**Figure 2.11a**). The carrier density (n) can be extracted according to $n=\frac{1}{R_H e}, R_H=\frac{Rd}{B}$, where R_H is the Hall coefficient, e is the electron charge, R is tested Hall resistance and d is the sample thickness. The electron concentration of the $PtSe_2$ sample decrease from 3.15 $\times10^{21}$ cm^{-3} (n_{2D} = 3.78×10^{15} cm^{-2}) at 300 K to 8.50×10^{20} cm^{-3} (n_{2D} =1.02 ×10^{15} cm^{-2}) at 2 K. There is negative MR (-0.97%) when $\boldsymbol{B} \mathbin{/\!/} \boldsymbol{E}$ (**Figure 2.11b**). The chiral conductivity (σ_{chiral}) as a function of $\boldsymbol{B}^2$ (the inset of **Figure 2.11b**) can be well fitted by a straight line, in good consistency with the chiral anomaly Equation (2.1).

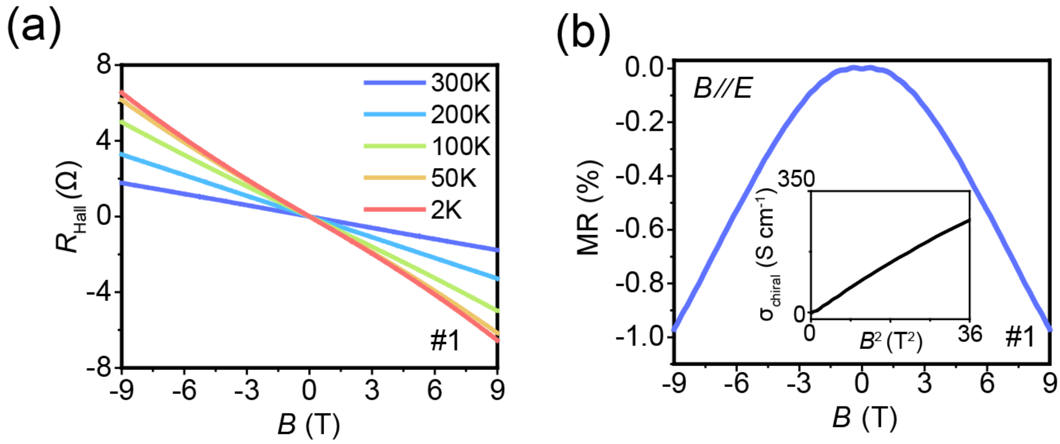

Figure 2.11 Hall resistance and magnetotransport behaviour of #1. (a) The Hall resistance varies from 300K to 2K of sample #1. (b) Magnetotransport behaviours of Hall bar device #1 under *B//E* at 2K. MR$=\frac{\boldsymbol{R(B)-R(0)}}{\boldsymbol{R(0)}}\times \mathbf{100\%}$, where $\boldsymbol{R(0)}$ is the resistance at zero magnetic field, and $\boldsymbol{R\ (B)}$ is the resistance under *B*. The inset is σ_{chiral} as a function of B^2, extracted according to $\sigma_{chiral} = \sigma - \sigma_0$, where σ is the conductivity under specific magnetic field, and σ_0 is the conductivity without magnetic field.

High electron carrier density is repeatable in another Hall sample #2 (**Figure 2.12a**). Lv *et al.* reported that the measured Hall carrier density of 1.5×10^{20} cm^{-3} in Weyl semimetal $WTe_{1.98}$ could upshift the Fermi level by 60~120 meV[38]. We calculate the upshift of Fermi level in our samples based on the carrier density from Hall data by referring to the previous work[38]. The density of state (DOS) of bulk $PtSe_2$ with/without electron doping are both calculated. The DOS of pristine $PtSe_2$ with electron doping was achieved by adding the extra electrons based on the tested n-type Hall carrier density 8.50×10^{20} cm^{-3} at 2 K. Finally, we can get two DOS spectra with similar shapes and clear upshift of Fermi level after electron doping. The DFT calculation based on the measured carrier density shows that the upshifted Fermi level gives rise to small $\Delta\varepsilon$ (**Figure 2.12b**), which allows the observation of chiral anomaly conductivity in our samples without applying gate voltage.

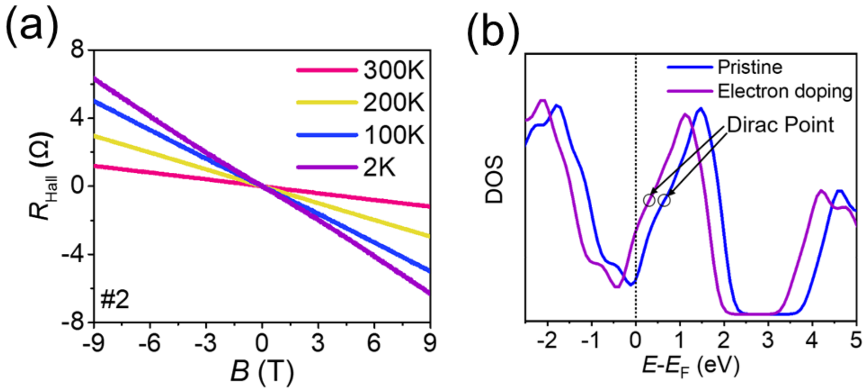

Figure 2.12 The downshift of the Dirac point of electron-doped $PtSe_2$. (a) Hall resistance of sample #2 at different temperatures. The Hall resistance increases as the temperature vary from 300K to 2K. (b) The density of states of pristine and electron-doped $PtSe_2$. The circles highlight the position of the Dirac point in pristine and electron-doped $PtSe_2$.

The inset of **Figure 2.13** shows a 4-terminal $PtSe_2$ (sample #3, ~13 nm thickness) for investigating chiral anomaly related angle-dependent MR behaviours. There are angle-dependent negative MR behaviours in sample #3 at 2K (**Figure 2.13a**), exhibiting the maximum negative MR value (-0.82%) when $\boldsymbol{B} \parallel \boldsymbol{E}$. The negative MR is gradually suppressed after rotating θ away from $\theta = 0°$ ($\boldsymbol{B} \parallel \mathbf{E}$), and becomes positive at $\theta > 2°$ under 9 T (**Figure 2.13b**).

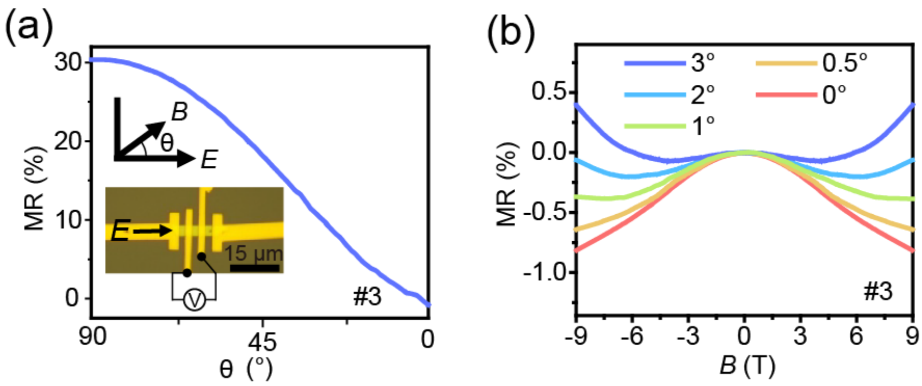

Figure 2.13 Angle-dependent longitudinal magnetic resistance of sample #3. (a) Angle-dependent longitudinal magnetic resistance of 4-terminal sample #3. Inset is the optical microscope photograph of a typical tested 4-terminal sample. (b) Longitudinal MR of sample #3 at small rotation angles near *B//E.*

For relatively thick sample #4 (~15 nm), it also shows angle-dependent negative MR, where the MR decreases from 36% (***B***⊥***E***) to -0.26% (***B***⁄⁄***E***) (**Figure 2.14**). It is noteworthy that the negative MR ratio of #4 under ***B***⁄⁄**E** is smaller than #3 because of the stronger positive MR background in a thicker sample.

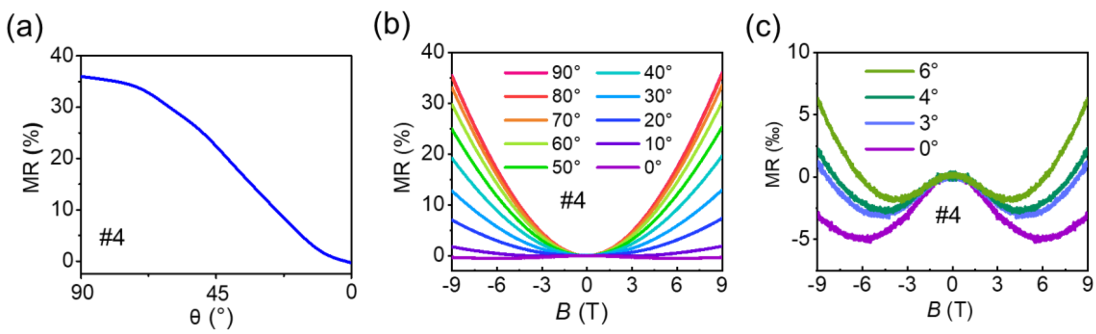

Figure 2.14 Angle-dependent negative longitudinal magnetic resistance of 4-terminal sample #4 (~15 nm) at 2K. When *B* // *E*, there is the strongest negative longitudinal magnetic resistance. As the angle gradually reduces, the negative magnetic

resistance becomes weaker. When $B \perp E$, the strongest positive magnetic resistance is about 36%.

For the thick samples (#5 with 160 nm and #6 with 180 nm), the resistance is as low as 1 Ω at 2 K and show positive MR at different angles (**Figure 2.15**). No observable negative under MR $B /\!/ E$ can be attributed to the strong background in thicker samples, as reported in previous topological semimetal works.

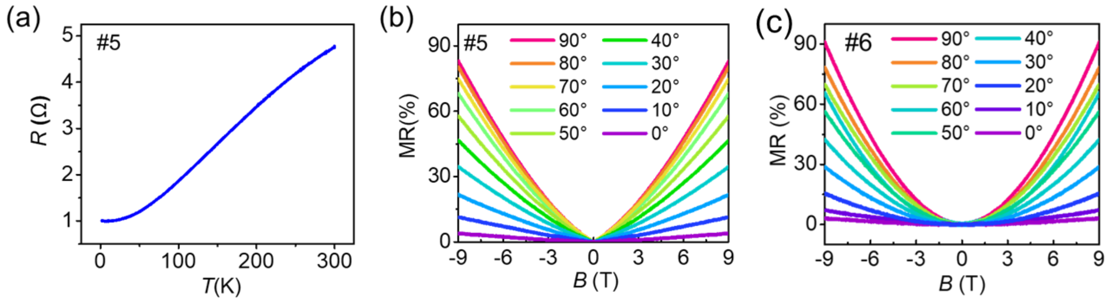

Figure 2.15 Magnetotransport behaviours in thick samples with more than 160 nm.

The thickness-dependent MR behaviours under $\boldsymbol{B /\!/ E}$ and $\boldsymbol{B \perp E}$ are summarized in **Table 2.1**, which exhibits that it is quite necessary to adopt the samples with suitable thickness to observe chiral anomaly. We performed magnetotransport tests on more than 10 $PtSe_2$ samples (8-15 nm), which show reproducible negative MR characteristics induced by chiral anomaly. It is noteworthy that thin $PtSe_2$ samples (*e.g.*, sample #1 in **Figure 2.11b**) with relatively weak background conductance provides a good platform for investigating field-effect chiral devices.

Table 2.1 Summary of thickness-dependent MR.

Sample number	Thickness	MR under $B \perp E$	MR under $B // E$
#12	4 nm	+10.5%	+0.8%
#9	8.5 nm	+8.45%	-4.50%
#1	12 nm	+21.16%	-0.97%
#3	13 nm	+25.22%	-0.82%
#4	15 nm	+36.10%	-0.26%
#11	90 nm	+53.15%	+0.75%
#5	160 nm	+83.15%	+3.84%

Another strong evidence for the observation of chiral anomaly is the planar Hall effect (PHE)[39], *i.e.*, the appearance of an in-plane transverse voltage when there is an angle between the coplanar electric and magnetic fields. Such behaviours are rare for non-ferromagnetic systems. As shown in **Figure 2.16**, we have acquired the angular-dependent PHE results. The planar Hall resistance (R_{xy}) (**Figure 2.16b**) displays a periodic angular dependence of 180°. R_{xy} reaches its minimum and maximum value at ~45° and ~135°, respectively. Meanwhile, the in-plane resistance (R_{xx}) (**Figure 2.16c**) reaches its minimum and maximum value at 0° and 90°, respectively. More importantly, our tested data can fit well with the PHE resistance formula, respectively. These results provide strong evidence of observed chiral anomalies in our work.

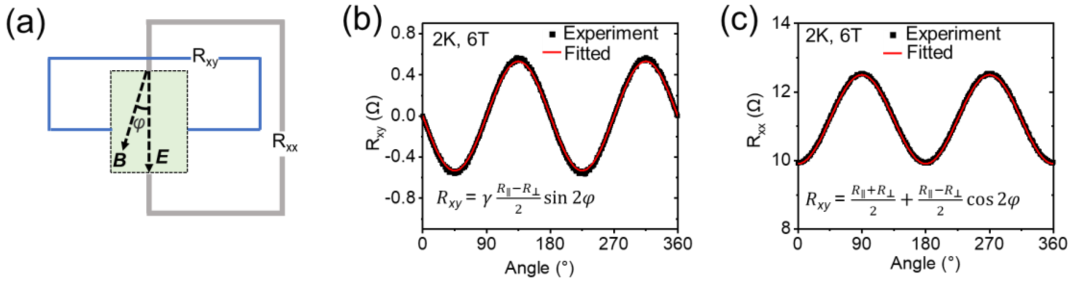

Figure 2.16 Planar Hall tests of our $PtSe_2$ sample. (a) Schematic of angular-dependent planar Hall tests. *B*, *E* and the sample are in the same plane. $\boldsymbol{\varphi}$ is the angle between *B* and *E*. (b) Angular dependence of the R_{xy}. (c) Angular dependence of the R_{xx}. Tested R_{xy} and R_{xx} are well fitted by $\boldsymbol{\gamma \frac{R_\parallel - R_\perp}{2} \sin 2\varphi}$ and $\boldsymbol{\frac{R_\parallel + R_\perp}{2} + \frac{R_\parallel - R_\perp}{2} \cos 2\varphi}$, respectively. $\boldsymbol{\gamma}$ is the ratio of the width to the length of the prepared Te device, $\boldsymbol{R_\parallel}$ is longitudinal MR under $\boldsymbol{B \parallel E}$, and $\boldsymbol{R_\perp}$ is longitudinal MR under $\boldsymbol{B \perp E}$. The tests were carried out at 2K under 6T.

As σ_{chiral} is strongly affected by $\Delta\varepsilon$, electrostatic modulation can be used to change the Fermi level and chiral anomaly conductivity. Due to the high equivalent capacitance of ~10 mF cm^{-2}, ionic liquid has been reported for effectively modulating the carrier density in transition metal dichalcogenides, which can tune the carrier density by two orders of magnitude from 2×10^{12} cm^{-2} to 1.4×10^{14} cm^{-2} in MoS_2 [40]. By applying ionic liquid gating (**Figure 2.17**), ions are driven to the channel surface, forming ultrahigh electrical double layer capacitance. I_g is relatively stable when temperature decreases from 220 K to 2 K. I_g is less than 0.2 nA during this cooling down process, suggesting a negligible damage effect (*e.g.*, surface electrochemical reaction) on the sample.

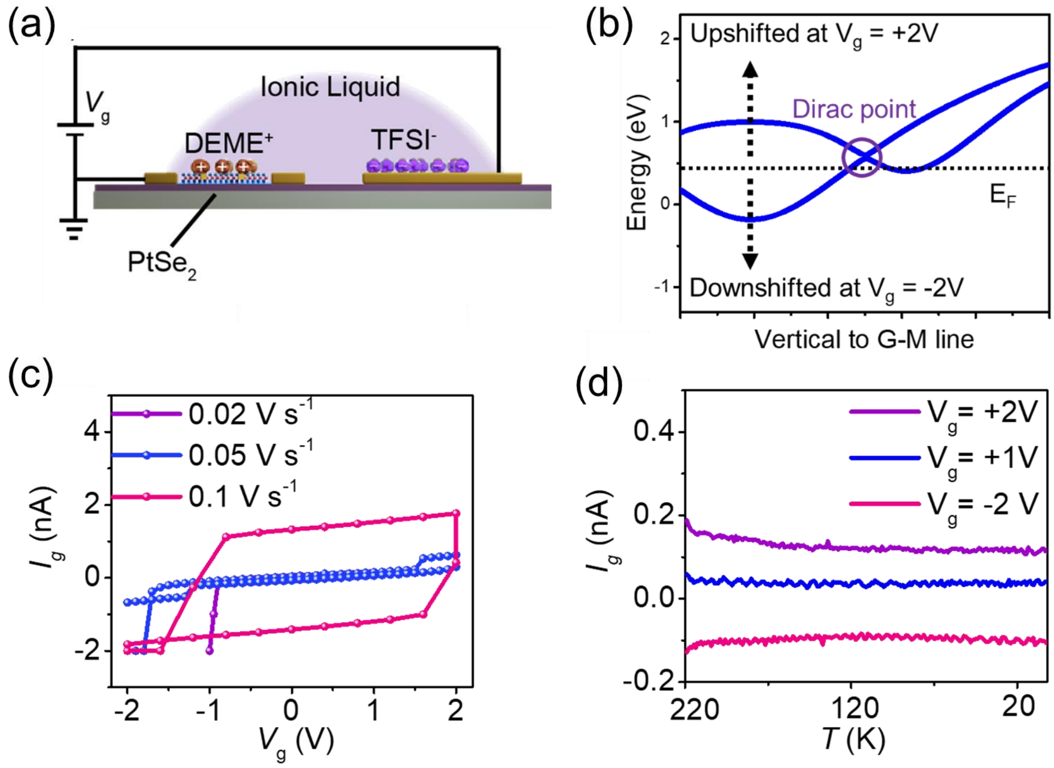

Figure 2.17 The manipulation of the chiral anomaly in $PtSe_2$ semimetal. (a) Schematic of gating $PtSe_2$ by the ionic liquid. (b) The shift of energy gap between E_F and Dirac point. The position of the Fermi level can be tuned by applying different V_g. (c) I_g-V_g curve of the ion liquid gating at 220K. The faster scanning (0.1 V s^{-1} vs 0.02V s^{-1}) rate leads to a larger hysteresis loop because of the effective movement of ions under gating, which is common in ionic liquid gating FET devices. (d) I_g-T curves for sample #7 under different V_g.

Resistance-temperature measurements on sample #8 (**Figure 2.18)** show that different gating voltage (V_g) can affect the electrical conductivity of the $PtSe_2$, suggesting the shift of carrier density and Fermi level. Specifically, +2V gating can reduce resistance, while -2V gating can increase the resistance, indicating the successful shift of the Fermi level. Meanwhile, there is no significant change of resistance at V_g= 0 after applying V_g= -2V and V_g= +2V.

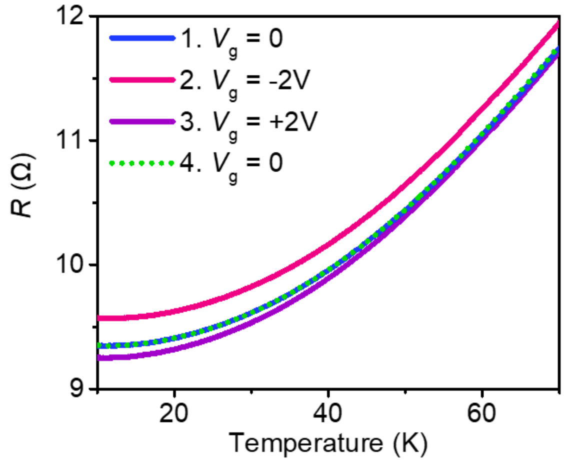

Figure 2.18 Resistance-temperature curves of sample #8. The testing order is V_g= 0, V_g= -2V, V_g= +2V and V_g= 0.

For sample #9 (~8.5 nm), negative MR is remarkably suppressed under negative V_g and is enhanced under positive V_g (**Figure 2.19a**) due to the change of $\Delta\varepsilon$. A positive V_g can upshift the Fermi level, while V_g downwardly shifts the Fermi level (Figure S14b, Supporting Information). The linear relationship between σ_{chiral} and $\boldsymbol{B^2}$ (**Figure 2.19b**) fits well with Equation (2.1). **Figure 2.19c** shows the chiral conductivity as a function of V_g, in analogy to the transfer curve of depletion-mode charge-based FETs. The ON/OFF ratio of chiral conductivity reaches 780 with electrical gating (+2V vs -2V) under 6T. Because of the high electron carrier density of the semimetal $PtSe_2$ at V_g = 0 and relatively large $\Delta\varepsilon$, it is difficult to drive the E_{Fermi} across the Weyl point, thus resulting in the saturated characteristics similar to the transfer curve of conventional FETs.

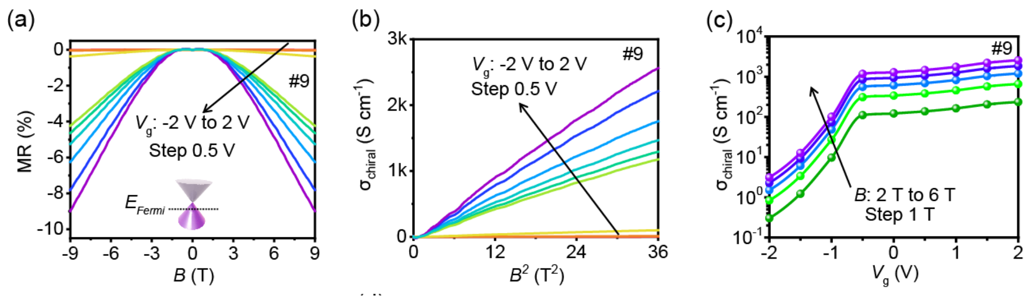

Figure 2.19 Chirality-based field-effect $PtSe_2$ device. (a) Chiral anomaly-based negative MR curves as a function of B under different V_g. The inset shows that E_{Fermi} is below the Dirac point of $PtSe_2$ at V_g=0. (b) σ_{chiral} as a function of B^2 under different V_g.

Due to the thinner thickness (~8 nm), the MR of sample #10 changes from nearly 0 (V_g = -2V) to -6.97% (V_g = +2V), exhibiting much stronger electrostatic modulation than sample #4 (**Figure 2.20**). The σ_{chiral} of sample #10 under different gating is also linearly fitted (**Figure 2.20c),** and both electric and magnetic field can modulate it (**Figure 2.20d**), with the ON/OFF ratio of 1.0×10^3 (electrical field, +2V vs -2V, at 9T) and 1.1×10^3 (magnetic field, 2T vs 9T, at V_g= 2V), respectively.

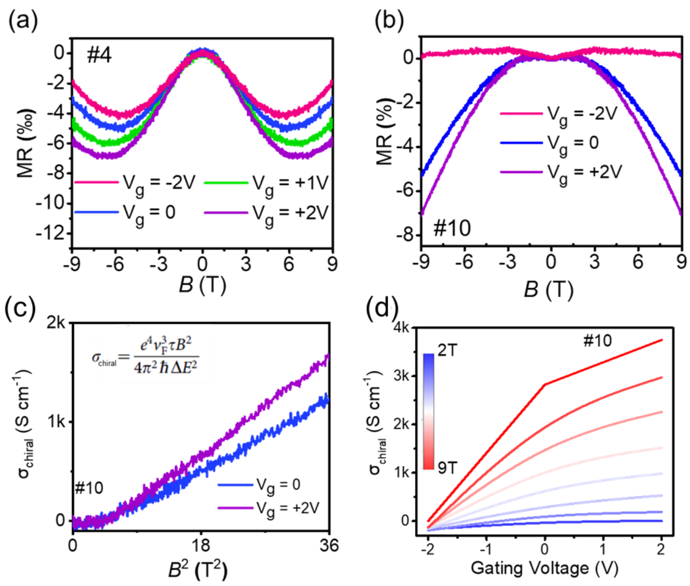

Figure 2.20 Chiral anomaly-based negative magnetic resistance curves as a

function of *B* at different gating voltages under *B* // *E*. Both samples #4 and #10 show V_g-dependent magnetic resistance curves.

In contrast, it is hard to tune the MR in thick sample #11 (~90 nm) from positive to negative MR because of the strong positive MR background (Figure S20, Supporting Information). At another angle θ = 10°, we can successfully achieve field-effect MR in sample #4 (Figure S21, Supporting Information) by combining θ, V_g and ***B*** to manipulate chiral anomaly.

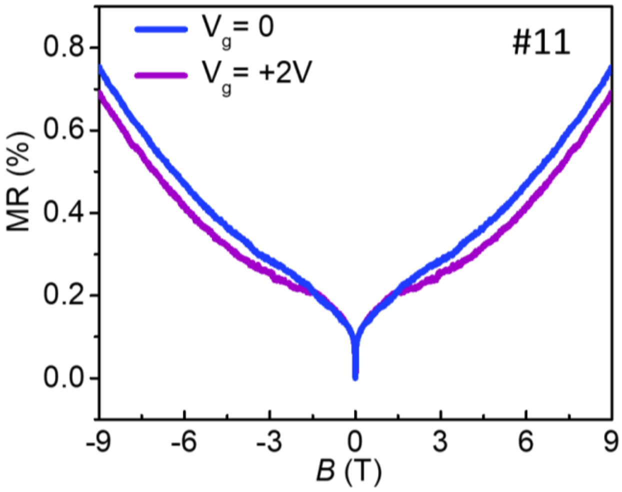

Figure 2.21 Gating thick $PtSe_2$ sample #11 (~90 nm) through the ionic liquid.

Chirality-based devices can perform logic operations (**Figure 2.22**), like the charge-based FETs[41]. We can define V_g and ***B*** as two inputs and σ_{chiral} as output. For the $input_1$ (***B***), logic “0” and “1” are defined as ***B*** ≤ 4.5 T and ***B*** > 4.5T, respectively; for the $input_2$ (V_g), logic “0” and “1” are defined as $V_g \leq 0$ V and $V_g > 0$ V, respectively. AND logic function (**Figure 2.22a**) can be realized on sample #9 (~8.5 nm), where the output “0” corresponds to $\sigma_{chiral} \leq 780$ S cm^{-1}, and “1” corresponds to $\sigma_{chiral} > 780$ S cm^{-1}. Only when both $input_1$ and $input_2$ are logic “1”, the output is “1”. In addition to two-input AND and OR logic operations, the AND-OR logic function with three inputs can also be achieved by combining θ, V_g and $\boldsymbol{B}$ as the input signals (**Figure 2.22b**).

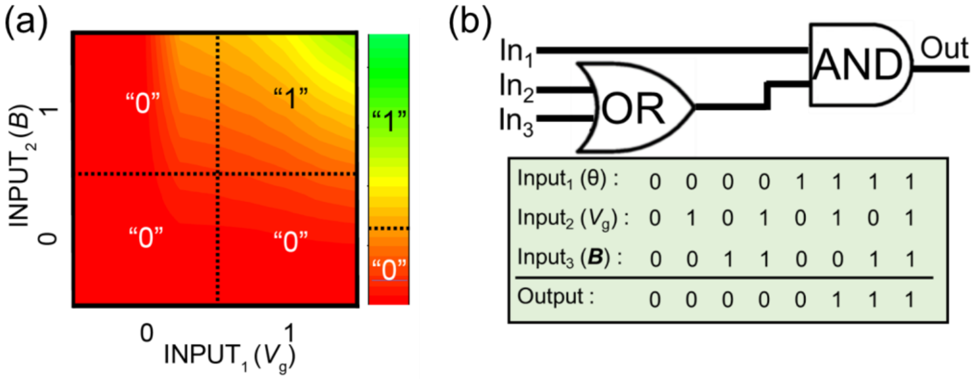

Figure 2.22 Demonstrations of logic operations based on chiral anomaly current. (a) Demonstration of AND logic gate. INPUT 1 is "0" for $B \leq 4.5$T, and "1" for $B >$ 4.5T. INPUT 2 is "0" for $V_g \leq 0$ V, and "1" for $V_g > 0$ V. OUTPUT is "0" for $\sigma_{chiral} \leq$ 780 S cm^{-1}, and "1" for $\sigma_{chiral} > 780$ S cm^{-1}. (b) OR-AND logic operation. We define θ as input 1 with 0°as "0" and 10° as "1". V_g is defined as input 2 with $V_g = +2$V as "0" and -2V as logic "1". Input 3 is B with 3 T as logic "0", and 6 T as logic "1". The output is defined as "0" corresponding to the negative MR, and "1" corresponding to the positive MR.

Nonlocal valley transport can distinguish the negative MR from conventional MR anisotropy, and provide another strong indicator to corroborate chiral anomaly in topological semimetals. We performed nonlocal valley transport through the "H" configuration (**Figure 2.23a**), in which constant current is injected, and a valley imbalance is generated under parallel $\boldsymbol{E}$ and $\boldsymbol{B}$. This valley polarized states will diffuse over the sample like spin and can be detected in the detector region with sufficient long distance (μm level)[8,10,42]. Nonlocal valley transport strength can be quantitatively characterized by width-dependent ratio and length-dependent exponential decay. We fabricated the devices in the "H" configuration with the same length (2 μm) and different widths (**Figure 2.23b**) to characterize the width-dependent valley transport. Constant current is applied through terminal 1-2, while terminal 3-4 (2 μm width) and 5-6 (1 μm width) are used to detect the voltage. The magnetic field can effectively modulate the nonlocal resistance of the device (**Figure 2.23c**). The pure nonlocal resistance is extracted by removing background from stray current[43] (Supporting Note VI, Supporting Information) according to $R_{\text{valley}} = -k_{34}Re^{-L/L_v}$ for terminal 3-4, where R_{valley} reveals the strength of valley signal, R is the local resistance, L_v is the valley diffusion length, and k is a dimensionless coefficient. The width ratio of terminal 5-6 to 3-4 is 0.5. Therefore, the corresponding theoretical nonlocal valley ratio should be 0.50 (dash line). The measured ***B*** dependent $R_{56\text{–NL}}$/ $R_{34\text{–NL}}$ ratio is close to this theoretical value (the inset of **Figure 2.23c**).

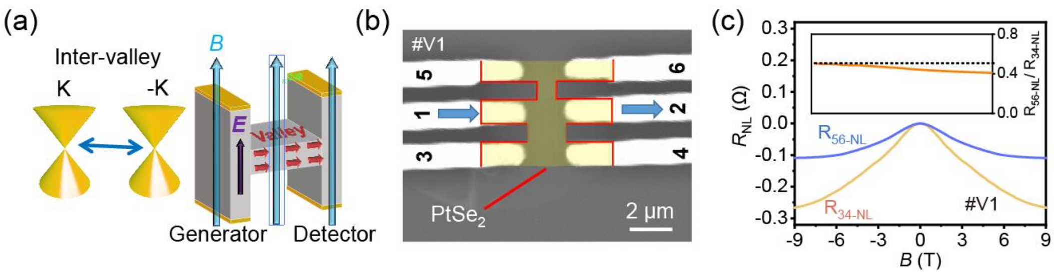

Figure 2.23 Chirality-based nonlocal width-dependent valley transport. (a) Schematic view of the inter-valley diffusion between different valley positions (±K), compensating the chiral anomaly induced charging pumping process. (b) Scanning electron microscopy of sample #V1. It has the same channel length of 2 μm and different channel width of 2 μm (terminal 3-4), and 1 μm (terminal 5-6), respectively.

(c) Width-dependent valley transport in sample #V1 under the magnetic field modulation. The inset shows the ratio of $R_{56\text{-}NL}/R_{34\text{-}NL}$ as a function of B at different temperatures. The dash line corresponds to the theoretical value of 0.50.

We also fabricated the device with different lengths (**Figure 2.24a**). By applying constant current through terminal 1-2, we tested the voltage of terminal 3-4 (2 μm length), 5-6 (4 μm length) and 7-8 (7 μm length). With the increase of lateral length L (the length between current injected terminal pair and nonlocal detecting pairs of terminals), the nonlocal resistance (**Figure 2.24b)** decays rapidly.

Valley transport strength coefficient α_{NL} is used to quantitatively describe the strength of the nonlocal response[8,10]:

$$\alpha_{\mathrm{NL}} = \left|\frac{\mathrm{R_{NL}}}{\mathrm{R_L}}\right| \propto e^{-\frac{L}{L_{\mathrm{v}}}} \qquad (2)$$

where L_{v} is the inter-valley scattering length. The semi-log plot of α_{NL} against the lateral length L (**Figure 2.24c**) clearly shows that the tested α_{NL}can be fitted by line, in which α_{NL} decays exponentially as the lateral length L increases from 2 μm, 4 μm to 7 μm, consistent with the valley transport Equation (2.1). The valley signal is relatively strong even for the 4 μm length[8,10].

In addition to the magnetic field, electrical gating can also be applied to manipulate the nonlocal valley transport, which shows that the tested α_{NL} can be well tuned ant fitted by a straight line under $V_g = \pm 2$V (**Figure 2.24c**). The good linear fitting in the semi-log curve supports that the tested valley signals decay exponentially under $V_g = \pm 2$V, fitting well with Equation (2.1). Both magnetic and electric field can successfully tune the strength of valley transport in different device geometries.

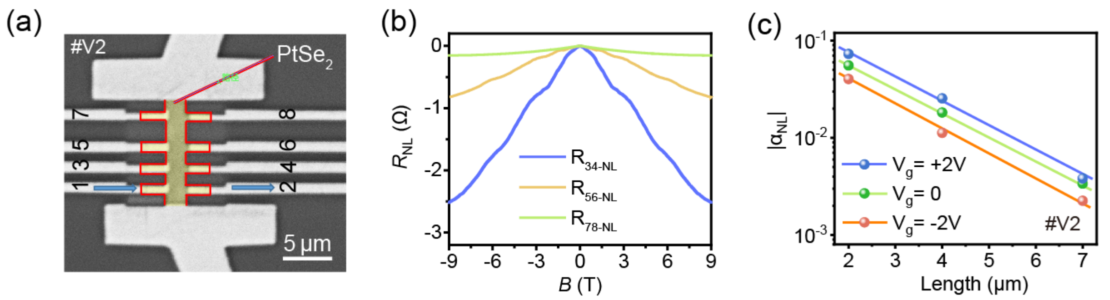

Figure 2.24 Length-dependent valley transport. (a) Scanning electron microscopy of sample #V2. It has the same channel width 2 μm and different channel length from 2 μm (terminal 3-4), 4 μm (terminal 5-6) to 7 μm (terminal 7-8). (b) Length-dependent valley transport sample #V1 under the magnetic field modulation. (c) Electrical modulation of length-dependent valley transport strength through ionic liquid gating. The calculated valley strength $|\alpha_{NL}|$ as a function of diffusion length shows that $|\alpha_{NL}|$ decays exponentially with the increasing of lateral length.

2.4 Summary

In summary, we design and demonstrate a device structure for controlling chirality transport in Dirac semimetal $PtSe_2$. The chirality-based field-effect devices show efficient electrostatic control over chiral anomaly current with an ON/OFF ratio of more than 10^3, and realize basic logic functions. The nonlocal valley transport is width- and length-dependent, which can also be effectively modulated by magnetic and electrical fields. This study provides a way to control the transport of chirality degree of freedom, which has the potential for significantly reducing power consumption compared with state-of-the-art charge-based FETs.

2.5 References

1 Wang, J. *et al.* in *2018 IEEE International Electron Devices Meeting (IEDM).* 22.23. 21-22.23. 24 (IEEE).

2 Mak, K. F., Xiao, D. & Shan, J. Light–valley interactions in 2D semiconductors. *Nature Photonics* **12**, 451-460 (2018).

3 Sui, M. *et al.* Gate-tunable topological valley transport in bilayer graphene. *Nature Physics* **11**, 1027-1031 (2015).

4 Seyler, K. L. *et al.* Signatures of moiré-trapped valley excitons in $MoSe_2$/WSe_2 heterobilayers. *Nature* **567**, 66-70 (2019).

5 Qiu, G. *et al.* Quantum Hall effect of Weyl fermions in n-type semiconducting tellurene. *Nature Nanotechnology* **15**, 585-591 (2020).

6 Lin, B.-C. *et al.* Electric control of Fermi arc spin transport in individual topological semimetal nanowires. *Physical Review Letters* **124**, 116802 (2020).

7 Li, C.-Z. *et al.* Giant negative magnetoresistance induced by the chiral anomaly in individual Cd_3As_2 nanowires. *Nature Communications* **6**, 10137 (2015).

8 Ma, Q. *et al.* Direct optical detection of Weyl fermion chirality in a topological semimetal. *Nature Physics* **13**, 842-847 (2017).

9 Zhang, C.-L. *et al.* Signatures of the Adler–Bell–Jackiw chiral anomaly in a Weyl fermion semimetal. *Nature Communications* **7**, 10735 (2016).

10 Parameswaran, S., Grover, T., Abanin, D., Pesin, D. & Vishwanath, A. Probing the chiral anomaly with nonlocal transport in three-dimensional topological semimetals. *Physical Review X* **4**, 031035 (2014).

11 Jia, S., Xu, S.-Y. & Hasan, M. Z. Weyl semimetals, Fermi arcs and chiral anomalies. *Nature Materials* **15**, 1140-1144 (2016).

12 Kharzeev, D. E. The chiral magnetic effect and anomaly-induced transport. *Progress in Particle and Nuclear Physics* **75**, 133-151 (2014).

13 Ma, J. *et al.* Nonlinear photoresponse of type-II Weyl semimetals. *Nature Materials* **18**, 476-481 (2019).

14 Kharzeev, D. E. & Liao, J. Chiral magnetic effect reveals the topology of gauge fields in heavy-ion collisions. *Nature Reviews Physics*, 1-9 (2020).

15 Zhang, N. *et al.* Magnetotransport signatures of Weyl physics and discrete scale invariance in the elemental semiconductor tellurium. *Proceedings of the National Academy of Sciences* **117**, 11337-11343 (2020).

16 Li, L. *et al.* Room-temperature valleytronic transistor. *Nature Nanotechnology* **15**, 743-749 (2020).

17 Song, P. *et al.* Coexistence of large conventional and planar spin Hall effect with long spin diffusion length in a low-symmetry semimetal at room temperature. *Nature Materials* **19**, 292-298 (2020).

18 Zhao, Y. *et al.* Extraordinarily strong interlayer interaction in 2D layered PtS_2. *Advanced materials* **28**, 2399-2407 (2016).

19 Zhao, Y. D. *et al.* High-Electron- Mobility and Air-Stable 2D Layered $PtSe_2$ FETs.

Advanced Materials **29**, 1604230 (2017).

20 Giannozzi, P. *et al.* QUANTUM ESPRESSO: a modular and open-source software project for quantum simulations of materials. *Journal of physics: Condensed matter* **21**, 395502 (2009).

21 Giannozzi, P. *et al.* Advanced capabilities for materials modelling with Quantum ESPRESSO. *Journal of Physics: Condensed Matter* **29**, 465901 (2017).

22 Giannozzi, P. *et al.* Quantum ESPRESSO toward the exascale. *The Journal of Chemical Physics* **152**, 154105 (2020).

23 Blöchl, P. E. Projector augmented-wave method. *Physical review B* **50**, 17953 (1994).

24 Perdew, J. P., Burke, K. & Ernzerhof, M. Generalized gradient approximation made simple. *Physical review letters* **77**, 3865 (1996).

25 Mostofi, A. A. *et al.* wannier90: A tool for obtaining maximally-localised Wannier functions. *Computer physics communications* **178**, 685-699 (2008).

26 Marzari, N., Mostofi, A. A., Yates, J. R., Souza, I. & Vanderbilt, D. Maximally localized Wannier functions: Theory and applications. *Reviews of Modern Physics* **84**, 1419 (2012).

27 Li, H. *et al.* Negative magnetoresistance in Dirac semimetal Cd_3As_2. *Nature Communications* **7**, 10301 (2016).

28 Lu, H.-Z. & Shen, S.-Q. Quantum transport in topological semimetals under magnetic fields. *Frontiers of Physics* **12**, 127201 (2017).

29 Xiong, J. *et al.* Evidence for the chiral anomaly in the Dirac semimetal Na_3Bi. *Science* **350**, 413-416 (2015).

30 Sun, H.-P. & Lu, H.-Z. Quantum transport in topological semimetals under magnetic fields (II). *Frontiers of Physics* **14**, 33405 (2019).

31 Wang, Y. *et al.* Gate-tunable negative longitudinal magnetoresistance in the predicted type-II Weyl semimetal WTe_2. *Nature Communications* **7**, 13142 (2016).

32 Kaushik, S. & Kharzeev, D. E. Quantum oscillations in the chiral magnetic conductivity. *Physical Review B* **95**, 235136 (2017).

33 Fukushima, K., Kharzeev, D. E. & Warringa, H. J. Chiral magnetic effect. *Physical Review D* **78**, 074033 (2008).

34 Lin, X. *et al.* Intrinsically patterned two-dimensional materials for selective adsorption of molecules and nanoclusters. *Nature Materials* **16**, 717-721 (2017).

35 Li, Z., Zeng, Y., Zhang, J., Zhou, M. & Wu, W. Observation of negative longitudinal magnetoresistance in the type-II Dirac semimetal $PtSe_2$. *Physical Review B* **98**, 165441 (2018).

36 Sun, J. *et al.* Asymmetric Fermi velocity induced chiral magnetotransport anisotropy in the type-II Dirac semi-metal $PtSe_2$. *Communications Physics* **3**, 93 (2020).

37 Guo, Y. *et al.* Distinctive in-Plane Cleavage Behaviours of Two-Dimensional Layered Materials. *ACS nano* **10**, 8980-8988 (2016).

38 Lv, Y.-Y. *et al.* Experimental observation of anisotropic Adler-Bell-Jackiw anomaly in type-II Weyl semimetal $WTe_{1.98}$ crystals at the quasiclassical regime. *Physical review letters* **118**, 096603 (2017).

39 Nandy, S., Sharma, G., Taraphder, A. & Tewari, S. Chiral anomaly as the origin of the planar Hall effect in Weyl semimetals. *Physical review letters* **119**, 176804 (2017).

40 Ye, J. *et al.* Superconducting dome in a gate-tuned band insulator. *Science* **338**, 1193-1196 (2012).

41 Liu, C. *et al.* Small footprint transistor architecture for photoswitching logic and in situ memory. *Nature Nanotechnology* **14**, 662-667 (2019).

42 Kimura, T., Otani, Y., Sato, T., Takahashi, S. & Maekawa, S. Room-temperature reversible spin Hall effect. *Physical review letters* **98**, 156601 (2007).

43 Zhang, C. *et al.* Room-temperature chiral charge pumping in Dirac semimetals. *Nature Communications* **8**, 13741 (2017).

Chapter 3 Topological transistors with Weyl semiconductor

Modern electronics demands transistors with high performance and extreme energy efficiency. Charge-based transistors with conventional semiconductors greatly suffer from increasing heat dissipation because of carrier scattering. Here we show the topological transistors (TPCTs) with Weyl semiconductor (Te) for low-dissipation and highly conductive ON-state. By modulating the energy separation between Fermi level and Weyl point of Te, the device exhibits topological phase change between Weyl semiconductor and conventional one by electrostatic modulation. The ON-state possesses low-dissipation transport characteristics because of the global topology of gauge fields. The OFF-state exhibits trivial charge transport in the conventional semiconductor by moving Fermi level into the band gap. The TPCTs show a high ON/OFF ratio (10^8) under low gating voltage ($\leq$2 V), high ON-state conductivity (3.9×10^4 μS/μm), and long transport distance. Our studies provide alternative strategies for supplementing conventional charge-based electronics.

3.1 Introduction

The electron devices with conventional semiconductors significantly constrain computation energy efficiency because of unavoidable heat dissipation. Modern electronic systems require high-performance and low-power devices to meet the demand of their sustainable development. It is reasonably necessary to adopt new device physics to break the constraint of charge transport mechanism[1,2]. Researchers have investigated spin/valley as the information carriers for low-dissipation transport[3], which usually shows a low ON/OFF ratio of 10^1-10^3 and low driving current[4,5], partly because of the non-ideal polarizers and analysers[6] and insufficient manipulation of polarized carriers[4]. In addition to spin/valley, low-energy relativistic quasiparticles hosted in topological materials show potential for the information carrier with high energy efficiency, in which chiral anomaly current can exhibit topologically protected low-dissipation transport characteristics over long distance due to the global topology of gauge fields[7,8].

The Weyl/Dirac points usually present in semimetals with the crossing of the two bands of spin polarized bands. The high carrier density in topological semimetals makes it difficult to modulate the position of their Fermi level ($\boldsymbol{E}_{\mathbf{F}}$) and chiral anomaly current, which also results in high static power consumption. Recent works reveal that Te is a Weyl semiconductor[9,10], which possesses a band gap similar to conventional semiconductor and has Weyl points in the vicinity of valence/conduction bands[10]. These characteristics of Weyl semiconductor allow it to retain low-dissipation transport feature and efficiently modulate the chiral anomaly current. When the $\boldsymbol{E}_{\mathbf{F}}$ of Weyl semiconductor is close to the Weyl points, it exhibits low-dissipation and highly conductive characteristics like Weyl semimetals; while the $\boldsymbol{E}_{\mathbf{F}}$ is tuned in the band gap, it shows high resistance trivial states without conduction channel, like conventional insulators. In addition, the chiral anomaly current in topological materials can transport with centimeter scale [9], allowing the information to be transported over long distance without dissipation.

In this work, we design and demonstrate topological transistors (TPCTs) with Weyl semiconductor Te. The states of TPCTs can be switched between low-dissipation, highly conductive ON-state and the trivial charge transport OFF-state by electrostatic modulation. We verify the chiral anomaly characteristics of ON-state through magnetotrasnport measurement. The high negative magnetoresistance (MR) up to -90% indicates that the low-dissipation chiral anomaly current contributes the majority part of the conductance. The Te TPCT shows high ON/OFF ratio of $\sim 10^8$ under ≤ 2 V operating voltage and high ON-state conductivity (3.9×10^4 μS/μm), which exhibit higher ON-state conductivity than conventional charge-based transistors and much higher ON/OFF ratio than spin/valley transistors. This designed TPCT has the potential for significantly reducing power consumption and retaining high performance compared with state-of-the-art charge-based field-effect transistors (FETs).

3.2 Experiment section

Device fabrication

Te flakes were prepared by hydrothermal methods[11] and then transferred to the Si substrate with 300-nm-thick SiO_2. The electron beam lithography technique was used to define the pattern of metal electrodes. Metal contacts were prepared by thermal evaporation of Au (80 nm) at the rate of 0.3 Å /s under the vacuum of 3×10^{-7} Torr. To prepare TPCTs, we patterned Te flakes into a Hall bar configuration with a side gate electrode.

Device characterization

The electrical transport measurements were carried out by Physical Property Measurement System from Quantum Design and Keithley 4200. The direction of the magnetic field was reversed to correct the additional Hall (or resistive) voltage signals due to the misalignment of the voltage leads during the MR (or Hall resistivity) measurements.

A droplet of ionic liquid DEME-TSFI covers the surface of Te flake and the side gate electrode. The gating voltage between the side electrode and the channel can drive the movements of ions. Then, the device was kept under high vacuum with 6×10^{-8} Torr for 24 h. To avoid damaging the sample, the initial gating temperature was set at 220 K, close to the freezing point of ionic liquid DEME-TFSI.

PEO/$LiClO_4$ electrolyte was prepared by dissolving PEO and $LiClO_4$ in methanol with a mass ratio of 9: 1. After coating PEO/$LiClO_4$, the sample was heated at 80 °C for 10 minutes to remove the solvent and water. The testing temperature was set at 10 K.

Materials characterizations

Scanning electron microscope images and energy dispersive X-ray spectroscopy spectrum were acquired by JEOL Model JSM-6490. Raman spectrum was performed with a Witec alpha300 R (laser source, 532 nm).

First-principles calculations

The calculation of Berry curvature. The Berry curvature Ω_n is defined as Equation (3.1)[12]:

$$\Omega_n\left(\vec{k}\right) = -\mathrm{Im}\left\langle \nabla_{\vec{k}} u_{n\vec{k}} \right| \times \left| \nabla_{\vec{k}} u_{n\vec{k}} \right\rangle \tag{3.1}$$

In this expression $u_{n\vec{k}}$ denotes the periodic part of the *n*th Bloch state with the momentum $\vec{k}$. In practice, it is convenient to calculate the Berry curvature with the Kubo-formula[12,13]:

$$\Omega_n^i\left(\vec{k}\right) = -\sum_{n'\neq n} \frac{2\,\mathrm{Im}\left\langle \psi_{n\vec{k}} \middle| \upsilon_j \middle| \psi_{n'\vec{k}} \right\rangle \left\langle \psi_{n'\vec{k}} \middle| \upsilon_k \middle| \psi_{n\vec{k}} \right\rangle}{\left(\omega_{n'} - \omega_n\right)^2} \tag{3.2}$$

with *i, j, k*=x, y, z respectively, υ_j being the velocity operators, and $E_n\left(\vec{k}\right) = \hbar\omega_n$ being the energy dispersion. Then the sum of Berry curvatures over the occupied bands are:

$$\Omega^i\left(\vec{k}\right) = \sum_n f_n \Omega_n^i\left(\vec{k}\right) \tag{3.3}$$

where f_n is the Fermi-Dirac distribution function.

We calculated the Bloch states with the Quantum-Espresso code[14-16] and performed analysis on the Berry curvature of Te with the Wannier90 code[17]. The lattice structure of Te is first fully relaxed, and then the full band structure is calculated. The

Bloch functions are transformed into the Wannier representation, and the Berry curvature is obtained with Equation (3.1) and (3.2) along the high symmetry paths.

The band structure and density of states calculations were carried out using DFT implemented in the Vienna Ab initio Simulation Package (VASP)[18]. The Perdew-Burke-Ernzerhof-type generalized gradient approximation[19] and the projector augmented-wave (PAW) method were employed[20]. A plane-wave basis set with a default energy cutoff and the 16 × 16 × 12 k-point mesh was used. A 3×3×3 Te supercell was used to calculate the density of states with or without Te vacancies. After removing one Te atom (marked by the red circle) from the supercell, the vacancy density in the calculated supercell with Te vacancies is 1/81 (~1.23%).

3.3 Results and discussion

In the conventional FETs, the switching mechanism relies on the build-up and removal of inversion layer (**Figure 3.1a**). In the TPCT with Weyl semiconductor, the conduction paths can be switched between conventional charge transport and low-dissipation chiral anomaly current (**Figure 3.1b**). Electrostatic modulation allows to tune the position of $\boldsymbol{E}_F$ and trigger the topological phase change between Weyl and conventional semiconductor. When the electrical field is parallel to magnetic field (***E*//*B***), the non-zero Berry curvature in Dirac/Weyl materials causes the chiral charge to be pumped between two Weyl nodes with opposite chirality. This chiral anomaly current is dependent on the strength of non-zero Berry curvature[21]. The electrostatic modulation of the position of $\boldsymbol{E}_F$ can substantially affect the energy gap ($\Delta\varepsilon$) between $\boldsymbol{E}_F$ and the Weyl point, which determines the strength of Berry curvature ($\boldsymbol{\Omega}$) ($\boldsymbol{\Omega} \propto 1/\Delta\varepsilon^2$). Thus, we can electrostatically modulate the strength of Berry curvature and chiral anomaly current.

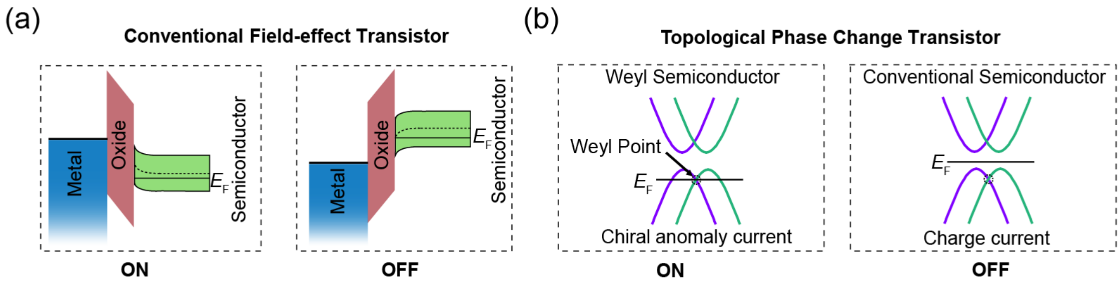

Figure 3.1 Comparison of working mechanisms. (a) The working mechanism of conventional field-effect transistors. (b) Working mechanism of topological transistors.

α-phase Te is a semiconductor with a band gap of approximately 0.32 eV, comprising of parallel-aligned helical chains with three Te atoms as the building block[22]. Along the high symmetric L-H path in the valence band (**Figure 3.2a**), Te has a pair of Weyl points that have opposite chirality (+1 for W_1 and -1 for W_2). W_1 is only ~0.2 eV below the $\boldsymbol{E}_F$, making it possible to efficiently modulate $\Delta\varepsilon$ and chiral anomaly current by electrostatic modulation. When the $\boldsymbol{E}_F$ is tuned close to the Weyl point (W_1) in Te, it exhibits a strong peak of ~40,000 (a.u.) of Berry curvature (right panel in **Figure 3.2b**) at the position of W_1 in momentum space according to theoretical calculations, corresponding to the ON-state dominated by chiral anomaly current. When the $\boldsymbol{E}_F$ is away from W_1 and in the band gap, the calculated Berry curvature is very weak of ~200 (a.u.) (left panel in **Figure 3.2b**) and the density of states is low, corresponding to high-resistance OFF-state.

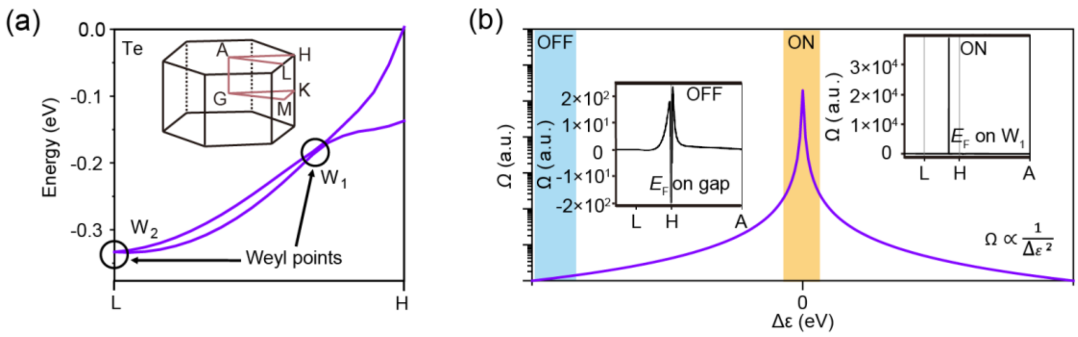

Figure 3.2 Weyl points and the operation of the topological transistors. (a) Weyl points in Te along the L-H path. Inset is the Brillion zone. (b) Berry curvature related working mechanism.

Angle-dependent negative MR is a representative signature of the chiral anomaly in Dirac/Weyl materials. In the case of $\boldsymbol{B}\cdot\boldsymbol{E} \neq 0$, the presence of chiral anomaly results in the observable negative MR. The as-grown Te usually has unintentional hole doping because of Te vacancies [9,10,23]. Our density functional theory (DFT) calculation results show that the vacancy in the Te crystal leads to strong hole doping (**Figure 3.3**), which makes the $\boldsymbol{E}_F$ of Te close to the Weyl point (W_1), consistent with reported Te work[9]. Thus, we can observe negative MR resulted from chiral anomaly current in self-hole-doped Te flakes without applying gate voltage.

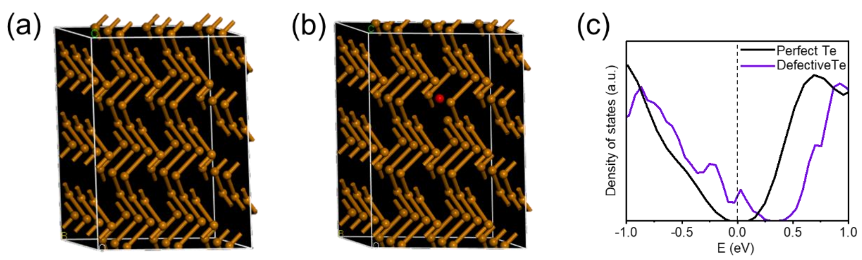

Figure 3.3 The crystal structure and density of states for the perfect and defective Te. (a) Schematic of the perfect Te supercell without defects (b) Schematic of the Te

supercell with one Te vacancy (marked by the red circle). (c) The density of states of the perfect and defective Te, respectively. The Fermi level shifts downwardly approximately 0.2 eV, close to the Weyl point (W_1) in the valence band.

We adopt the Te flakes with different thicknesses (**Figure 3.4**). There are optical images (**Figure 3.4** a1, a2, a3), atomic force microscopy (AFM) images (**Figure 3.4**b1, b2, b3), and thickness characterization curves (**Figure 3.4**c1, c2, c3) for different samples. Black arrow in the AFM image indicates the direction of the height-distance curve.

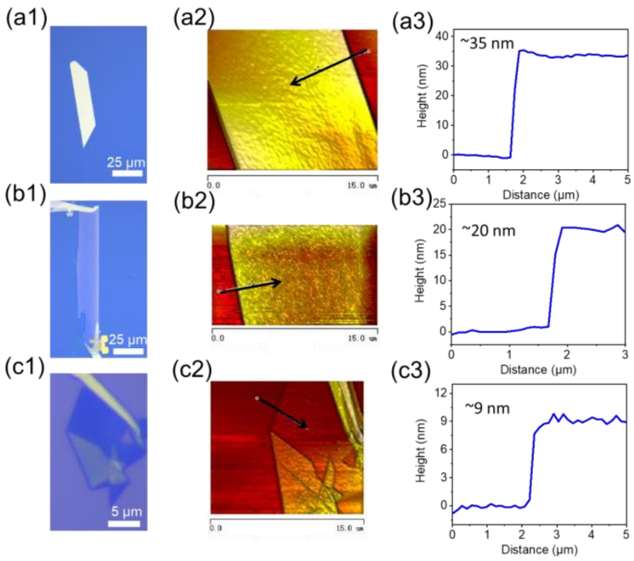

Figure 3.4 Representative Te flakes with different thicknesses.

There are angle-dependent MR from 0° (***B***//***E***) to 90° (***B***⊥***E***) on a sample with a thickness of ~30 nm (**Figure 3.5a**). The largest negative MR at 0° reaches -15.8%. **Figure 3.5b** shows the MR under precise rotation angles from 0° to 10°, exhibiting the monotonic decrease of negative MR with the increase of the angle. As the temperature gradually increases from 2 K to 100 K (**Figure 3.5c**), the negative MR becomes weaker because of thermal perturbation.

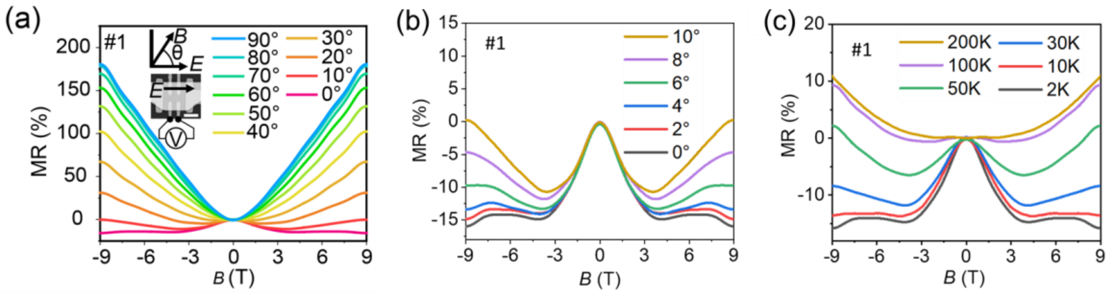

Figure 3.5 Angle- and temperature-dependent MR in sample #1. (a) Angle-dependent longitudinal MR in the prepared Te device. MR= $\frac{\boldsymbol{R(B)-R(0)}}{\boldsymbol{R(0)}} \times \mathbf{100\%}$, where $\boldsymbol{R(0)}$ is the resistance at zero magnetic field, and $\boldsymbol{R\ (B)}$ is the resistance under B. Inset is the scanning electron microscope image of the prepared Te device. The scale bar is 10 µm. (b) Precise angle-dependent negative MR from 0° to 10° at 2 K. (c) Temperature-dependent MR from 200 K to 2 K. Negative MR appears at 100 K under low magnetic field. Around 7.5 T, there is an angle- and temperature-dependent oscillation peak.

This angle-dependent negative MR characteristic is reproducible in other samples with similar thickness (**Figure 3.6**). In addition, we observe an oscillation peak at around 7.5 T (**Figure 3.5** & **Figure 3.6**), which is consistent with the first quantum oscillation peak at ~7.5 T[10].

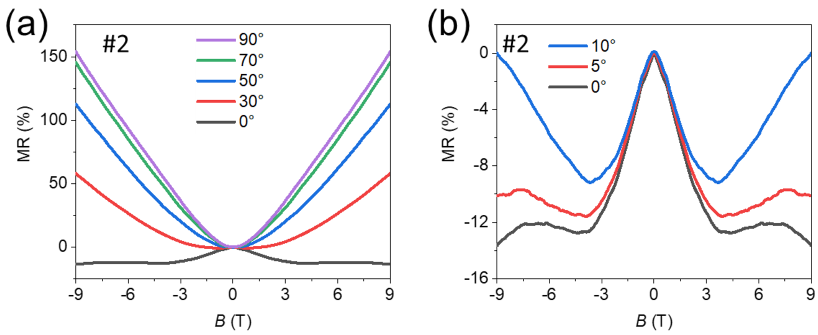

Figure 3.6 Angle-dependent negative MR in sample #2 at 2 K. (a) Angle-dependent

MR from 0° to 90°. (b) Precise angle-dependent MR from 0° to 10°. There is also an oscillation peak around 7.5 T.

More than 10 Te samples show reproducible negative MR characteristics under **B//E** (**Figure 3.7**). As the thickness of samples decreases, the negative MR becomes weaker, accordingly. MR of 70-nm-thick sample is -12.4% under 3 T and -61.7% under 9 T. MR of 28-nm-thick sample is -0.088% under 3 T and 0.28% under 9 T.

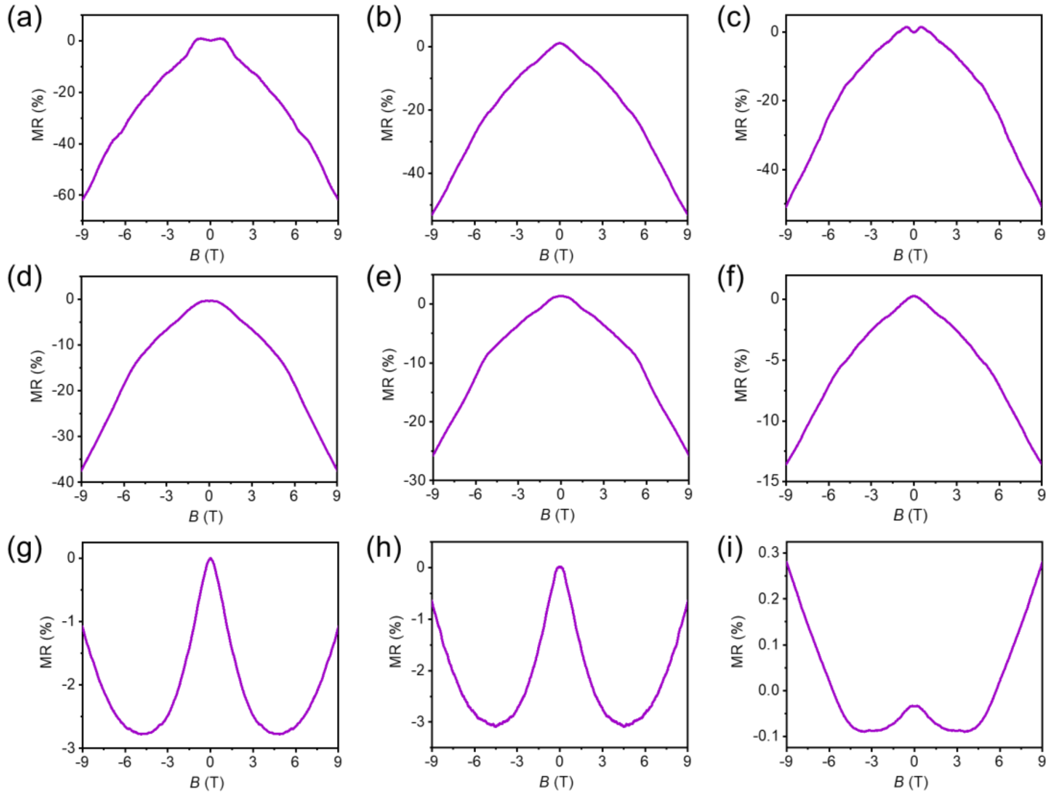

Figure 3.7 Reproducible negative MR characteristics under *B*//*E*. Te samples with the thickness ranging from (a) 70 nm to (f) 28 nm.

Furthermore, we rule out other possibilities that may cause the negative MR, such as the doping from magnetic elements (**Figure 3.8**) and current jetting (**Figure 3.9**). The MR behaviours for four-probe and two-probe magnetotransport tests are similar, indicating the negligible current jetting effect. It is noteworthy that current jetting effects usually exist in the thick bulk samples. The thickness of all tested Te flakes is tens of nanometers in this work.

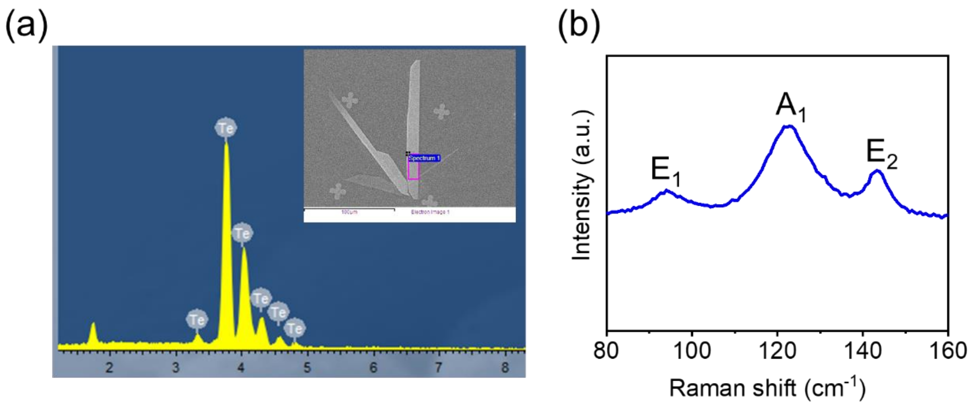

Figure 3.8 No observable magnetic elements doping in the Te sample. (a) EDX spectrum of the prepared Te flake. The inset is the captured scanning electron microscope image with a pink rectangle as the analytical area. (b) Raman spectrum clearly shows three typical peaks E_1 (94 cm^{-1}), A_1 (123 cm^{-1}) and E_2 (143 cm^{-1}), which are typical Raman peaks for Te sample.

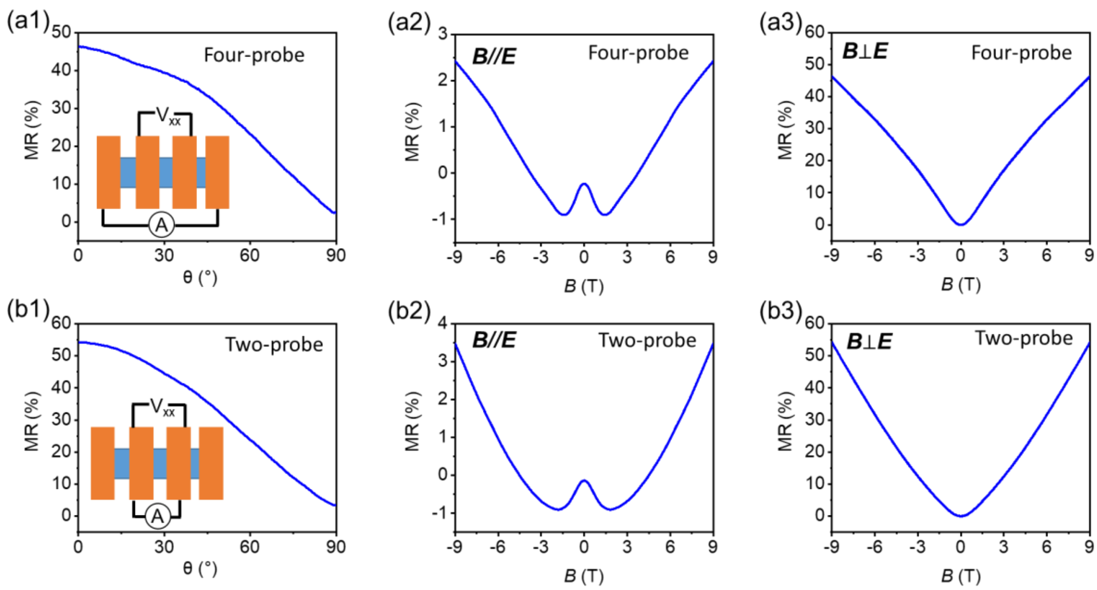

Figure 3.9 Exclusion of the current effect on the observed negative MR behaviours.

(a1, b1) Angle-dependent MR, (a2, b2) MR under *B//E*, and (a3, b3) MR under $B \perp E$ in the four-probe test and two-probe magnetotransport tests, respectively.

Another important signature of Weyl physics is the planar Hall effect, which exhibits angle-dependent in-plane transverse voltage. We study the planar Hall effect under different rotation angles to further corroborate the observed chiral anomaly (**Figure 3.10a**). The planar Hall resistance (R_{xy}) (**Figure 3.10b**) and in-plane resistance (R_{xx}) displays a periodic angular dependence of 180°. R_{xy} reaches its maximum and minimum value at ~135° and ~45°, respectively. Meanwhile, the maximum and minimum values of R_{xx} are at 90° and 0°, respectively. The values of tested R_{xy} and R_{xx} fit well with the equation of the planar Hall effect (**Figure 3.10b, c)**. These observations are typical characteristics of the chiral anomaly in Weyl physics[10]. The experimental results about the angle-dependent negative MR and planar Hall effect unambiguously verify the existence of chiral anomaly current in prepared Te samples.

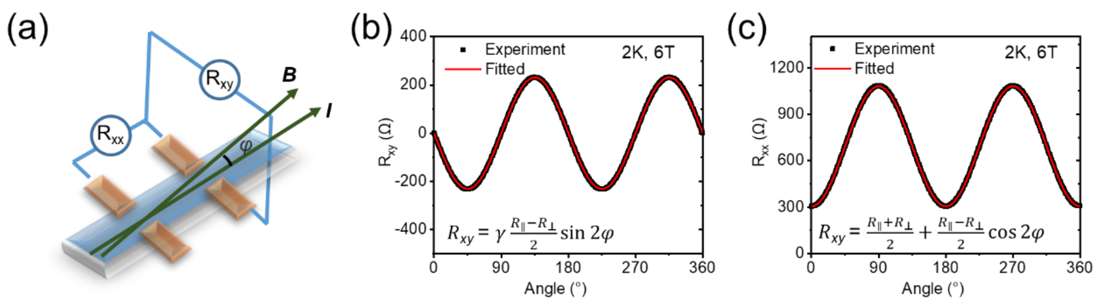

Figure 3.10 Planar Hall effect of Te device to further corroborate the observed chiral anomaly. (a) Schematic of test structure of planar Hall tests. *B*, *E* and the sample are in the same plane. $\boldsymbol{\varphi}$ is the angle between *B* and *E* (b) Angular dependence of the R_{xy}. Experiment data are well fitted by $\boldsymbol{\gamma \frac{R_{\parallel}-R_{\perp}}{2} \sin 2\varphi}$, where $\boldsymbol{\gamma}$ is the ratio of the

width to the length of the prepared Te device, $\boldsymbol{R}_{\parallel}$ is longitudinal MR under $\boldsymbol{B} \parallel \boldsymbol{E}$, and $\boldsymbol{R}_{\perp}$ is longitudinal MR under $\boldsymbol{B} \perp \boldsymbol{E}$. (c) Angular dependence of the R_{xx}. Experiment data are well fitted by $\frac{\boldsymbol{R}_{\parallel}+\boldsymbol{R}_{\perp}}{2}+\frac{\boldsymbol{R}_{\parallel}-\boldsymbol{R}_{\perp}}{2}\cos 2\boldsymbol{\varphi}$. These tests were carried out at 2 K under 6T.

The chiral anomaly is closely related to the carrier density and the $\boldsymbol{E}_F$ in the Weyl semiconductor Te. We prepared the Hall bar structures with different Te thicknesses, including the sample with ~32 nm (**Figure 3.11a)** and ~12 nm (**Figure 3.11b)**. Both samples show hole carrier transport according to Hall measurement (**Figure 3.11a, b**) and positive MR under $\boldsymbol{B}\perp\boldsymbol{E}$ (**Figure 3.11c**). The carrier density of the 32-nm-thick sample is 3.39×10^{13} cm^{-2} at 2 K, approximately 1 order of magnitude higher than that of the 12-nm-thick sample (2.25×10^{12} cm^{-2}).

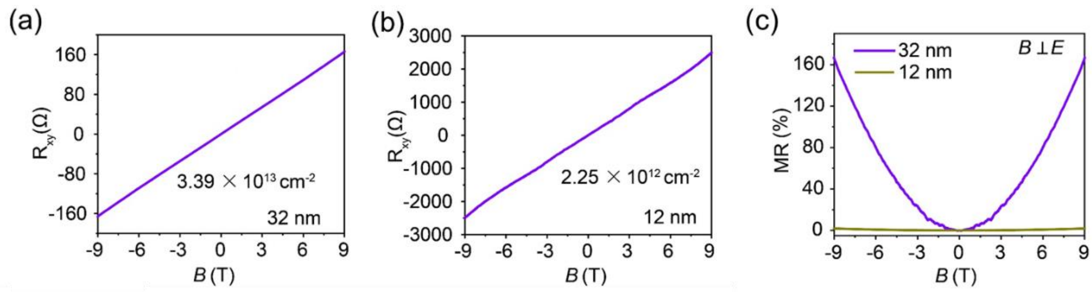

Figure 3.11 (a, b) Hall resistance and (c) MR of thick and thin samples under $\boldsymbol{B} \perp \boldsymbol{E}$.

We can observe negative MR in a 32-nm-thick sample under $\boldsymbol{B}//\boldsymbol{E}$ when the temperature decreases from 200 K to 100 K (**Figure 3.12a**). As the temperature further decreases from 100 K to 2 K, the negative MR becomes stronger from -2.7% to -48.9%. Thermal fluctuation influences the transport lifetime and related momentum relaxation of imbalanced chirality, resulting in the temperature-dependent MR behaviours[24]. In contrast, the 12-nm-thick sample exhibits only positive MR across different temperature range (**Figure 3.12b**) because of its low carrier density. **Figure 3.12c** shows the MR as a function of carrier densities in 10 samples under **B//E**. The samples with high carrier density exhibit strong negative MR (*e.g.*, 8.12 $\times 10^{13}$ cm^{-2} for -65.3% MR) because high hole density results in the downshift of E_F close to the Weyl point and generates high chiral anomaly current. For the sample with medium carrier density of 9×10^{12} cm^{-2}, it exhibits relatively weak negative MR (-1.15%). The samples with low carrier density (1.05×10^{12} cm^{-2}) give rise to the positive MR (1.33%). The E_F is in the band gap and away from the Weyl point, providing negligible chiral anomaly current.

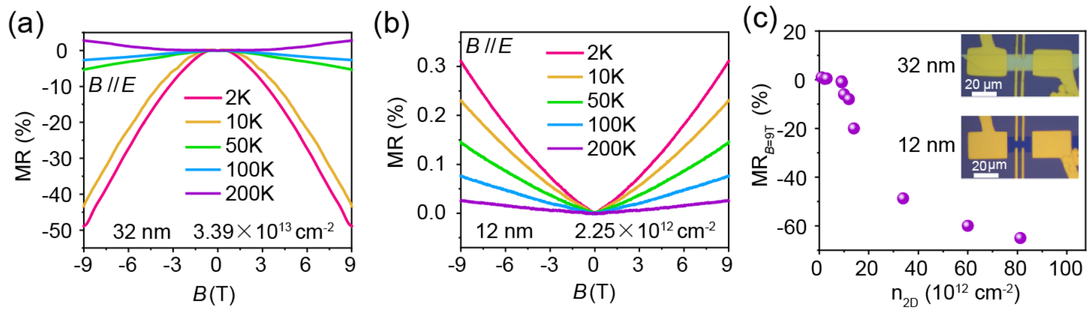

Figure 3.12 Carrier-density-dependent MR. (a) The temperature-dependent MR of 32-nm-thick sample under *B*//*E*. The hole carrier density is 3.39×10^{13} cm^{-2} at 2K. (b) The temperature-dependent MR of 12-nm-thick sample under *B*//*E*. The hole carrier density is 2.25×10^{12} cm^{-2} at 2K. (c) Carrier-density-dependent MR in different samples. The insets are the corresponding optical images of the prepared Hall bar structures based on 32-nm-thick and 12-nm-thick samples.

Figure 3.13 shows the prototypical TPCTs, where the Weyl semiconductor Te provides the transistor channel for low-dissipation chiral anomaly current in a Hal bar configuration. Chiral anomaly current (marked as red arrow in **Figure 3.13**) transports longitudinally along terminal 1-4. We detect the voltage through terminal 2 and 3 for extracting conductivity. The distance between terminal 2 and 3 is ~4 μm. To allow efficient modulation of chiral anomaly current in TPCTs, we adopt ionic liquid DEME-TFSI for electrostatic modulation because it can induce the carrier density more than 10^{14} cm^{-2}.

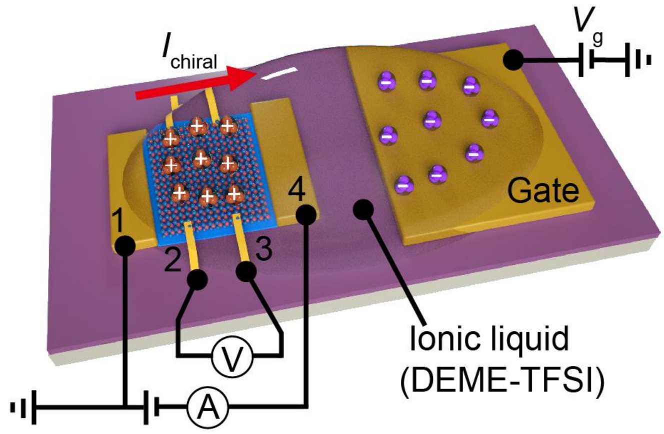

Figure 3.13 Schematic of topological transistors with Weyl semiconductor Te. Te flake and the side gate electrode are covered with ionic liquid (DEME-TSFI). Gating voltage can drive ions onto the channel surface of Te.

We characterize the samples with different thicknesses by electrical gating (**Figure 3.14**). For the thick sample (32 nm), as the V_g increases from 0 to +2 V, the negative MR disappears quickly and the positive MR of 2.49% appears at V_g= +2 V, because of weak Berry curvature and insignificant contribution of chiral anomaly current. We can observe negative MR -55.9% at V_g= -2 V, slightly larger than the negative MR at V_g= 0 due to the downshift of E_F and stronger Berry curvature. For the thin sample (12 nm), we observe negative MR more than -90% under V_g= -2 V. The negative MR of this TPCT is much higher than that reported in Dirac/Weyl semimetals[25,26], as a result of relatively weak background and ease of tuning the $\boldsymbol{E}_{\mathrm{F}}$ in the Weyl semiconductor. These results clearly suggests that the dominant current in TPCT is chiral anomaly current, where the charge current contributes insignificant part. **Figure 3.14c** shows the MR as a function of $\boldsymbol{V_g}$, in which the gating voltage can efficiently modulate the chiral anomaly current, especially in thin sample with low background carrier density.

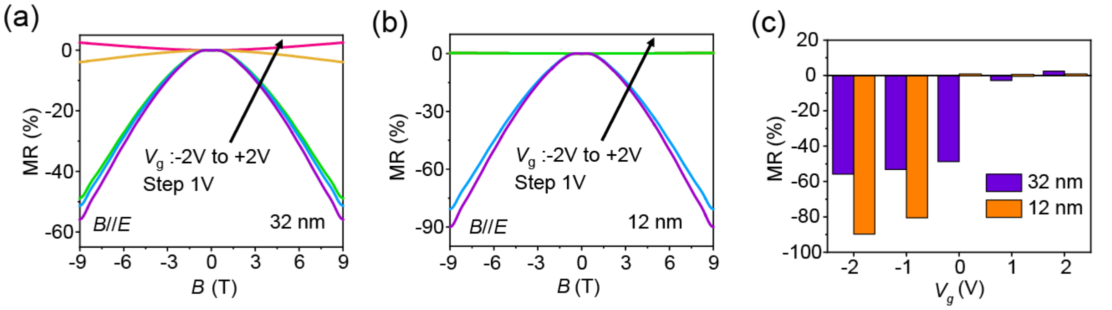

Figure 3.14 Magnetotransport tests of 32-nm-thick and 12-nm-thick samples under *B*//*E* at different gating voltages, respectively.

We can extract chiral anomaly conductivity ($\Delta\sigma$) by subtracting the background conductivity according to $\Delta\sigma = \sigma - \sigma_0$, where σ is the conductivity under specific magnetic field, and σ_0 is the conductivity without magnetic field. The Δσ -$\boldsymbol{B}^2$ curve (**Figure 3.15a, b**) is linear, showing strong dependence on $\boldsymbol{V}_{\mathbf{g}}$. This linear relationship between positive Δσ and $\boldsymbol{B}^2$ is consistent with the chiral anomaly relationship under relatively low magnetic field according to Equation (3.4)[25,27]:

$$\Delta\sigma = \frac{e^4 v_F^3 \tau B^2}{4\pi^2 \hbar \Delta\varepsilon^2} \tag{3.4}$$

where e is the electron charge, v_F is the Fermi velocity near the Weyl points, τ is the inter-valley scattering time, and $\hbar$ is the Planck constant.

The $\boldsymbol{E}_{\mathrm{F}}$ of TPCT with 32-nm-thick sample is close to the Weyl point, showing high conductivity at $\boldsymbol{V}_{\mathrm{g}}= 0$ and low conductivity at positive voltages (**Figure 3.15c**), which is typical depletion-mode FET characteristics. In contrast, the $\boldsymbol{E}_{\mathrm{F}}$ of 12-nm-thick sample locates in the band gap, which exhibits low conductivity "OFF" state at $\boldsymbol{V}_{\mathrm{g}}$= 0 and high conductivity "ON" state at negative gating voltages (**Figure 3.15d**), displaying the characteristic of enhancement-mode FET. In this thin sample, the OFF-state conductivity is 1.8×10^{-4} μS/μm while ON-state conductivity is 4.1×10^{4} μS/μm, consisting of a large amount of chiral anomaly conductivity ($\sigma_{\mathrm{chiral}}=3.7\times10^{4}$ μS/μm) and insignificant trivial charge conductivity ($\sigma_{\mathrm{trivial}}= 0.36\times10^{4}$ μS/μm).

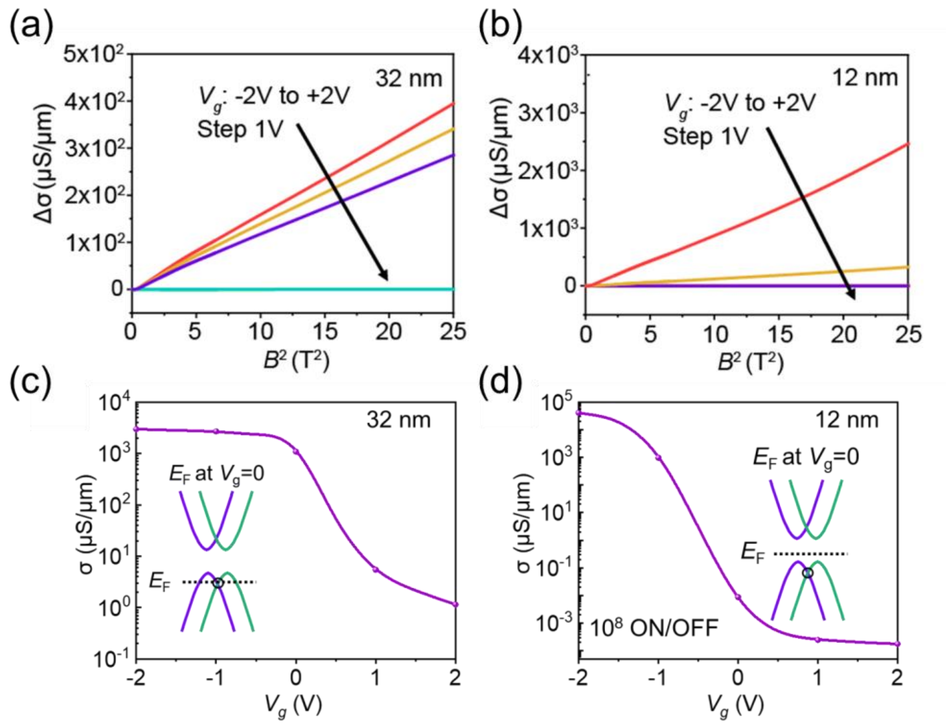

Figure 3.15 Electrical gating to manipulate the Δσ and σ. (a, b) $\Delta\sigma$ as a function of B^2 in 32-nm-thick and 12-nm-thick samples, analogue to the I_{d}-V_{d} curve of conventional charge-based FETs. The linear relationship between $\Delta\sigma$ and B^2 is in good agreement with the chiral anomaly equation under relatively low magnetic field. Different modes of topological FET with Weyl semiconductor Te. (c) Depletion-mode FET based on 32-nm-thick sample. E_{F} is close to the Weyl point at V_{g}= 0. (d) Enhancement-mode FET

based on 12–nm-thick sample. E_F is far away from the Weyl point at V_g= 0.

We also prepare the conventional back-gated Te FET (300-nm-thick SiO_2 as gate dielectrics) as a control sample of TPCT. When the gate voltage varies from negative to positive, the Te FET switches from the ON-state to the OFF-state, exhibiting typical p-type transport characteristics. The ON/OFF ratio is 2.1×10^4 with the ON-state conductivity of 443 μS/μm (**Figure 3.16**), which is comparable to other reported Te FET works[11,28] (*e.g.*, 10^4 ON/OFF and ~600 μS/μm ON-state conductivity[11]).

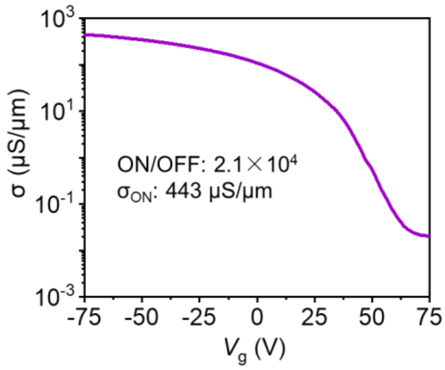

Figure 3.16 Transfer curve of prepared conventional charge-based Te FET at 300 K.

When the temperature decreases to 10 K, the $\boldsymbol{I_d}$-$\boldsymbol{V_d}$ curve of conventional Te FET exhibits linear shape (**Figure 3.17a**). The transfer curve (**Figure 3.17b**) shows the ON/OFF ratio of 2.0×10^5 and the ON-state conductivity of 660 μS/μm. We apply solid-state PEO/$LiClO_4$ electrolyte in TPCTs for more stable and large-scale applications. The Te TPCT (**Figure 3.17c**) exhibits nearly linear $\Delta\boldsymbol{\sigma}$-$\boldsymbol{B}^2$ curve under the magnetic field lower than 5T. The $\boldsymbol{\sigma}$-$\boldsymbol{V_g}$ curve of the Te TPCT shows that the ON/OFF ratio reaches 3.5×10^8 and the ON-state conductivity is up to 3.9×10^4 μS/μm (**Figure 3.17d**).

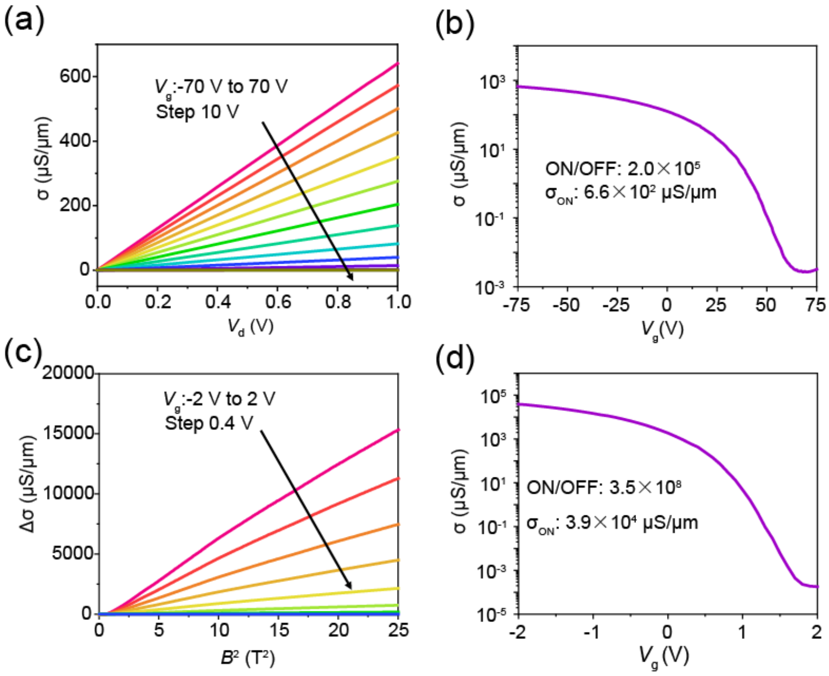

Figure 3.17 Performance comparison between conventional charge-based FETs and TPCTs. (a) Output curve in the Te charge-based FET as V_g increases from -70 V to 70 V. (b) Transfer curve in the Te charge-based FET, typical p-type FET with a ON/OFF ratio of 2.0×10^5 and ON-state conductivity of 660 μS/μm. (c) Chiral anomaly conductivity as a function of B^2 in the Te TPCT. (d) Transfer curve as a function of V_g in the Te TPCT with a ON/OFF ratio of 3.5×10^8 and ON-state conductivity of 3.9×10^4 μS/μm.

Different from charge transport in conventional FETs, the TPCTs can switch between Weyl semiconductor (chiral anomaly transport, ON-state) and conventional one (charge transport, OFF-state), which results in the coexistence of high ON/OFF ratio and high ON-state conductivity by shifting the position of $\boldsymbol{E_F}$ through electrostatic modulation. The Te TPCTs outperform reported spin/valley FETs[4,29], topological insulator-based FETs[30-32] and Te charge-based FET[11,28] **(Table 3.1)** in terms of both ON-state conductivity and ON/OFF ratio, showing great potential for ultralow power electronics.

Table 3.1 ON/OFF ratio comparison among our work, reported spin/valley-based FETs and charge-based FETs.

FET works	ON/ OFF
Charge-based Te FET ***Nat. Electron*.** 1, *228–236, 2018*	~10^6
Charge-based Te FET ***Nat. Nanotechnol*.** 15, *53–58, 2020*	~10^5
Valley-based FET ***Nat. Nanotechnol*.** *15, 743-749, 2020*	10^2 to 10^3
Spin-based FET ***Nat. Electron.*** 2, 159–163, 2019	400%
This work	**~10^8**

Figure 3.18a presents the relationship between ON/OFF ratio and ON-state conductivity of Te TPCTs with 300 nm channel length. The ON/OFF ratio and ON-state conductivity of Te TPCTs range from 1.6×10^8 to 4.0×10^8 and 3.8×10^4 μS/μm to 6.0×10^4 μS/μm, respectively. Different from Te charge-based FETs[11], the ON/OFF ratio of TPCTs is independent on their ON-state conductivity, exhibiting excellent performance compared with reported charge-based FETs with low-dimensional materials and state-

of-the-art Si transistors[11,33-39](**Figure 3.18b**). The coexistence of high ON-state conductivity and high ON/OFF ratio in TPCTs results from the topological phase change between conventional charge transport and low-dissipation chiral anomaly current. Compared with conventional charge-based FETs, the ON-state conductivity in TPCT is dominated by low-dissipation chiral anomaly current, which is determined by the strength of Berry curvature.

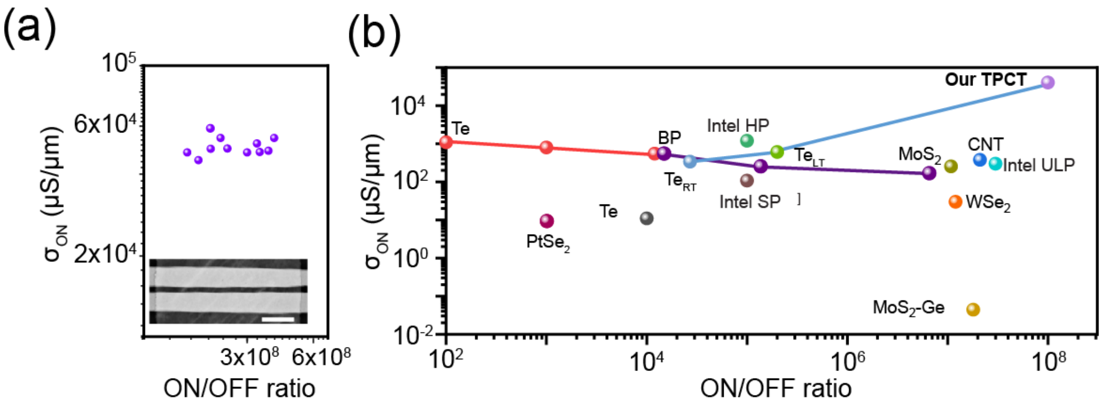

Figure 3.18 Performance comparison. (a) Summarized performance in prepared short-channel TPCTs. Inset is the SEM image of a typical device with ~300 nm channel length. The scale bar is 2 μm. (b) ON-state conductivity versus ON/OFF ratio in our work, the FETs based on low-dimensional materials and state-of-the-art Si transistors. Te_{RT} and Te_{LT} are the performance in Te charge-based FET at 300K and 10K, respectively. Three kinds of Intel 14-nm transistor: HP (high performance), SP (standard performance), and ULP (ultralow-power).

The off-conductivity in our topological field-effect transistor is 1.8×10^{-4} μS/μm, which is lower than recent low-dimensional based high-impact transistor works. Te charged-based transistors show the off-conductivity of ~10^{-3} μS/μm[11,28]. For carbon nanotube, the off-conductivity is ~3×10^{-4} μS/μm[40]. The off-conductivity of black phosphorus-based transistor shows ~4×10^{-3} μS/μm[41].

The working temperature in our topological field-effect transistor is 10K, which is much higher than recent non-charge-based electronics (including topological transistors). Emerging electronics always suffer from harsh conditions. A well-known example is the quantum computing device: in the IBM Quantum lab, they must keep the temperature extremely cold (15 mK) to achieve high performance. Besides quantum computing, Josephson junction-based infrared detectors can only work during 27 mK to 325 mK[42]. The working temperature of the graphene-based microwave detectors is 0.19 K[43]. The supercurrent field-effect transistor works at about 0.41 K[44].

The output conductance of TPCTs is dependent on the gating voltage, magnetic field and the relative angle between magnetic and electrical field[25], which allows processing multiple input signals. By designing V_g and $\boldsymbol{B}$ as input signals and $\Delta\sigma$ as the output signal, we can realize "AND" and "OR" logic functions based on Te TPCTs (**Figure 3.19**). Furthermore, we can switch "AND" and "OR" logic functions in a single TPCT by changing the angle between magnetic and electrical fields. We firstly demonstrated the multiple-input logic functions. For the input$_1$ (V_g), logic "0" and "1" are defined as $-2V \le V_g < 0$ and $0 \le V_g \le 2V$, respectively. For the input$_2$ ($\boldsymbol{B}$), logic "0" and "1" are defined as -8 T$\le \boldsymbol{B} <$-4 T and -4 T$\le \mathbf{B} \le$ 0, respectively. The output "0" corresponds to MR< -14%, and "1" corresponds to MR ≥ -14%. When input$_1$ or input$_2$ is logic "1", the output is "1" (**Figure 3.19a**), exhibiting OR logic function. We define θ as input$_1$ with 0° as "0" and 10° as "1". V_g is defined as input$_2$ with V_g= 0 as "0", and V_g= -2 V as logic "1". Input$_3$ is $\boldsymbol{B}$ with 1 T as logic "0", and 2 T as logic "1". The output is defined as “0” corresponding to |MR|< 1%, and “1” for |MR|≥ 1%. Then, we can achieve the AND-OR logic function with three input signals (**Figure 3.19b**).

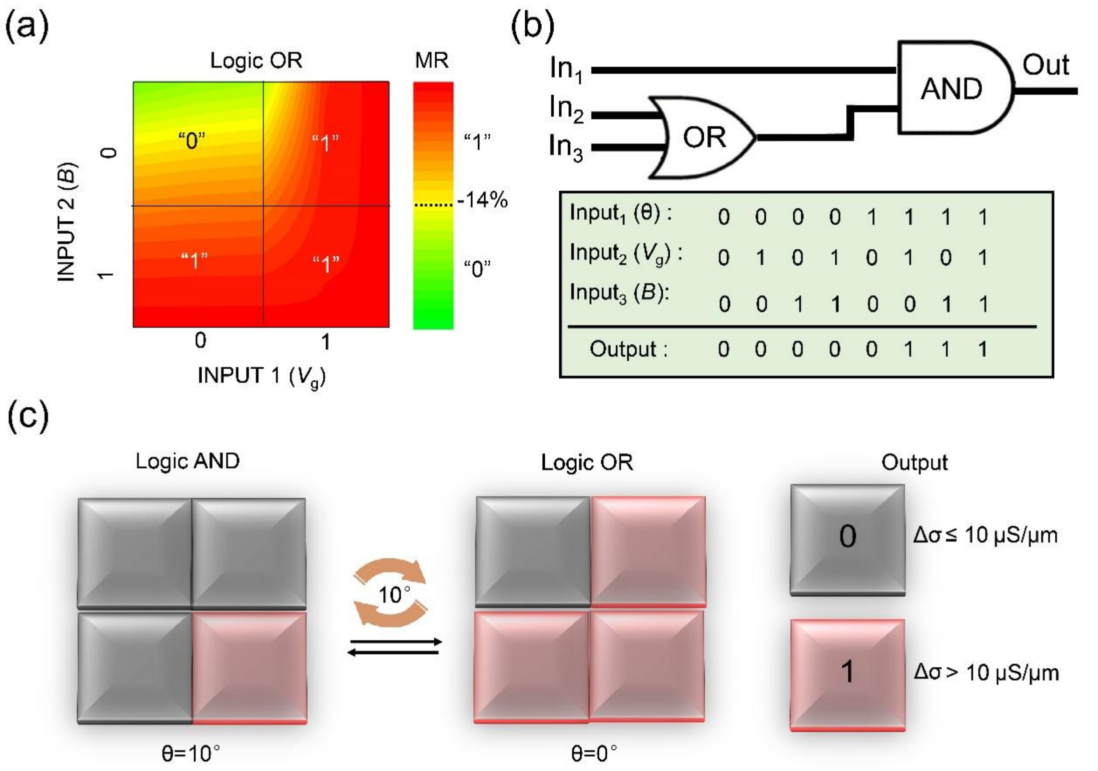

$Input_1$ (θ) :	0	0	0	0	1	1	1	1
$Input_2$ (V_g) :	0	1	0	1	0	1	0	1
$Input_3$ (B):	0	0	1	1	0	0	1	1
Output :	0	0	0	0	0	1	1	1

Figure 3.19 Multiple-mode logic functions based on the topological Te FETs. (a) Two-input AND logic function. (b) Three-input OR-AND logic function. (c) Demonstration of a single topological Te FET for angle-switching logic functions (OR, AND).

The logic functions (OR, AND) can be switched in one TPCT (left panel of **Figure 3.19c**) by changing the angle. $Input_1$ is defined as “0” for V_g= 0 and “1” for V_g=-1 V. $Input_2$ is “0” for $\boldsymbol{B}$=1 T and “1” for $\boldsymbol{B}$= 2 T. When Δσ < 10 μS/μm, the output is “0”; otherwise, the output is “1”. For the thick sample under **B//E** (θ= 0), when either one of the $input_1$ and $input_2$ is “1”, the output is “1”, corresponding to OR logic. After switching the angle by 10° (θ= 10°), this device shows AND logic because when both $input_1$ and $input_2$ is “1”, the output is “1”. So, this “angle-switching” strategy can efficiently change the logic functions from OR to AND due to the high sensitivity of chiral anomaly current to the rotation angle.

3.4 Summary

We investigate the magneto-transport of Weyl semiconductor Te and verify the presence of chiral anomaly current. We design and demonstrate the TPCTs that can retain a highly conductive and low-dissipation ON state and switch to a trivial phase OFF state with high resistance. The use of Weyl semiconductor eliminates the high background current in Weyl semimetal and allows to efficiently change its topological phase. The Te TPCTs exhibit a high ON/OFF ratio of 10^8 and high ON-state conductivity (3.9×10^4 μS/μm), which show much better performance than conventional charge-based FETs and emerging spin/valley FETs. Furthermore, we demonstrate multiple-input logic functions in one TPCT. Our proposed Te TPCT provides an ultralow-power device alternative to conventional charge-based FETs.

3.5 References

1 Akinwande, D. *et al.* Graphene and two-dimensional materials for silicon technology. *Nature* **573**, 507-518 (2019).

2 Shukla, N. *et al.* A steep-slope transistor based on abrupt electronic phase transition. *Nature Communications* **6**, 7812 (2015).

3 Mak, K. F., Xiao, D. & Shan, J. Light–valley interactions in 2D semiconductors. *Nature Photonics* **12**, 451-460 (2018).

4 Li, L. *et al.* Room-temperature valleytronic transistor. *Nature Nanotechnology* **15**, 743-749 (2020).

5 Lin, X., Yang, W., Wang, K. L. & Zhao, W. Two-dimensional spintronics for low-power electronics. *Nature Electronics* **2**, 274-283 (2019).

6 Datta, S. How we proposed the spin transistor. *Nature Electronics* **1**, 604-604 (2018).

7 Kharzeev, D. E. The chiral magnetic effect and anomaly-induced transport. *Progress in Particle and Nuclear Physics* **75**, 133-151 (2014).

8 Jia, S., Xu, S.-Y. & Hasan, M. Z. Weyl semimetals, Fermi arcs and chiral anomalies. *Nature Materials* **15**, 1140-1144 (2016).

9 Zhang, N. *et al.* Magnetotransport signatures of Weyl physics and discrete scale invariance in the elemental semiconductor tellurium. *Proceedings of the National Academy of Sciences* **117**, 11337-11343 (2020).

10 Qiu, G. *et al.* Quantum Hall effect of Weyl fermions in n-type semiconducting tellurene. *Nature Nanotechnology* **15**, 585-591 (2020).

11 Wang, Y. *et al.* Field-effect transistors made from solution-grown two-dimensional tellurene. *Nature Electronics* **1**, 228-236 (2018).

12 Yao, Y. *et al.* First principles calculation of anomalous Hall conductivity in ferromagnetic bcc Fe. *Physical review letters* **92**, 037204 (2004).

13 Thouless, D. J., Kohmoto, M., Nightingale, M. P. & den Nijs, M. Quantized Hall conductance in a two-dimensional periodic potential. *Physical review letters* **49**, 405 (1982).

14 Giannozzi, P. *et al.* QUANTUM ESPRESSO: a modular and open-source software project for quantum simulations of materials. *Journal of physics: Condensed matter* **21**, 395502 (2009).

15 Giannozzi, P. *et al.* Advanced capabilities for materials modelling with Quantum ESPRESSO. *Journal of Physics: Condensed Matter* **29**, 465901 (2017).

16 Giannozzi, P. *et al.* Quantum ESPRESSO toward the exascale. *The Journal of Chemical Physics* **152**, 154105 (2020).

17 Mostofi, A. A. *et al.* An updated version of wannier90: A tool for obtaining maximally-localised Wannier functions. *Computer Physics Communications* **185**, 2309-2310 (2014).

18 Kresse, G. & Furthmüller, J. Efficiency of ab-initio total energy calculations for metals and semiconductors using a plane-wave basis set. *Computational materials science* **6**, 15-50 (1996).

19 Perdew, J. P., Burke, K. & Ernzerhof, M. Generalized gradient approximation made simple. *Physical review letters* **77**, 3865 (1996).

20 Blöchl, P. E. Projector augmented-wave method. *Physical review B* **50**, 17953 (1994).

21 Zhang, C.-L. *et al.* Signatures of the Adler–Bell–Jackiw chiral anomaly in a Weyl fermion semimetal. *Nature Communications* **7**, 10735 (2016).

22 Qiao, J. *et al.* Few-layer Tellurium: one-dimensional-like layered elementary semiconductor with striking physical properties. *Science bulletin* **63**, 159-168 (2018).

23 Zhang, X. *et al.* Hydrogen-assisted growth of ultrathin Te flakes with giant gate-dependent photoresponse. *Advanced Functional Materials* **29**, 1906585 (2019).

24 Zhang, C. *et al.* Room-temperature chiral charge pumping in Dirac semimetals. *Nature Communications* **8**, 13741 (2017).

25 Wang, Y. *et al.* Gate-tunable negative longitudinal magnetoresistance in the predicted type-II Weyl semimetal WTe_2. *Nature communications* **7**, 1-6 (2016).

26 Li, H. *et al.* Negative magnetoresistance in Dirac semimetal Cd_3As_2. *Nature Communications* **7**, 10301 (2016).

27 Fukushima, K., Kharzeev, D. E. & Warringa, H. J. Chiral magnetic effect. *Physical Review D* **78**, 074033 (2008).

28 Zhao, C. *et al.* Evaporated tellurium thin films for p-type field-effect transistors and circuits. *Nature nanotechnology* **15**, 53-58 (2020).

29 Jiang, S., Li, L., Wang, Z., Shan, J. & Mak, K. F. Spin tunnel field-effect transistors based on two-dimensional van der Waals heterostructures. *Nature Electronics* **2**, 159-163 (2019).

30 Vandenberghe, W. G. & Fischetti, M. V. in *2014 IEEE International Electron Devices Meeting.* 33.34. 31-33.34. 34 (IEEE).

31 Di Bernardo, I. *et al.* Progress in epitaxial thin-film Na_3Bi as a topological electronic material. *Adv Mater* **33**, 2005897 (2021).

32 Collins, J. L. *et al.* Electric-field-tuned topological phase transition in ultrathin Na_3Bi. *Nature* **564**, 390-394 (2018).

33 Sarkar, D. *et al.* A subthermionic tunnel field-effect transistor with an atomically thin channel. *Nature* **526**, 91-95 (2015).

34 Natarajan, S. *et al.* in *2014 IEEE International Electron Devices Meeting.* 3.7. 1-3.7. 3 (IEEE).

35 He, D. *et al.* High-performance black phosphorus field-effect transistors with long-term air stability. *Nano letters* **19**, 331-337 (2018).

36 Zhao, Y. D. *et al.* High-Electron- Mobility and Air-Stable 2D Layered $PtSe_2$ FETs. *Advanced Materials* **29**, 1604230 (2017).

37 Wang, J. *et al.* in *2018 IEEE International Electron Devices Meeting (IEDM).* 22.23. 21-22.23. 24 (IEEE).

38 Qiu, C. *et al.* Dirac-source field-effect transistors as energy-efficient, high-performance electronic switches. *Science* **361**, 387-392 (2018).

39 Yu, Z. *et al.* in *2017 IEEE International Electron Devices Meeting (IEDM).* 23.26. 21-23.26. 24 (IEEE).

40 Liu, L. *et al.* Aligned, high-density semiconducting carbon nanotube arrays for high-performance electronics. *Science* **368**, 850-856 (2020).

41 Wu, Z. *et al.* Large-scale growth of few-layer two-dimensional black phosphorus. *Nature Materials* (2021).

42 Walsh, E. D. *et al.* Josephson junction infrared single-photon detector. *Science* **372**, 409-412 (2021).

43 Lee, G.-H. *et al.* Graphene-based Josephson junction microwave bolometer. *Nature* **586**, 42-46 (2020).

44 De Simoni, G., Paolucci, F., Solinas, P., Strambini, E. & Giazotto, F. Metallic supercurrent field-effect transistor. *Nature Nanotechnology* **13**, 802-805 (2018).

Chapter 4 Room-temperature valley transistors to process static and dynamic information

As a quantum degree of freedom, the valley exhibits low-dissipation transport characteristics for carrying information with high energy efficiency. However, it remains a grand challenge to operate the valley transistor at room temperature efficiently and realise essential computing functions. Here we demonstrate room-temperature valley transistors based on Weyl semiconductor (Te), showing the diffusion length of more than 7 μm because of the long relaxation time of valley current based on the chiral anomaly. Electrochemical modulation effectively change the Fermi level ($\boldsymbol{E}_{\mathrm{F}}$) and Berry curvature ($\mathbf{1}/\boldsymbol{E}_{\mathrm{F}}^{2}$ sensitivity). The electrical double layer capacitance can volatilely shift the E_{F} of Te and modulate the valley transistor with an ON/OFF ratio of 10^5. The coexistence of ion adsorption and intercalation mechanisms results in tunable nonlinearity and retention time, promising different neuromorphic computing applications. The accuracy of classifying static images and dynamic icons both reach 95%. Our studies show the potentials of low-power valley electronics to process static and dynamic information.

4.1 Introduction

The ever-increasing computation energy demands energy-efficient electronics. As conventional charge-based electronics are approaching fundamental limits, valley (a quantum degree of freedom) provides an information carrier with low-power features due to its low-dissipation transport characteristics[1-3]. The electrical field, magnetic field, and light can generate and manipulate the valley (±K) in specific materials (*e.g.*, MoS_2)[3-6]. For instance, circularly polarised light can confine electrons in MoS_2 to individual momentum valleys. However, it is still quite challenging to achieve the high ON/OFF ratio valley field-effect transistors (FETs) and essential computing functions at room temperature because of the short lifetime of the excitonic valley states[3].

To operate the valley devices at room temperature, the relaxation length of the valley must be sufficiently long that the gating process can efficiently modulate the transport[7]. Chiral-anomaly-based valley current (CAVC) transport can reach 10 to 100 μm due to large quasi-momentum transfer between valleys and long relaxation time[8]. The inter-valley transport compensates for the pumped chiral charges (**Figure 4.1**), which arises from chiral anomaly[9].

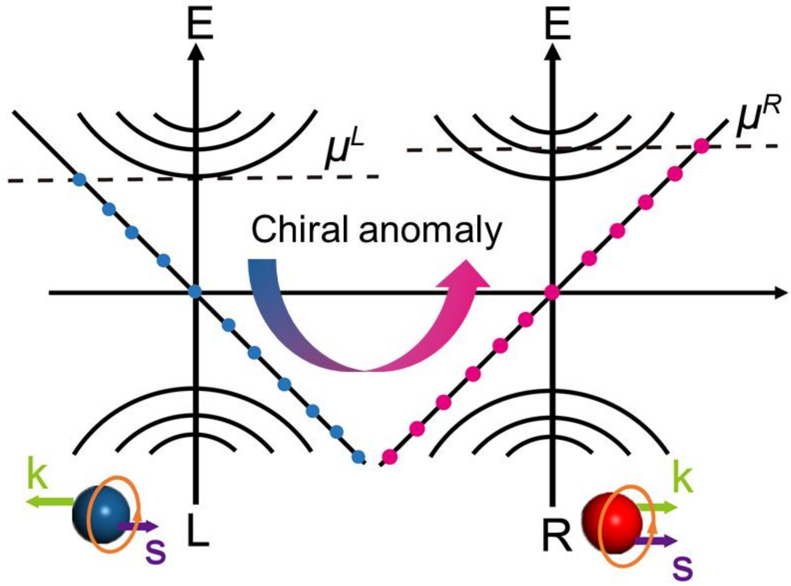

Figure 4.1 Chiral anomaly in Dirac/Weyl physics. Charge pumping refers that the

charge depleted at one Weyl node will be generated at the other node with opposite chirality. The charge pumping between Weyl nodes results in the low-dissipation chiral anomaly current ($\boldsymbol{J_c}$), which generates and transports in the form of $\boldsymbol{J_c} = \frac{e^2 B}{4\pi^2\hbar^2 c}(\mu^{R} - \mu^{L})$. $\boldsymbol{J_c}$ is topologically protected and "even" under time reversal.

The CAVC exhibits width- and length-dependent transport characteristics at room temperature[10] but the manipulation of CAVC is limited by the hard manipulation of EF in the topological semimetal in the reported work. Recently, Weyl semiconductors are reported with a band structure distinctly different from the Weyl semimetals[11,12] (**Figure 4.2**).

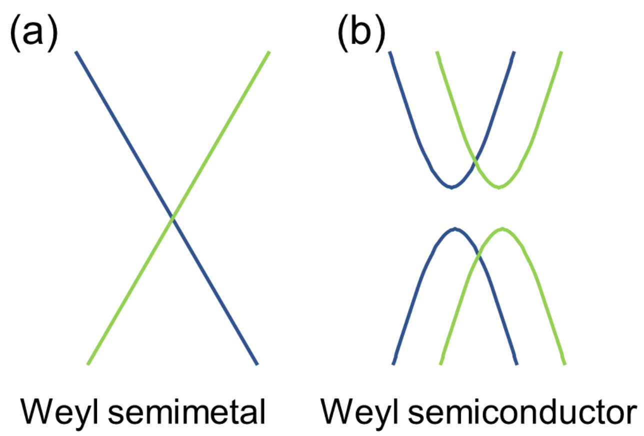

Figure 4.2 Typical scheme of the band structure for the topological semimetal and the topological semiconductor.

The unique band structure of the Weyl semiconductor enables the detection of CACS with low background conductance compared with the topological semimetals (**Table 4.1**).

Table 4.1 Comparison of the topological semimetal and semiconductor for chiral anomaly-based electronics.

	Topological semimetal	Topological semiconductor
Density of states around Weyl point	Strong	Weak
Background influence	Strong	Weak
Tunability of Fermi level and chiral anomaly	Hard	Easy

We can detect CAVC in an "H" structure (**Figure 4.3**, the red arrow illustrates the transport direction of CAVC). When the magnetic field is in parallel with constant current through electrodes 1 and 2, valley imbalance generates from the chiral anomaly. The nonlocal structure allows us to detect the valley current through electrodes 3 and 4. The CAVC is determined by the strength of Berry curvature, which is sensitive to the position of Fermi level ($\boldsymbol{E}_{\mathbf{F}}$)[8]. We can efficiently modulate the valley transport at room temperature through electrochemical modulation through volatilely shifting $\boldsymbol{E}_{\mathbf{F}}$ by electrical double layer capacitance[13] and non-volatilely shifting $\boldsymbol{E}_{\mathbf{F}}$ by the ion intercalation/extraction[14,15], respectively.

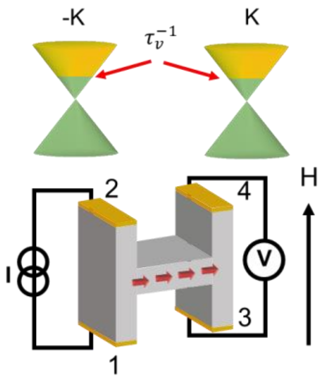

Figure 4.3 Detection of inter-valley transport based on the chiral anomaly. Valley

pseudospin (indicated by node position ±K) imbalance relaxes at a rate of $\boldsymbol{\tau_v^{-1}}$. For practical tests, planar and nonlocal electrodes are prepared in the etched samples for detecting the valley.

In this work, we demonstrate room-temperature valley FETs based on Weyl semiconductor Te. We achieve the valley FET with the ON/OFF ratio of about 10^5 at room temperature by electrostatic gating. The coexistence of ion adsorption and intercalation mechanisms result in the output curves with tunable low/high nonlinearity and long/short-term memory (3000 s vs 10 ms). The accuracy of classifying static images with the artificial neural network, and processing dynamic icons with reservoir computing both reach 95%. Our studies provide the potentials of low-power computing applications by valley degree of freedom at room temperature.

4.2 Experimental section

Device fabrication

We prepared Te flakes by hydrothermal methods[16] and transferred them to the Si substrate with 300-nm-thick SiO_2. Electron beam lithography was used to define the pattern of metal electrodes in a Hall bar configuration with a side gate. Metal contacts were prepared by thermal evaporation of Au (80 nm) at the rate of 0.3 Å /s under the vacuum of 3×10^{-7} Torr. The Te flake was etched by the focused ion beam to achieve the "H" configuration for the nonlocal valley transport measurement [10]. A low beam current of 10 pA, 20 kV was adopted in the etching process to avoid severe damage to the sample.

Device characterisation

The electrical measurements were carried out by Physical Property Measurement System from Quantum Design and Keithley 4200. For the valley FET, a droplet of ionic liquid DEME-TSFI is used to cover the Te flake and the side gate electrode. Before the test, the device was kept under a high vacuum with 4×10^{-8} Torr for 24 h to remove the water. For valley synapses, PEO/$LiClO_4$ electrolyte (PEO and $LiClO_4$ in methanol with a mass ratio of 9: 1) was coated on the sample, and then the sample was heated at 70 °C for 30 minutes to remove the solvent.

Materials characterisations

Scanning electron microscopic images were acquired by JEOL Model JSM-6490. XPS spectra were tested by Thermo Fisher Nexsa. For the gated Te, samples were carefully washed with water and methanol to remove PEO/$LiClO_4$ before the XPS characterisation.

First-principles calculations

The band structure and density of states calculations were carried out using DFT implemented in the Vienna Ab initio Simulation Package (VASP)[17]. The Perdew-Burke-Ernzerhof-type generalised gradient approximation[18] and the projector augmented-wave (PAW) method were employed[19]. A plane-wave basis set with a default energy cutoff and the 16 × 16 × 12 k-point mesh was used. A 3×3×3 Te supercell was used to calculate the density of states with or without Te vacancies. After removing one Te atom (marked by the red circle) from the supercell, the vacancy density in the calculated deficient Te sample is 1/81 (~1.23%). The Li doping concentration in defective is 1/81 (~1.23%) and 1/41 (~2.46%) in defective Te.

Neuromorphic computing simulations

For ANN, a three-layer artificial neural network was used to execute supervised learning over the training examples, after which the network accuracy was compared against the test examples in a single training epoch. MNIST dataset, a large image version (28 × 28 pixels) of the handwritten digit, is used for training and classifying.

For RC, our devices are used for the reservoir neurons, which can nonlinearly deal with the inputs. The connecting weights between the reservoir nodes and the output nodes are trained. There are 25×20 input neurons, 5×20 reservoir neurons and 5 output neurons in this computing system.

4.3 Results and discussion

As a narrow-gap semiconductor (~0.31 eV), Te exhibits strong spin-orbit coupling and no inversion symmetry (**Figure 4.4a)**, which results in the splitting spin up/down bands. Along the L-H path of the Brillouin zone (**Figure 4.4b)**, there is a pair of Weyl points with opposite chirality (W_1 and W_2), which arises from the crossing of two spin-splitting valence bands (**Figure 4.4c**).

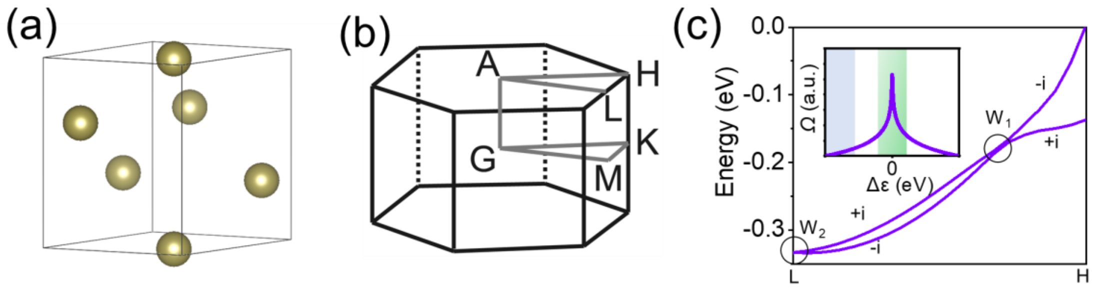

Figure 4.4 Crystal structure, Brillion zone and bandstructure of Te.

It is reasonable to shift the position of $\boldsymbol{E}_F$ close to W_1 by electrostatic modulation because W_1 is only ~0.2 eV below the $\boldsymbol{E}_F$. The inset curve of **Figure 4.4c** shows a typical distribution of the Berry curvature as a function of the energy separation ($\Delta\varepsilon$) between $\boldsymbol{E}_F$ and the Weyl point. When the $\boldsymbol{E}_F$ shifts close to the W_1, it exhibits the strongest Berry curvature and valley strength. By moving $\boldsymbol{E}_F$ away from the W_1, the Berry curvature and valley strength decays rapidly. Therefore, we can manipulate the position of $\boldsymbol{E}_F$ of Weyl materials and switch of valley FET by electrostatic modulation.

The carrier density and the position of $\boldsymbol{E}_F$ of Te are very sensitive to the defects. The reported carrier density of as-grown Te is up to 8×10^{16} cm^{-3} with the $\boldsymbol{E}_F$ in the valence band due to Te vacancies[12]. To systematically investigate the effects of Te vacancies and Li intercalation on the shift of $\boldsymbol{E}_F$, we perform theoretical calculations about the band structures of perfect Te, defective Te, and Li-intercalated defective Te (**Figure 4.5**).

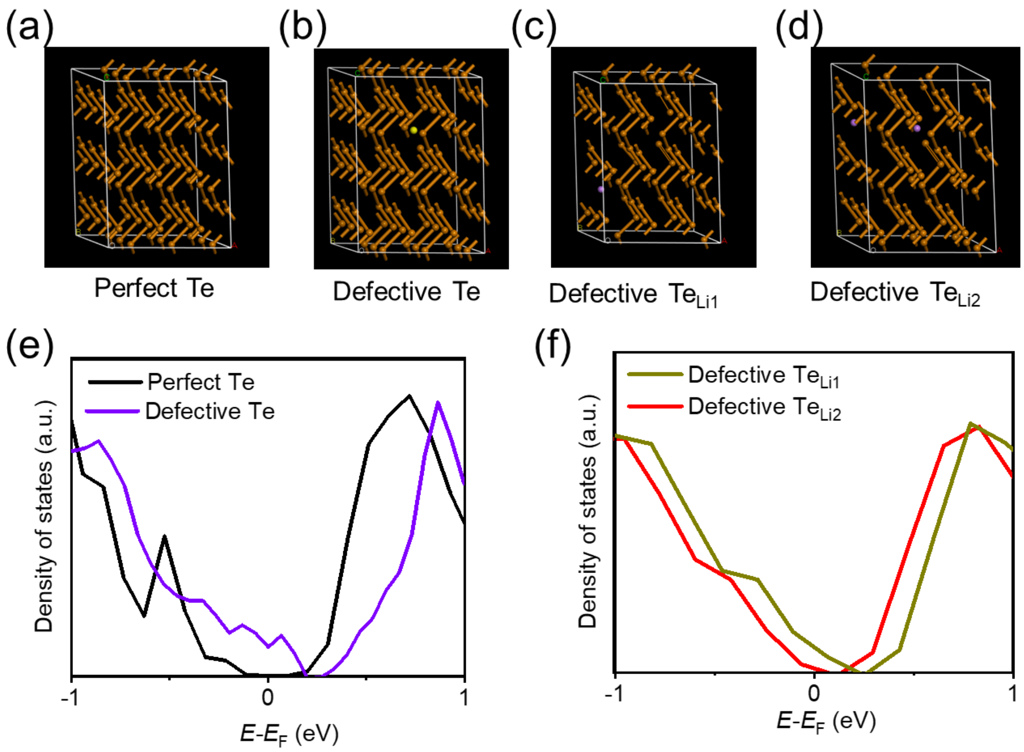

Figure 4.5 Calculation configuration and densities of states of different Te structures. (a-d) Configuration of perfect Te, defective Te (1.23% Te vacancy), defective Te_{Li1} (1.23% Te vacancy and 1.23% Li doping) and defective Te_{Li2} (1.23% Te vacancy and 2.46% Li doping). Te vacancy is marked yellow ball. Doping Li is marked purple ball. (e) Densities of states of perfect and defective Te. (f) Densities of states of defective Te with different concentrations of Li doping.

Figure 4.6 summarises the energy separation between $\boldsymbol{E}_F$ and W_1 ($\boldsymbol{E}_{W1}$), where $\Delta\varepsilon=\boldsymbol{E}_F-\boldsymbol{E}_{W1}$.For the Te with a perfect crystalline structure, the $\boldsymbol{E}_F$ is about 0.31 eV higher than W_1. It is hard to observe the valley current in this perfect Te because the Berry curvature strength is very weak due to the large $\Delta\varepsilon$. For the defective Te (1.23 % Te vacancy), the $\boldsymbol{E}_F$ is downshifting to the position of W_1 because Te vacancy acts as the electron acceptor[12]. The small energy separation ($\Delta\varepsilon\approx0$) gives rise to a very strong Berry curvature and CAVC. In Li-intercalated defective Te_{Li1} structure (1.23 % Te vacancy and 1.23% Li concentration), the $\Delta\varepsilon$ increases to 0.05 eV. Thus, Li intercalation is an effective method to non-volatilely shift the E_F and the valley current. With more Li intercalated into defective Te_{Li2} structure (2.46% Li concentration), $\Delta\varepsilon$ reaches 0.10 eV. These results reveal that Li intercalation in defective Te can increase the $\Delta\varepsilon$ step by step as the Li concentration increases. In this way, we can use controllable Li doping to achieve the non-volatile shift of E_F and the stable synaptic valley FETs.

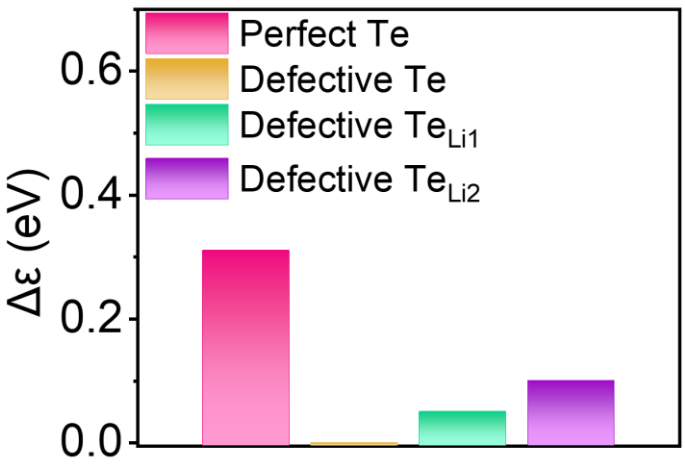

Figure 4.6 The summary of calculated energy separation between E_F and Weyl point W_1. There are perfect Te, defective Te (1.23% Te vacancy), defective Te_{Li1} (1.23% Te vacancy and 1.23% Li doping) and defective Te_{Li2} (1.23% Te vacancy and 2.46% Li doping).

We design valley FETs by patterning the Te flake into a Hall bar with a side gate electrode. With the ionic liquid electrolyte EDME-TFSI, we can achieve the equivalent double layer capacitance as high as ~10 mF/cm^2. Gating voltage can efficiently shift the E_F close to or away from the W_1. Thus, the valley FET can exhibit an output curve similar to conventional FETs (left panel in **Figure 4.7a**). With ion intercalation/extraction (*e.g.*, Li^+ from the solid-state electrolyte PEO/$LiClO_4$), it can non-volatilely shift the position of $\boldsymbol{E}_F$. In this way, we can control multiple non-volatile states in synaptic valley FET according to the amplitude and duration of gate voltage and time (right panel in **Figure 4.7b**), similar to the synapses based on organic electrochemical ion FETs[14].

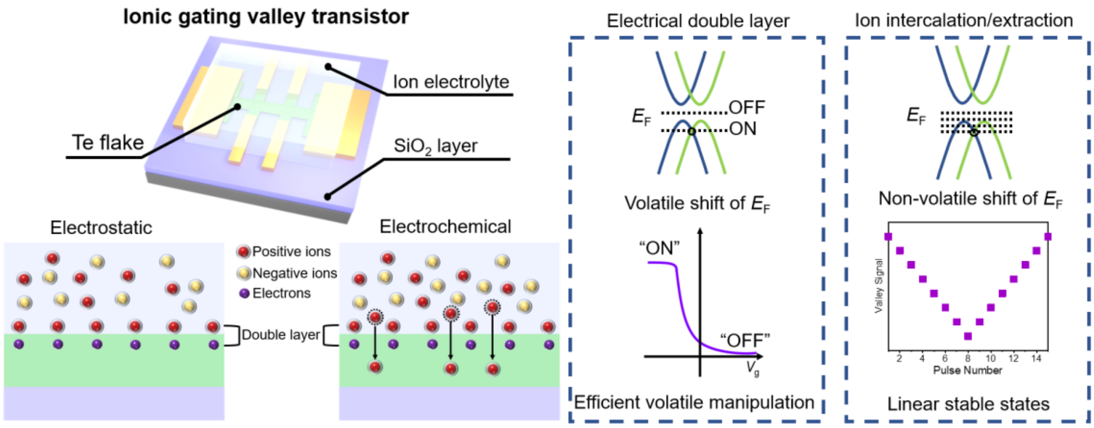

Figure 4.7 Valley transistors based on the ion manipulation. Electrical double layer of ions with a volatile shift of E_F in Te flakes for valley transistors. Reversible ion intercalation/extraction with a non-volatile shift of E_F in Te flakes for valley synapses.

We patterned Te flake with a Hall bar configuration. The Hall resistance shows the hole density of 4×10^{13} cm^{-2} at 300 K (**Figure 4.8**). The high hole density from Te vacancies can shift the position of $\boldsymbol{E}_F$ close to the Weyl point of Te, which allows us to observe the valley current without additional gating.

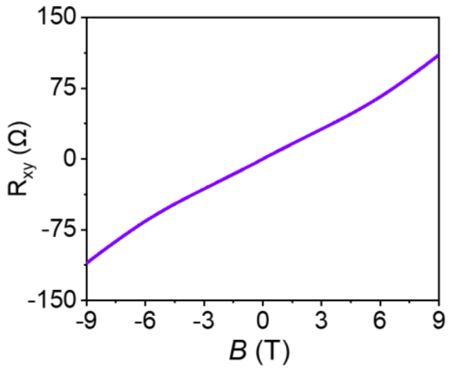

Figure 4.8 Self-doped high hole carrier density (n_{2D} =3.0×10^{13} cm^{-2}).

To detect the valley transport, we design and fabricate the device with an "H" configuration (**Figure 4.9a**) for detecting the nonlocal valley resistance (R_{VNL})[8,20]. We apply constant current through terminal 1-2 and detect nonlocal resistance (R_{NL}) with terminal 3-4, which is a mixed contribution from both the Ohmic nonlocal resistance (R_{ONL}) and R_{VNL}. We can extract R_{VNL} according to the Van der Pauw formula (details in Supplementary Note I). Since the nonlocal response from R_{VNL} vanishes at ***B***=0, we can extract R_{ONL} from R_{NL}. **Figure 4.9b** displays the temperature-dependent R_{VNL} from 300 K to 2 K, revealing that the valley current becomes weaker with the increase of temperature. It is noteworthy that strong valley current (R_{VNL}=-6.4 Ω under 9T) still exists at room temperature.

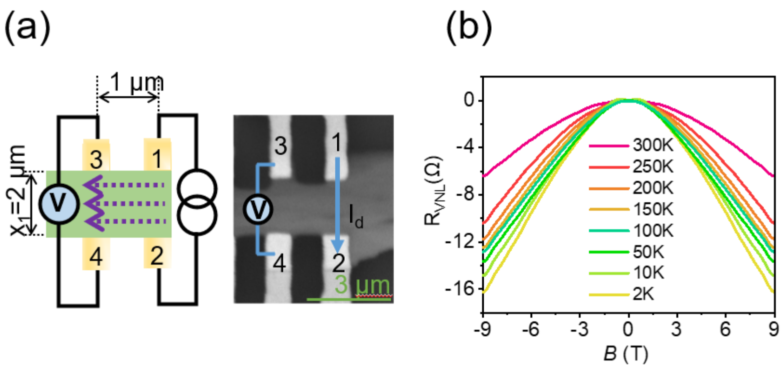

Figure 4.9 Temperature-dependent valley transport. (a) Schematic and scanning

electron microscopy image of the "H" geometry valley device. (b) Temperature-dependent valley transport from 300K to 2K.

For the CAVC, there are two typical transporting characteristics: length-dependent and width-dependent valley transport. **Figure 4.10a** shows the R_{VNL} as a function of the magnetic field, clearly exhibiting the length-dependent valley transport characteristics. We plotted the local resistance (R_L) of terminal 1-2 at B=0 as a function of channel length (**Figure 4.10b**), which shows an exponential decay. So Van der Pauw formula is suitable in our samples. The valley current is still sufficiently strong (R_{VNL}=-1.0 Ω under 9T) even with a long transport distance of 7 μm. **Figure 4.10c** shows extracted $|R_{VNL}|$ as a function of channel length in the semi-log curve. $|R_{VNL}|$ is well fitted by a linear line, in good consistency with the decay law of CAVC.

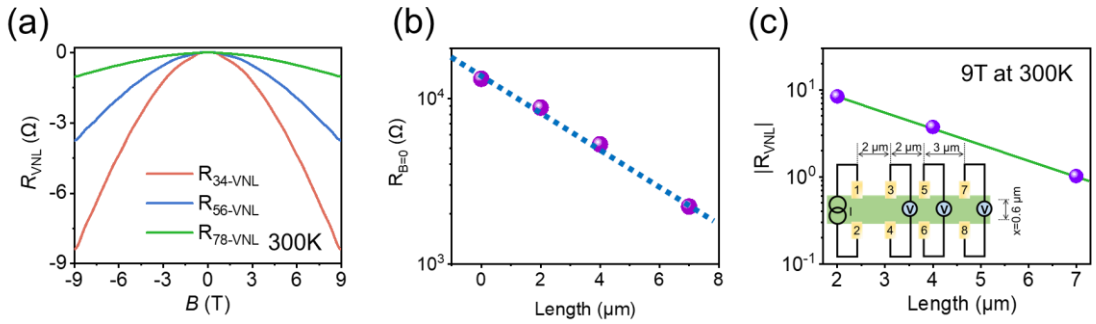

Figure 4.10 Length-dependent valley transport. (a) Nonlocal resistance as a function of the magnetic field. (b) The zero-magnetic field resistance as a function of length. (c) $|R_{VNL}|$ as a function of channel length in the semi-log curve, well fitted by a straight line. Inset is the schematic of the length-dependent valley device.

In addition, we also investigate the width-dependent valley transport behaviours. **Figure 4.11a** presents R_{NL} as a function of ***B*,** in which valley current is dependent on the different width (*e.g.*, -2.1 Ω for $R_{34\text{-VNL}}$ with 2 μm-width and -1.1 Ω for $R_{56\text{-VNL}}$ with 1 μm-width under 3T). The ratio of $R_{34\text{-VNL}}$ to $R_{56\text{-VNL}}$ is ~2 (**Figure 4.11b**), well consistent with the width ratio (inset of **Figure 4.11b**). The magnetic field-, length- and width-dependent results unambiguously support the existence of the valley transport in our Te samples.

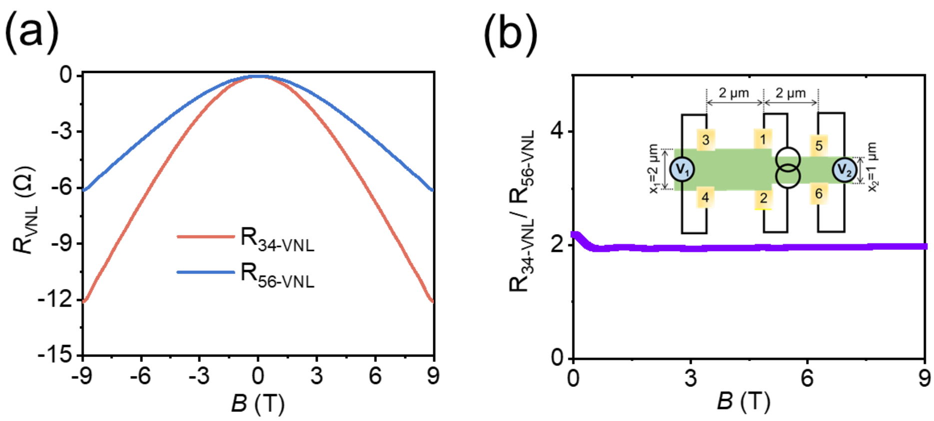

Figure 4.11 Width-dependent valley transport. (a) Width-dependent valley transport as a function of *B*. (b) Valley transport ratio of different widths. Inset is the schematic of the width-dependent valley device.

Chiral anomaly behaviour is further verified by the angle-dependent negative longitudinal magnetoresistance (MR), as shown in **Figure 4.12**. We performed angle-dependent MR measurements in our devices (**Figure 4.12a**). When the magnetic and electrical fields are perpendicular (θ=90°), there is the strongest positive MR. In comparison, when the magnetic field is parallel to the electrical field (θ=0°), there is obviously negative MR. The precise angle rotation measurement (**Figure 4.12b**) shows that the negative MR is weakened substantially as the small angle changes away from θ=0°. The temperature-dependent MR curves show that negative MR can appear at 100

K (**Figure 4.12c**) and it becomes stronger at low temperature, similar to the reported temperature-dependent negative MR in reported Dirac semimetal work[10]. These results support the observation of the chiral anomaly behaviours in our Te sample.

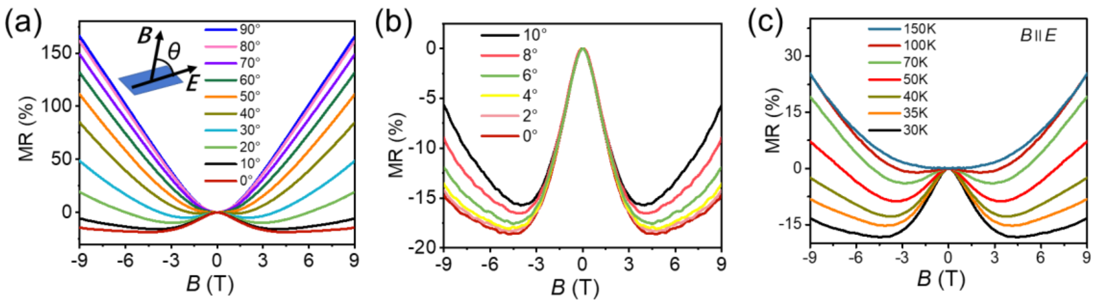

Figure 4.12 Angle- and temperature-dependent longitudinal MR. (a) Angle-dependent MR from 0° to 90° at 2K. Inset shows the definition of the rotation angle. The angle between *B* and *E* is defined as *θ*. (b) Precise angle-dependent negative MR from 0° to 10° at 2K. (c) Temperature-dependent MR from 150 K to 2 K. Negative MR appears at 100 K under a low magnetic field.

To achieve a high ON/OFF ratio, we used ionic liquid DEME-TFSI for electrostatic modulation to manipulate the CAVC. We adopt a dimensionless coefficient α_{VNL} to quantitatively describe the relative strength of valley current: $\alpha_{VNL}=|R_{VNL}/R_L|$. The curve of α_{VNL} as a function of B^2 exhibits linear shape and is tuneable by the gating voltages in the Te valley FET (**Figure 4.13a**). The α_{NL} -V_g curve of the Te valley FET exhibits the ON/OFF ratio of 10^5 at room temperature (**Figure 4.13b**), higher than the state-of-the-art valley FET reported in other works (10^2-10^3 ON/OFF ratio)[3]. This high ON/OFF ratio is from easy manipulation of E_F and Berry curvature in the Weyl semiconductor. We summarise the relationship between the ON/OFF ratio and thickness of Te flakes (**Figure 4.13c**). As the thickness increases from 28 nm to 50 nm, the ON/OFF ratio of Te valley devices decreases from 1.4×10^5 to 2.6×10^3, accompanied by the transition between enhancement-mode and depletion-mode FETs.

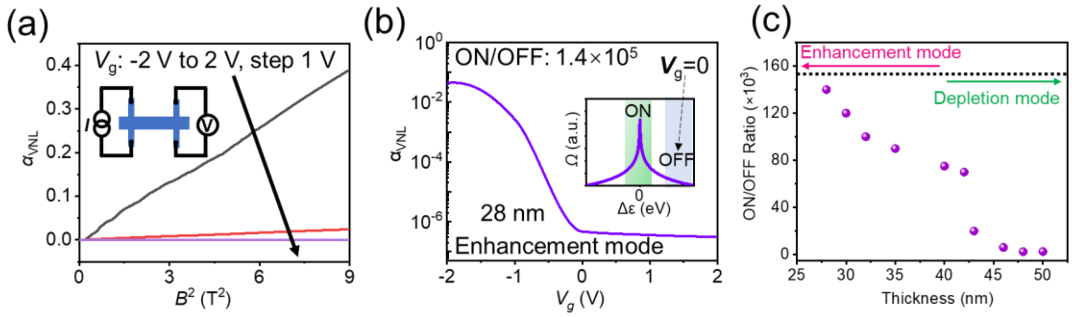

Figure 4.13 The performance of Te valley transistors. (a) α_{NL} as a function of B^2 in the Te valley transistor. (b) Transfer curve as a function of V_g in the 28-nm Te valley transistor under 1T. A typical enhancement-mode transistor. (c) ON/OFF ratio versus thickness of Te flakes in our valley transistors.

For comparison, we used the same Te flake (28-nm-thick) to characterise charge-based FET along the longitudinal direction (the inset of **Figure 4.14a**). The $\boldsymbol{I_d}$-$\boldsymbol{V_d}$ curve of the Te charge FET exhibits a linear shape under V_{ds} of 0 to 2V (**Figure 4.14a**). As the gate voltage (V_g) increases from -60 V to 60 V, the Te charge-based FET switches from the ON-state to the OFF-state with the ON/OFF ratio of 139 (**Figure 4.14b**). This ON/OFF ratio is comparable to reported Te FET works with similar thickness[16] (*e.g.*, ~200 ON/OFF ratio for 25-nm-thick and ~20 ON/OFF ratio for 30-nm-thick samples), but much lower than the 10^5 ON/OFF ratio of valley FET with the same Te flake. The performance of our valley FET is comparable to reported charge-based Te FET and much higher than reported valley FETs (**Table 4.2**).

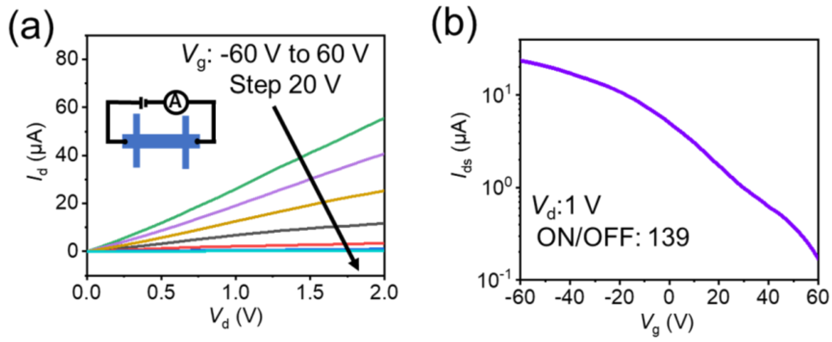

Figure 4.14 Charge-based FET in the same Te flake as the valley FET. (a) Output curve I_d-V_d in the charge-based FET as V_g increases from -60 V to 60 V with a step of 20V. (b) Transfer curve in the Te charge-based FET.

Table 4.2 Performance comparison among our valley transistor, Te charge transistor and valley transistor.

Works	Degree of freedom	ON/OFF
Nat. Electron 1, 228–236, 2018	Charge	~20 (30 nm thickness) ~200 (25 nm thickness) 10^6 (5 nm thickness)
Nat. Nanotechnol. 15, 53–58, 2020	Charge	10^4
Nat. Nanotechnol 15, 743-749, 2020	Valley	10^2~10^3
Our work	**Valley**	**10^5 (28 nm thickness)**

Moreover, we have performed thickness-dependent logic functions (AND, OR) based on valley transistors using low gating voltages and affordable magnetic fields as inputs (**Figure 4.15**). For the input1 (V_g), logic "0" and "1" are defined as 0 and 1 V, respectively. For the input2 (***B***), logic "0" and "1" are defined as 0.1 T and 0.2 T, respectively. The output "0" corresponds to $\alpha_{NL} \leq 10^{-4}$, and "1" corresponds to MR $\geq 10^{-4}$. In a 25-nm sample, we have to use a relatively high magnetic field and positive gating voltages to observe valley signal. Thus, when input1 and input2 are logic "1", the output is "1", corresponding to the AND logic function. In contrast, due to relatively high hole densities and downshift of $\boldsymbol{E}_F$ in 50-nm sample, when either input1 or input2 is logic "1", the output is "1", which is the OR logic function.

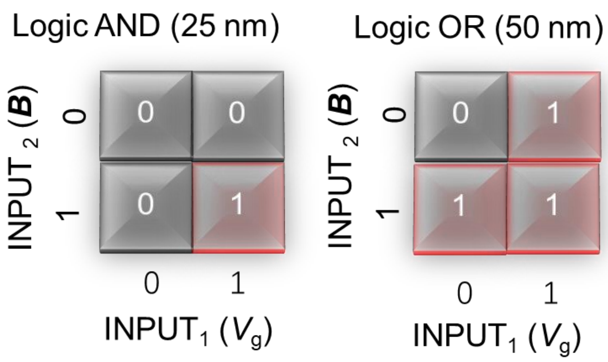

	"0"	"1"
IN 1 (V_g)	0	1V
IN 2 (B)	0.1T	0.2T
Output	$\alpha_{NL} \leq 10^{-4}$	$\alpha_{NL} > 10^{-4}$

Figure 4.15 Thickness-dependent logic functions (AND, OR).

After investigating the basic characterises and field-effect manipulation of CAVC, we are exploring the computing functions based on CAVC. Two crucial computing applications are processing static information and dynamic time-series data, which need different responding curves. For example, the artificial neural network (ANN) is a widely used neuromorphic computing network to deal with static information. ANN requires stable, discrete, and linear long-term potentiation (LTP) and long-term depression (LTD) synaptic behaviours[15]. To process time-series and dynamic signals such as language and voice[21,22], reservoir computing (RC) with the high nonlinearity and short-term memory responding curve is efficient. Because the Berry curvature is highly dependent on the position of $\boldsymbol{E}_{\mathrm{F}}$ ($\mathbf{1}/\boldsymbol{E}_{\mathrm{F}}^{2}$) in CAVC, it is reasonable to achieve the tunable nonlinearity and retention time to deal with static/dynamic information in one device.

We adopt solid-state PEO/$LiClO_4$ as the electrolyte of the valley FET, in which Li^+ can intercalate into Te flakes by the relaxation of PEO chains at room temperature above the glass transition temperature (-60 °C)[23]. To reveal the working mechanism of Li^+ intercalation and extraction, we carry out X-ray photoelectron spectroscopy (XPS) characterisation of the Te samples at different stages. XPS spectra (**Figure 4.16a**) show the shift of Te peaks in different samples. The characteristic XPS peaks for Te^0 and Li_2Te are ~573.1 eV and 572.4 eV, respectively[24]. The peak ~572.7 eV between ~571.1 eV and 572.4 eV in the Te sample after V_g=+2V pulses gating indicates the Li^+ intercalation into Te. The presence of Li peak (**Figure 4.16b**) in Te with V_g= +2V further supports Li^+ doping. Followed by V_g=-2V, the Li peak disappears, indicating the extraction of Li^+. Meanwhile, the XPS spectra (**Figure 4.16c**) show little peak of Cl in different samples, suggesting the complete removal of PEO/$LiCl_4$ after washing the samples. Thus, we can exclude the effects of adsorbed Li ions on the samples. These results suggest that Li^+ can successfully intercalate into Te after V_g= +2V and extract out after further V_g= -2V. As illustrated in **Figure 4.16b**, we can shift $\boldsymbol{E}_{\mathrm{F}}$ and the strength of Berry curvature step-by-step with a different doping concentration of Li^+.

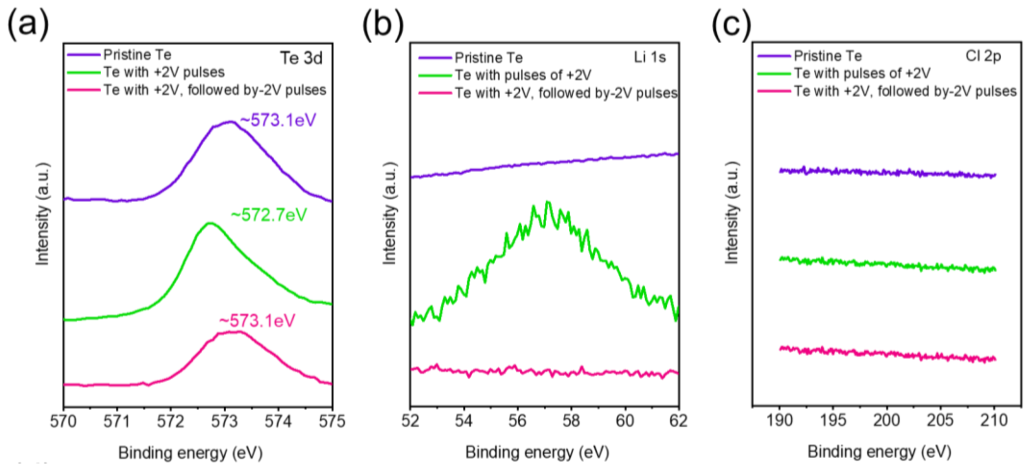

Figure 4.16 Ion intercalation/extraction mechanism in our valley devices. (a) XPS Te 3d spectra of Te. (b) XPS Li 1s spectra of Te. (c) XPS Cl 2p spectra of Te.

By regulating the gating voltage and time, we show cycle-to-cycle LTP and LTD valley synaptic states (**Figure 4.17a**). Positive pulses (130 ms of +2 V followed by 200 ms of 0 V in one writing process) results in 20 distinct states with a downward trend. Correspondingly, there are 20 states with an upward trend under pulses of -2V. The zoom-in image exhibits linear and distinct states, which is comparable to the state-of-the-art performance of charge-based synapses[15]. Under the retention test with 3000 s, the valley synaptic states are discrete and very stable, exhibiting the potential as synapses for the artificial neural network (**Figure 4.17b**).

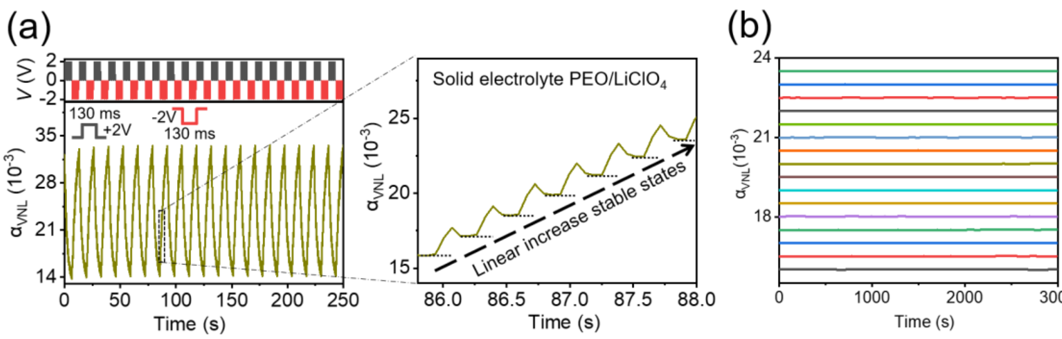

Figure 4.17 Stable valley states with linear increasing. (a) Long-term potentiation

and depression displaying discrete states under the control of voltage pulses. +2V is used to intercalate Li^+ into Te and move the E_F away from the Weyl point. -2V is used to extract Li^+ and move E_F back. The zoom-in of (a) with linear and discrete states. (b) Stable valley states under 3000 s retention tests.

We achieve different states (8, 16, 24, and 32) in the synaptic valley FETs (**Figure 4.18**) by applying different voltage pulses. All of them show discrete and linear states. To quantitatively analyse the nonlinearity, we fitted the experiment data (**Figure 4.19**). There is ultra-low nonlinearity (0.012/-0.442) in 8 states. The nonlinearities of LTP and LTD in other states are also very low: 16 states (0.895/-0.263), 24 states (1.295/-0.731), and 32 states (0.541/-0.664). 100 cycle-to-cycle operation tests show the stability of valley states with low variation(*e.g.*, 0.371% variation for 32 states).

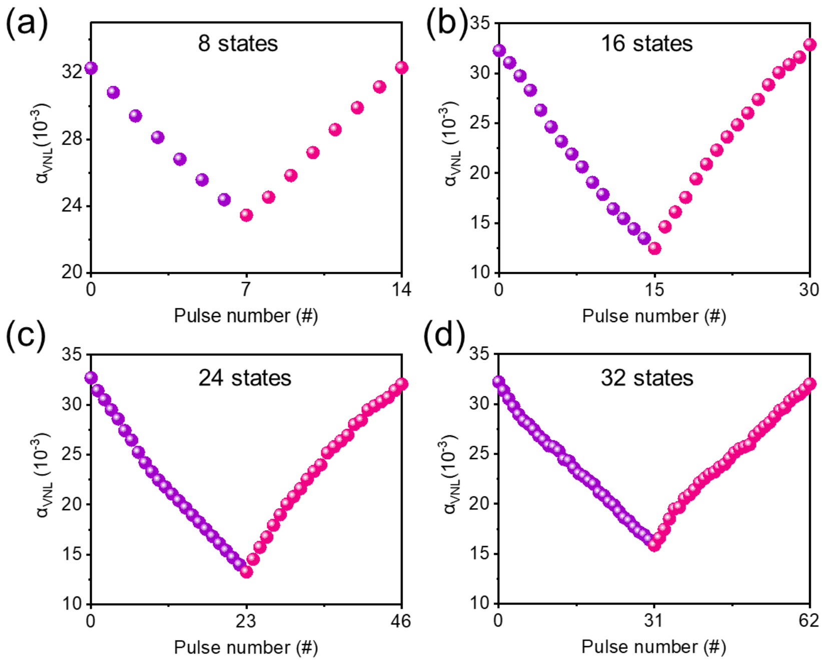

Figure 4.18 Valley synapses with different stable states. (a)8, (b)16, (c)24 and (d)32 discrete and linear states through electrochemical modulation.

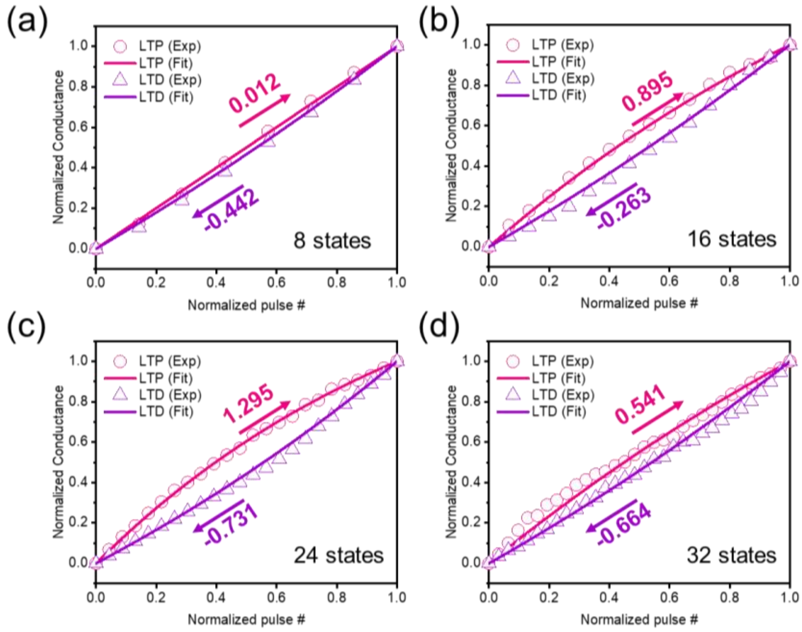

Figure 4.19 Different nonlinearities of the LTP and LTD to fit the experimental data. All the data are normalized from 0 to 1 before the fitting.

We conduct proof-of-concept valley-based ANN computing with the tested cycle-to-cycle synaptic behaviours (**Figure 4.20**), which clearly shows that the synaptic states are very stable with low variation (*e.g.* 0.371% for 32 states).

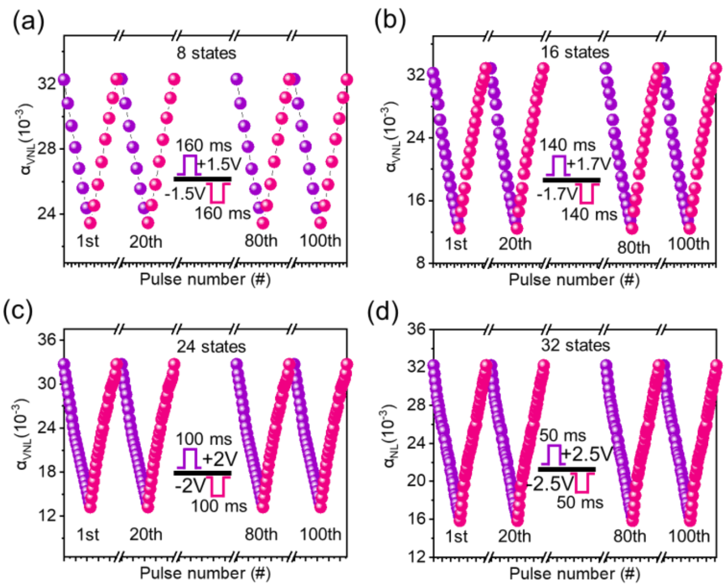

Figure 4.20 Cycle-to-cycle performance of valley synapses with different stable

states. (a)8, (b)16, (c)24 and (d)32 discrete states under different stimulation pulses.

We adopt a three-layer ANN for neuromorphic computing to classify the widely used handwritten database MNIST (**Figure 4.21a**). As the states increase from 8 to 32, the classifying accuracy rises gradually. After 50 epochs (**Figure 4.21b**), the accuracy is up to 95.2%, classifying accuracy based on 32 states. With the consideration of variation (0.371%), the classification is still higher than 95%. Thus, our classification accuracy is close to the numeric value of 96.5% after 40 training epochs. This performance is comparable to the state-of-the-art accuracy of neuromorphic computing based on charge devices[14,15]. Besides, in the valley synapses with 8 states, there is more than 91% accuracy due to ultra-low nonlinearity (0.012/-0.442).

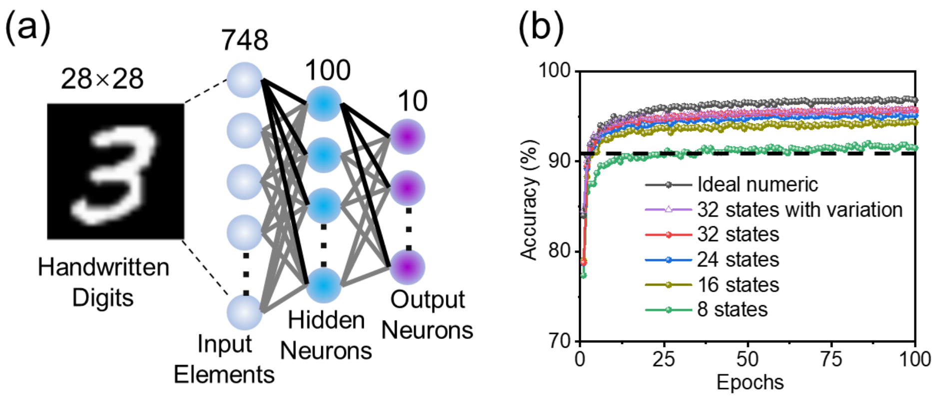

Figure 4.21 Processing the static information based on valley synapses with linear, discrete and stable states. (a) Neuromorphic computing based on a three-layer neural network. A voltage programmed crossbar array with valley synaptic devices is shown. (b) Training the neural network using different valley states based on voltage-controlled "write" operations for classifying static MNIST.

The distribution of synaptic values between the neurons of inputs and hidden layers after training were summarized in **Figure 4.22**.

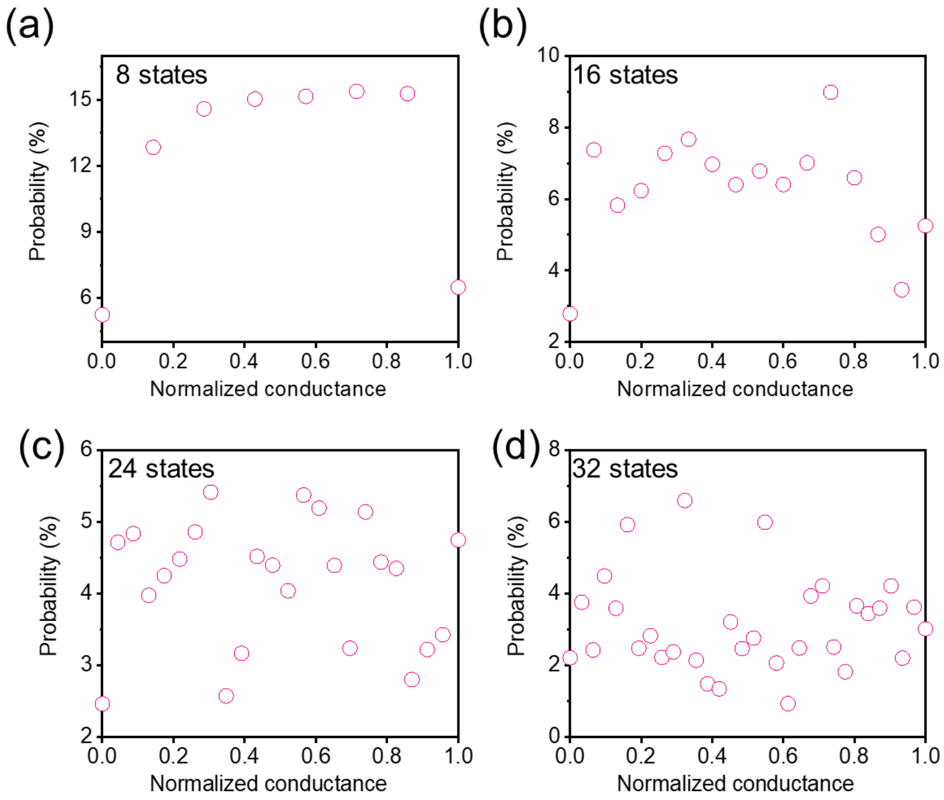

Figure 4.22 The distribution probability between the neurons of inputs and hidden layers in synapses with different states after training.

Besides dealing with static information, we are exploring the application of processing dynamic signals based on RC. High nonlinearity and short-term memory are two critical parameters to change the time-series data into high-dimensional states for RC. We have achieved a nonlinear decaying curve with short-term memory (~10 ms), which is suitable for RC (**Figure 4.23a**). Characteristic constant t_0 obtained by fitting is 2.55 ms. **Figure 4.23b** shows the representative modulation of our dynamic valley FET with the reception of 4 input signals: (10010), (11011), (01110), and (10101). The response of the device originates from ion adsorption and relaxation, which dynamically affects the E_F. Signal "1" represents the applied stimulation pulse with an amplitude of 4 V and time of 1 ms. Moreover, we acquire all the possible stimulation from (0000) to (11111), with 32 distinct output values in total (**Figure 4.23c**).

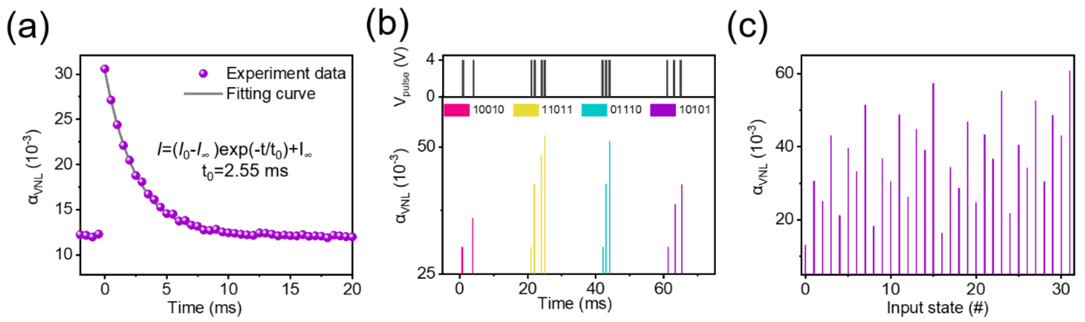

Figure 4.23 Nonlinear and short-term memory behaviours with the pulse coding. (a) Nonlinear decaying curve with short-term memory. Decaying data follows a fitted exponential curve and the characteristic time t_0 obtained by fitting is 2.55 ms. After stimulation, it takes about ~10 ms for the output value to retain stability. (b) Dynamic responses after representative input signals, (10010), (11011), (01110) and (10101). "1" indicates the applied stimulation pulse of 4 V with 1 ms. (c) The summarised output of the device at the fifth pules.

All the input states in **Figure 4.23c** are numbered (#) based on the binary encoding, as shown in the first column of **Table 4.3**. The second column to the sixth column is the applied voltages of Pulse-1, Pulse-2, Pulse-3, Pulse-4 and Pulse-5.

Table 4.3 The outputs after 32 different input states numbered #0 to #31.

Input state	Pulse-1	Pulse-2	Pulse-3	Pulse-4	Pulse-5	Output α_{VNL} (10^{-3})
#0	0	0	0	0	0	13.05

#1	0	0	0	0	1	30.64
#2	0	0	0	1	0	25.08
#3	0	0	0	1	1	42.98
#4	0	0	1	0	0	21.23
#5	0	0	1	0	1	39.55
#6	0	0	1	1	0	33.22
#7	0	0	1	1	1	51.44
#8	0	1	0	0	0	18.26
#9	0	1	0	0	1	36.74
#10	0	1	0	1	0	30.47
#11	0	1	0	1	1	48.82
#12	0	1	1	0	0	26.25
#13	0	1	1	0	1	44.77
#14	0	1	1	1	0	39.12
#15	0	1	1	1	1	57.44
#16	1	0	0	0	0	16.33
#17	1	0	0	0	1	34.29
#18	1	0	0	1	0	28.62
#19	1	0	0	1	1	46.82
#20	1	0	1	0	0	24.71

#21	1	0	1	0	1	43.36
#22	1	0	1	1	0	36.71
#23	1	0	1	1	1	55.17
#24	1	1	0	0	0	21.75
#25	1	1	0	0	1	40.47
#26	1	1	0	1	0	34.2
#27	1	1	0	1	1	52.69
#28	1	1	1	0	0	30.47
#29	1	1	1	0	1	48.64
#30	1	1	1	1	0	42.92
#31	1	1	1	1	1	60.76

We use pulse-coding to process dynamic icons of the Tokyo Olympic Games in 2021(**Figure 4.24a**). Each dynamic icon shows motions with much difference. In one motion, every five pixels is a group and processed nonlinearly based on one valley FET. For example, pixels in the row of the "golf" icon is coded as (1100111111100001000111111), which is further divided into (11001), (11111), (10000), (10001), and (11111). **Figure 4.24b** displays the schematic of our neuromorphic computing network with the reservoir. In this computing system, the connecting weights among the reservoir nodes are randomly assigned, while connecting weights between the reservoir nodes and the output nodes are trained.

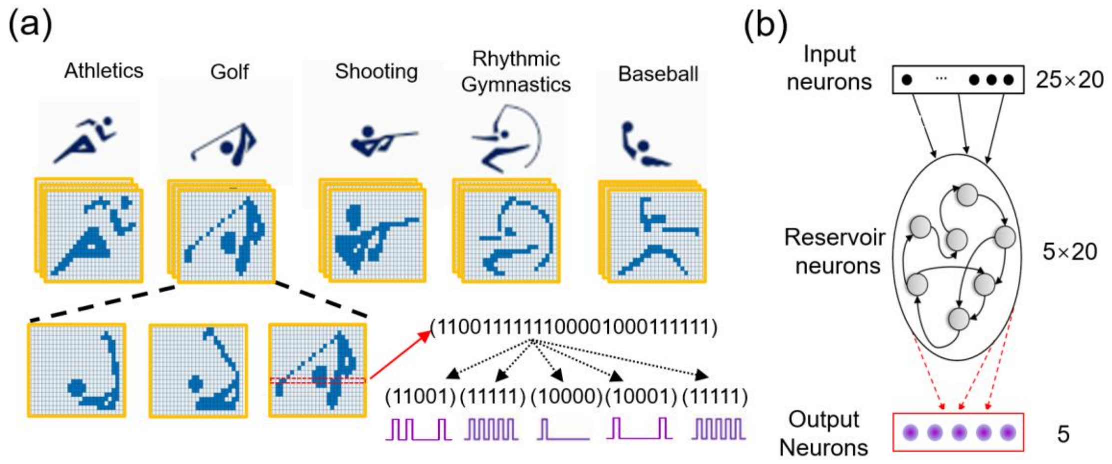

Figure 4.24 Nonlinear and short-term memory behaviours with the pulse coding. (a) Pulse-coding to nonlinearly deal with five dynamic icons of the Tokyo Olympic Games. Each dynamic icon consists of three much different motions. Every five pixels is a group for nonlinear processing. (b) Reservoir computing network to process dynamic information. The classifying accuracy of processing dynamic information.

The states of reservoir neurons for the rhythmic gymnastics icon are experimentally measured (**Figure 4.25a**), which is used for the training and inference in reservoir computing. The classifying accuracy of dynamic icons with 10% noise reaches 95% after 65 epochs (**Figure 4.25a**), indicating that our valley FETs can easily classify the dynamic data after training even if there is much different time-series information. The confusion matrix (**Figure 4.25c**) exhibits the five dynamic icons' classification, showing that the RC based on valley FETs can correctly classify nearly all of the dynamic icons. The measured states of the reservoir neurons for other dynamic icons are shown in **Figure 4.26**.

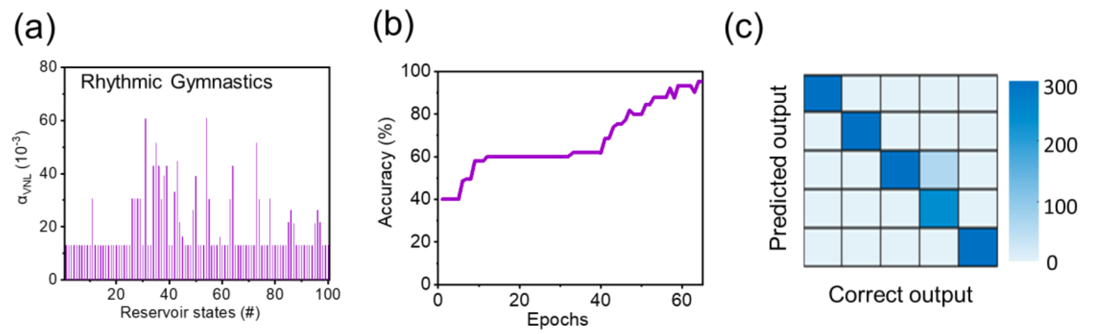

Figure 4.25 Classifying the dynamic icons. (a) The measured states of the reservoir neurons for the rhythmic gymnastics icon. (b) Accuracy of classifying the dynamic ions with 10% noise based on the reservoir computing network. (c) Confusion matrix for classifying the five dynamic icons of the test set. Colour bar: occurrence of a given predicted output.

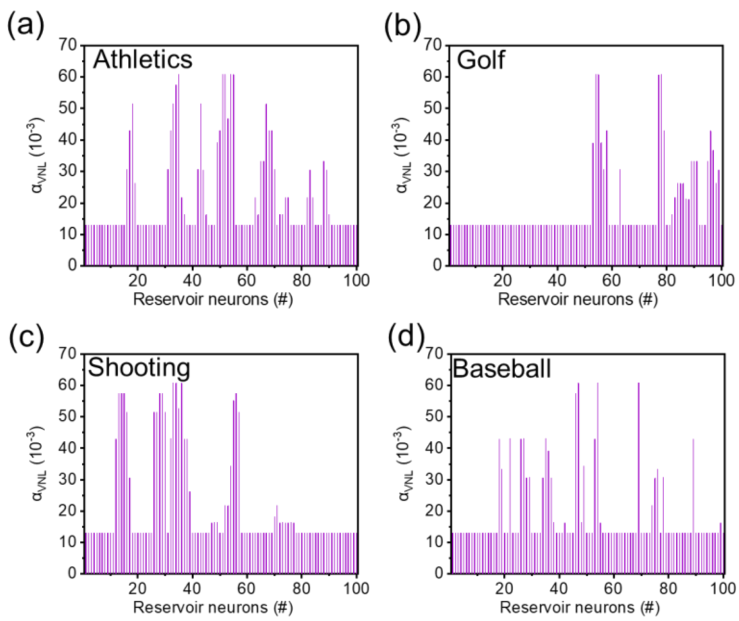

Figure 4.26 The measured states of the reservoir neurons for different dynamic icons.

In the training process, we add 10% noise into the dynamic figures (**Figure 4.27**). The details of adding noise to different dynamic icons are shown in **Figure 4.28** (athletics), **Figure 4.29** (golf), **Figure 4.30** (shooting) and **Figure 4.31** (rhythmic gymnastics) and **Figure 4.32** (baseball).

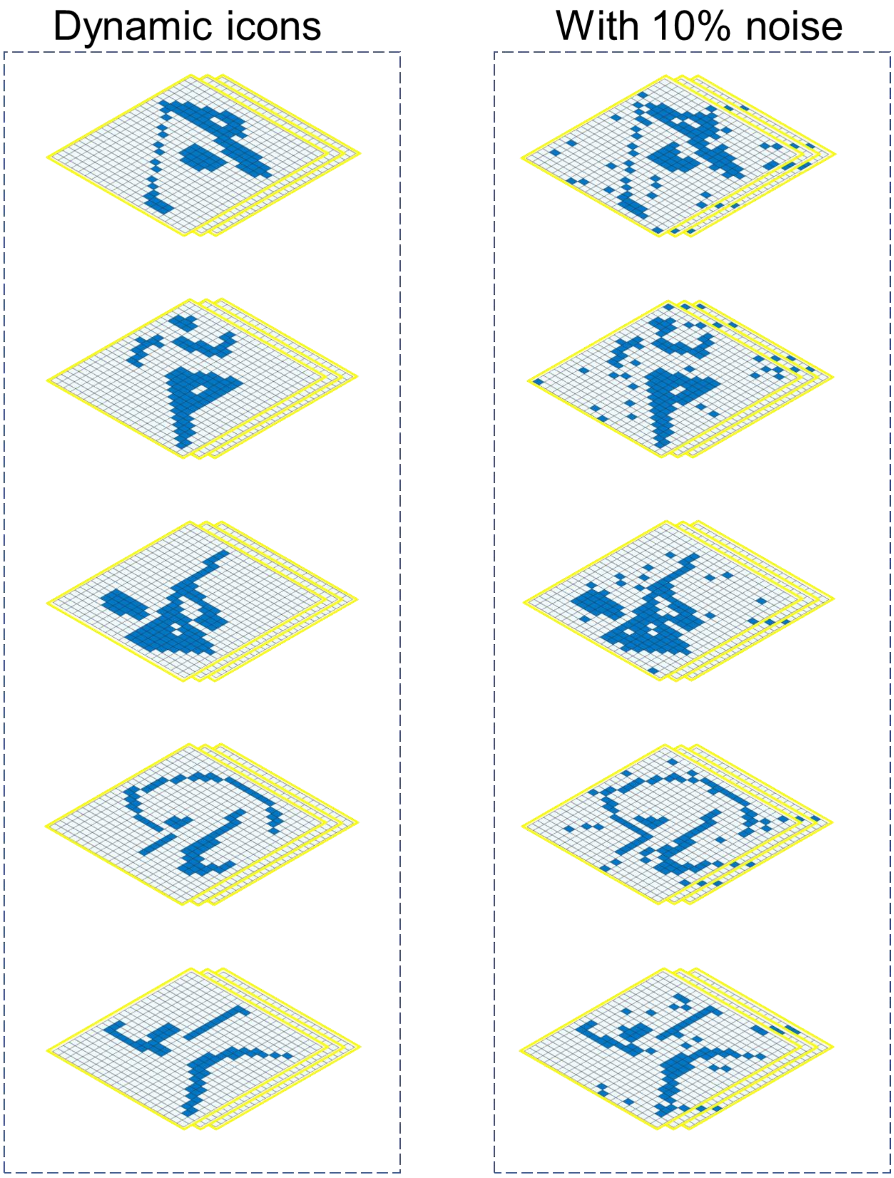

Figure 4.27 Dynamic icons with 10% noise for the test in reservoir computing.

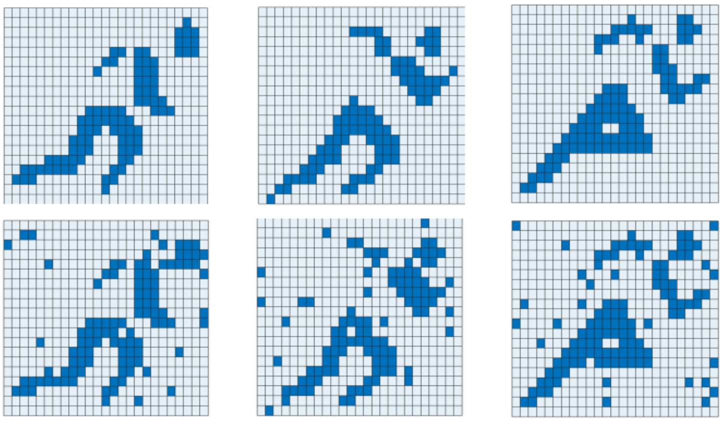

Figure 4.28 Dynamic athletics icon with 10% noise for the test in reservoir computing.

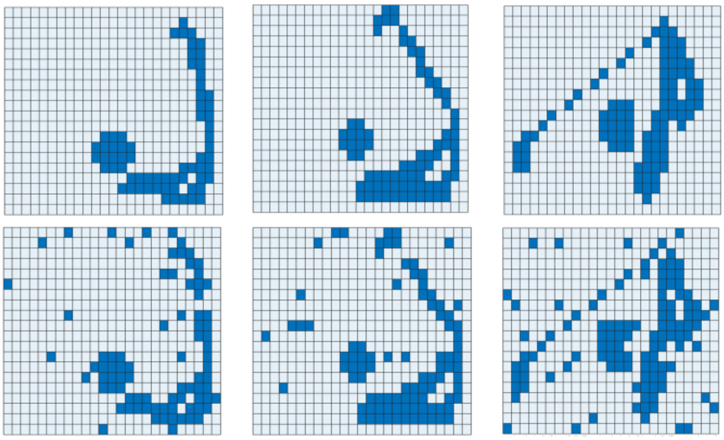

Figure 4.29 Dynamic golf icon with 10% noise for the test in reservoir computing.

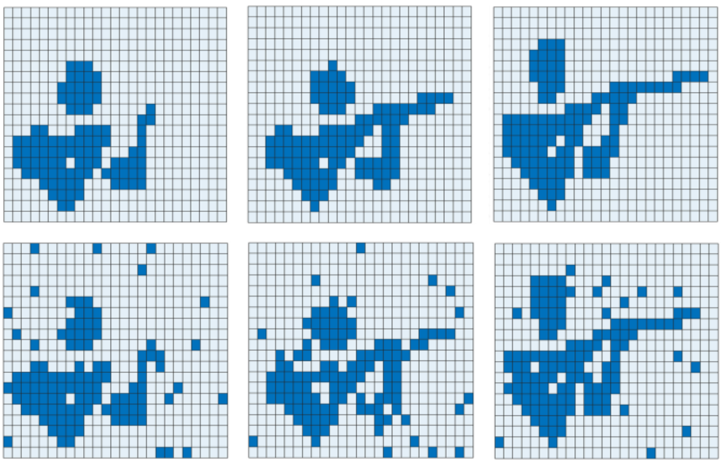

Figure 4.30 Dynamic shooting icon with 10% noise for the test in reservoir computing.

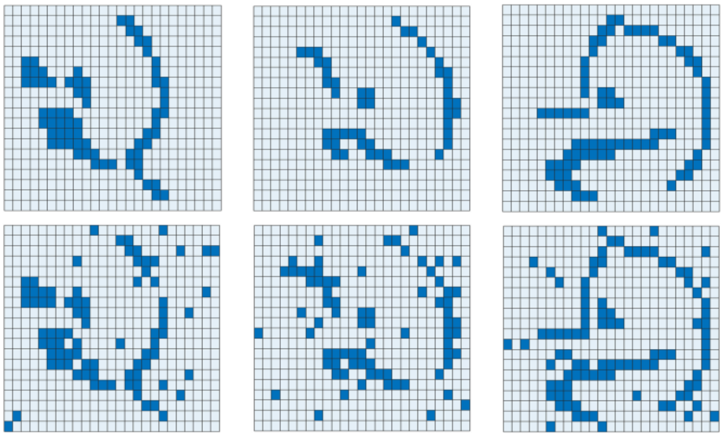

Figure 4.31 Dynamic rhythmic gymnastics icon with 10% noise for the test in the reservoir computing.

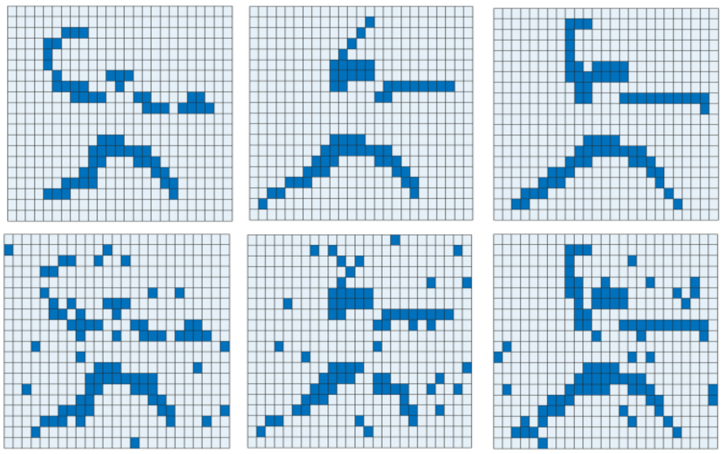

Figure 4.32 Dynamic baseball icon with 10% noise for the test in reservoir computing.

Since there is a coexistence of the electrical double layer and ion intercalation mechanism in our valley devices, we can use ion gating to achieve the required responding curves based on CAVC. This tunability of CAVC provides a platform to attain neuromorphic computing to process static and dynamic information with high accuracy in one valley FET. In contrast, reported neuromorphic devices always only exhibit linear or nonlinear curves in one device to deal with static or dynamic signals.

4.4 Summary

We investigate the magneto-transport of Weyl semiconductor Te and verify the presence of CAVC with 7 μm diffusion length at room temperature. We design and demonstrate the valley FET with the 10^5 ON/OFF ratio under low gating voltage ($\leq$2 V) at room temperature. We have manipulated valley synapses with different nonlinearity and retention time (3000 s to 10 ms), suitable for neuromorphic processing static/dynamic information. ANN can show more than 95% accuracy for classifying static MNIST data. We have achieved similar accuracy in processing dynamic icons from Tokyo Olympic Games based on RC. With the low-dissipation characteristics of valley degree, our valley FET can process both static and dynamic information in one device provides alternatives to conventional charge-based devices.

4.5 References

1 Mak, K. F., Xiao, D. & Shan, J. Light–valley interactions in 2D semiconductors. *Nature Photonics* **12**, 451-460 (2018).

2 Jones, A. M. *et al.* Optical generation of excitonic valley coherence in monolayer WSe_2. *Nature Nanotechnology* **8**, 634-638 (2013).

3 Li, L. *et al.* Room-temperature valleytronic transistor. *Nature Nanotechnology* **15**, 743-749 (2020).

4 Ye, Y. *et al.* Electrical generation and control of the valley carriers in a monolayer transition metal dichalcogenide. *Nature nanotechnology* **11**, 598-602 (2016).

5 Li, H.-K. *et al.* Valley optomechanics in a monolayer semiconductor. *Nature Photonics* **13**, 397-401 (2019).

6 Sui, M. *et al.* Gate-tunable topological valley transport in bilayer graphene. *Nature Physics* **11**, 1027-1031 (2015).

7 Schaibley, J. R. *et al.* Valleytronics in 2D materials. *Nature Reviews Materials* **1**, 1-15 (2016).

8 Parameswaran, S., Grover, T., Abanin, D., Pesin, D. & Vishwanath, A. Probing the chiral anomaly with nonlocal transport in three-dimensional topological semimetals. *Physical Review X* **4**, 031035 (2014).

9 Kharzeev, D. E. The chiral magnetic effect and anomaly-induced transport. *Progress in Particle and Nuclear Physics* **75**, 133-151 (2014).

10 Zhang, C. *et al.* Room-temperature chiral charge pumping in Dirac semimetals. *Nature Communications* **8**, 13741 (2017).

11 Qiu, G. *et al.* Quantum Hall effect of Weyl fermions in n-type semiconducting tellurene. *Nature Nanotechnology* **15**, 585-591 (2020).

12 Zhang, N. *et al.* Magnetotransport signatures of Weyl physics and discrete scale invariance in the elemental semiconductor tellurium. *Proceedings of the National Academy of Sciences* **117**, 11337-11343 (2020).

13 Liu, L. *et al.* Aligned, high-density semiconducting carbon nanotube arrays for high-performance electronics. *Science* **368**, 850-856 (2020).

14 van de Burgt, Y. *et al.* A non-volatile organic electrochemical device as a low-voltage artificial synapse for neuromorphic computing. *Nature materials* **16**, 414-418 (2017).

15 Fuller, E. J. *et al.* Parallel programming of an ionic floating-gate memory array for scalable neuromorphic computing. *Science* **364**, 570-574 (2019).

16 Wang, Y. *et al.* Field-effect transistors made from solution-grown two-dimensional tellurene. *Nature Electronics* **1**, 228-236 (2018).

17 Kresse, G. & Furthmüller, J. Efficiency of ab-initio total energy calculations for metals and semiconductors using a plane-wave basis set. *Computational materials science* **6**, 15-50 (1996).

18 Perdew, J. P., Burke, K. & Ernzerhof, M. Generalized gradient approximation made simple. *Physical review letters* **77**, 3865 (1996).

19 Blöchl, P. E. Projector augmented-wave method. *Physical review B* **50**, 17953 (1994).

20 Ma, Q. *et al.* Direct optical detection of Weyl fermion chirality in a topological semimetal. *Nature Physics* **13**, 842-847 (2017).

21 Sun, L. *et al.* In-sensor reservoir computing for language learning via two-dimensional memristors. *Science advances* **7**, eabg1455 (2021).

22 Zhong, Y. *et al.* Dynamic memristor-based reservoir computing for high-efficiency temporal signal processing. *Nature Communications* **12**, 1-9 (2021).

23 Yang, C. S. *et al.* All-Solid-State Synaptic Transistor with Ultralow Conductance for Neuromorphic Computing. *Advanced Functional Materials* **28**, 1804170 (2018).

24 Zhang, J., Yin, Y. X., You, Y., Yan, Y. & Guo, Y. G. A High-Capacity Tellurium@ Carbon Anode Material for Lithium-Ion Batteries. *Energy Technology* **2**, 757-762 (2014).

Chapter 5 Conclusions and outlook

5.1 Conclusions

This thesis investigates the application of chiral anomaly for electronics. We designed and demonstrated three kinds of chiral anomaly-based devices: chirality-based field-effect devices with Dirac semimetal $PtSe_2$, topological transistors with Weyl semiconductor Te and room-temperature valley transistors for static and dynamic information processing.

Firstly, we design and demonstrate a device structure for controlling chirality transport in Dirac semimetal $PtSe_2$. The chirality-based field-effect devices show efficient electrostatic control over chiral anomaly current with an ON/OFF ratio of more than 10^3 and realize basic logic functions. The nonlocal valley transport is width- and length-dependent, which can also be effectively modulated by magnetic and electrical fields. This study provides a way to control the transport of chirality degree of freedom, which has the potential for significantly reducing power consumption compared with state-of-the-art charge-based FETs.

Secondly, we design and demonstrate the TPCTs that can retain a highly conductive and low-dissipation ON state and switch to a trivial phase OFF state with high resistance. We efficiently manipulated topological FETs based on Weyl semiconductor Te with negative MR up to -90%. We have achieved both enhancementsand depletion-mode topological FETs with ~10^8 ON/OFF ratio and ultrahigh ON conductivity (3.9×10^4 μS/μm), superior to general charge-based FETs. Furthermore, we demonstrate multiple-input OR-AND logic function and angle-switching logic functions (AND, OR) in one device. Our proposed Te topological device has the potential of solving power consumption and footprint limits of traditional charge-based FETs.

Thirdly, we investigate the magneto-transport of Weyl semiconductor Te and verify the presence of CAVC with 7 μm diffusion length at room temperature. We design and demonstrate the valley FET with the 10^5 ON/OFF ratio with nearly no memory effect. We have manipulated responding curves with different nonlinearity and retention time (3000 s to 10 ms), suitable for neuromorphic processing static/dynamic information. Accuracies both reach 95% for classifying static MNIST data and dynamic icons of the Tokyo Olympic Games. With the low-dissipation characteristics of valley degree and tunable curves, our valley FET can process static and dynamic information in one device efficiently, providing alternatives to conventional charge-based devices.

In the chiral anomaly-based devices, the used Weyl materials include the widely investigated Dirac semimetals and the emerging Weyl semiconductors. Ion electrolyte is used to form an electrical double layer to efficiently manipulate the chiral anomaly volatilely or acting as the Li^+ source with the intercalate/extraction mechanism to non-volatilely affect the chiral anomaly. There is superior performance in the transfer curve with a 10^8 ON/OFF ratio. With dynamic ion adsorption and intercalation, room-temperature valley devices are used for processing static and dynamic information.

5.2 Outlook

After achieving three different chiral anomaly-based devices, there is still much room to explore electronic applications. The performance, functions and large-scale preparation can be further explored.

(1) N-type valley FETs. The prepared FETs in this thesis are based on the Weyl point in the valence band of Te, which shows a typical p-type transfer curve. N-type valley FETs can be prepared by decorating Al_2O_3 on thin films through atomic layer deposition because depositing Al_2O_3 is effective to upshift the $\boldsymbol{E}_F$ of Te to the Weyl point of the conduction band[1].

(2) Complementary logic devices (such as the inverter). Complementary logic devices are important in modern electronics. Both charge- and spin-based complementary logic devices have been achieved[2,3]. Here, we can achieve the valley-based inverter by combining the p-type and n-type valley FETs.

(3) Preparing the ion electrolyte through the technology compatible with the integrated circuit. For examples, depositing wafer-scale polymer electrolyte of a nano-scale thickness through the chemical vapour deposition[4] or preparing the Li_xSiO_2 electrolyte through the magnetic sputtering[5].

(5) Using the high-k dielectric layer instead of the ion electrolyte for manipulation. Some high-k dielectric layers such as HfO_2 can manipulate up to 3×10^{13} cm^{-2} carrier density[6], strongly affecting the $\boldsymbol{E}_F$ in the Weyl semiconductor Te.

(5) Achieving higher ON/OFF ratio and lower subthreshold swing. For example, it is more efficient to manipulate $\boldsymbol{E}_F$ by preparing the Te flakes with fewer trapping defects. Ferroelectric materials (such as $Hf_{0.5}Zr_{0.5}O_2$) as the gating layer have the potentials of reducing the subthreshold swing[7].

5.3 References

1 Qiu, G. *et al.* Quantum Hall effect of Weyl fermions in n-type semiconducting tellurene. *Nature Nanotechnology* **15**, 585-591 (2020).

2 Baek, S.-h. C. *et al.* Complementary logic operation based on electric-field controlled spin–orbit torques. *Nature Electronics* **1**, 398-403 (2018).

3 Huang, W., Markwart, J. C., Briseno, A. L. & Hayward, R. C. Orthogonal Ambipolar Semiconductor Nanostructures for Complementary Logic Gates. *ACS nano* **10**, 8610-8619 (2016).

4 Yu, J. M. *et al.* All-Solid-State Ion Synaptic Transistor for Wafer-Scale Integration with Electrolyte of a Nanoscale Thickness. *Advanced Functional Materials*, 2010971 (2021).

5 Li, Y. *et al.* Oxide-Based Electrolyte-Gated Transistors for Spatiotemporal Information Processing. *Advanced Materials* **32**, 2003018 (2020).

6 Gieraltowska, S. *et al.* Properties and characterization of ALD grown dielectric oxides for MIS structures. *ACTA PHYSICA POLONICA A* **119**, 692-695 (2011).

7 Zhang, Z. *et al.* FinFET with improved subthreshold swing and drain current using 3-nm ferroelectric Hf 0.5 Zr 0.5 O 2. *IEEE Electron Device Letters* **40**, 367-370 (2019).